Advanced Laboratory course

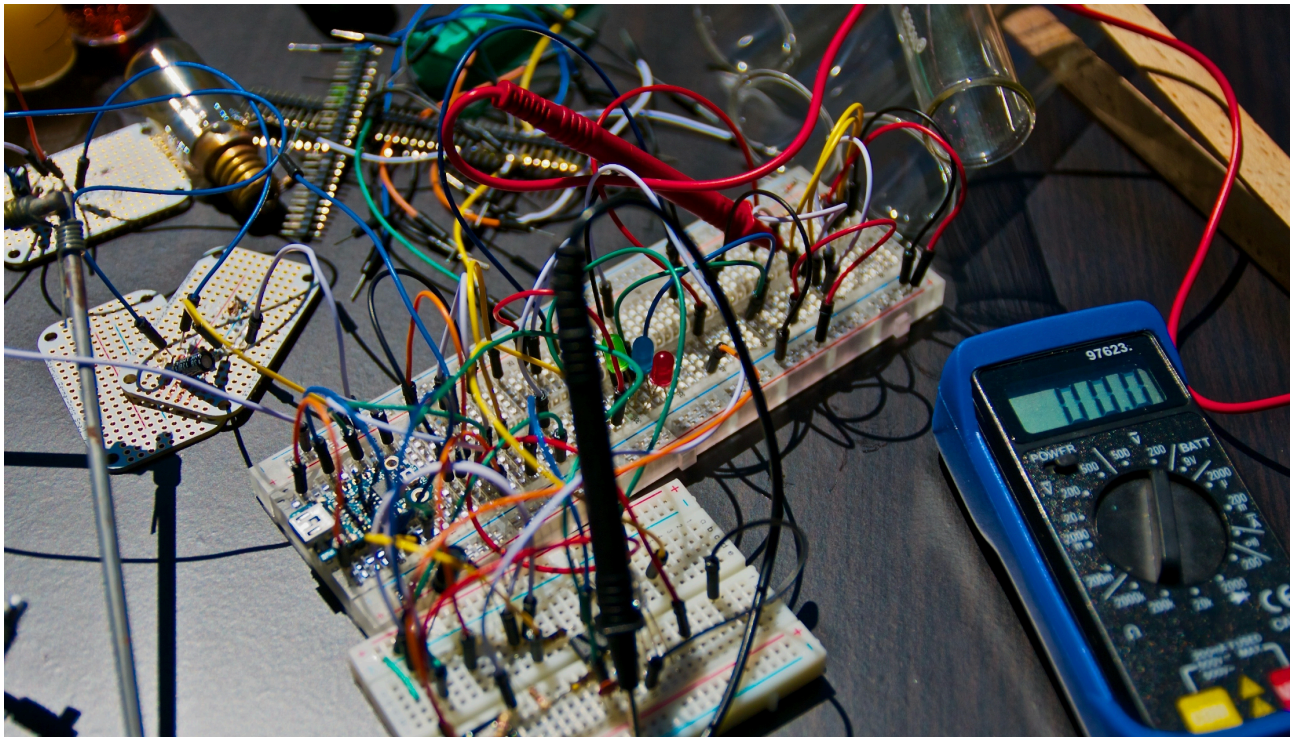

Fabio Cufino IMAPP

LT1

Interaction of particles with matter

Short reminder of technical terms and how they are used in literature
Example: proton beam on matter

- fluence (Fluenz): number of protons that cross an infinitesimal area

$$\Phi := \frac{dN}{dA} \quad [\Phi] = \frac{\text{protons}}{\text{cm}^2}$$

- fluence rate (Fluenzrate): time derivative of fluence (sometimes called flux); bei Krieger: Flussdichte

$$\dot{\Phi} = \frac{d\Phi}{dt} =: \phi \quad [\phi] = \frac{\text{protons}}{\text{cm}^2\ \text{s}}$$

- stopping power (Stoßbremsvermögen): rate of energy loss per distance in matter

$$S := -\frac{dE}{dx} \quad [S] = \frac{\text{MeV}}{\text{cm}}$$

- mass stopping power (Massenstoßbremsvermögen): stopping power normalized to density of the material

$$\frac{S}{\rho} := -\frac{1}{\rho}\frac{dE}{dx} \quad \left[\frac{S}{\rho}\right] = \frac{\text{MeV}}{\text{g/cm}^2}$$

Interaction in matter

1. Photoelectric Effect

Interaction Mechanism

- **Interaction with shell electrons**, typically from inner shells (K, L, M).
- **Photon absorption**: The photon is absorbed, causing an electron to be ejected, leaving the atom in an excited state.
- **Deexcitation**: The atom returns to its ground state by emitting a secondary photon.

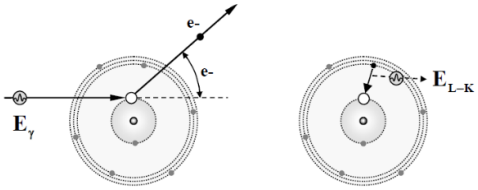

Cross Section and Photo Absorption Coefficient (τ)

The cross section, described by the photo absorption coefficient τ, depends on:

- **Medium density (ρ).**
- **Electron density per atom:** For K-shell electrons, the cross section is proportional to Z^5, where Z is the atomic number, with a weaker dependence for outer shells.
- **Photon energy:**
  - Maximum cross section occurs when $E_\gamma = E_{\text{bind}}$ for K-shell electrons.
  - The cross section decreases as $1/E^3$ up to 511 keV, with a weaker dependence at higher energies.

$$\tau \propto \rho \cdot Z^{4-5} \cdot \begin{cases} \frac{1}{E_\gamma^3} & \text{for } E_\gamma \ll 511\,\text{keV} \\ \frac{1}{E_\gamma} & \text{for } E_\gamma \gg 511\,\text{keV} \end{cases}$$

Special Nuclear Photoelectric Effect:

- **Photon absorption by the nucleus:** Leads to nuclear excitation, oscillation, and the emission of individual nucleons.

2. Compton Effect

Interaction Mechanism

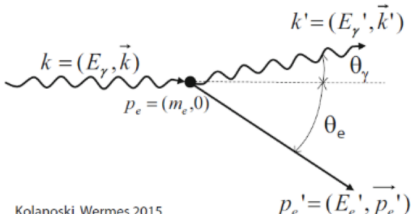

- **Photon energy significantly larger than binding energy:** The electron can be treated as quasi-free.
- **Elastic interaction:**

$$\gamma + e^- \rightarrow \gamma' + e'^-$$

- **Energy transfer:** The photon transfers part of its energy to the electron, which is emitted at an angle.
- **Photon wavelength increase:** The photon's wavelength increases, reducing its energy.
- **Scattering angle dependence:** The energy transferred to the electron depends on the scattering angle.

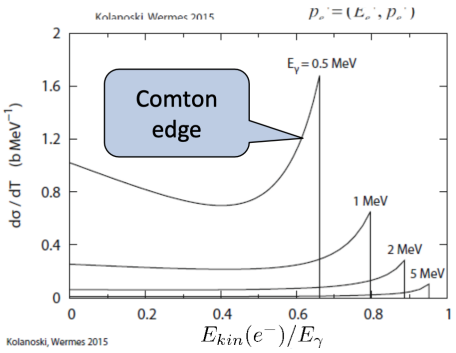

Compton Wavelength Shift

$$\Delta\lambda = \lambda' - \lambda = 2\lambda_C \sin^2\left(\frac{\theta_\gamma}{2}\right)$$

where the Compton wavelength is:

$$\lambda_C = \frac{h}{m_e c} \approx 0.0243 \text{ Å}$$

- **Maximum energy transfer:** Occurs at $\theta_\gamma = 180°$, leading to the Compton edge in the electron energy spectrum.
- **Klein-Nishina formula:** Describes the cross section per electron.

$$\sigma_C^{\text{Atom}} = Z \cdot \sigma_C$$

3. Pair and Triplet Creation

Interaction Mechanism

- **Photon absorption and pair production:** In the presence of a nucleus, a photon can create an electron-positron pair.

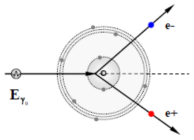

pair creation

- **Triplet production:** Similar, but results in the creation of three particles.

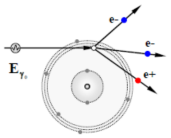

triplet creation

Cross Section:

$$\kappa_{\text{pair}} \propto Z \cdot \rho \cdot \log E$$

Summary

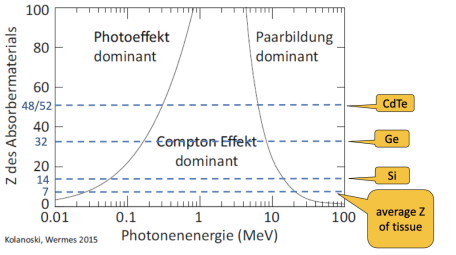

Attenuation of Photon Beams

In most cases photon is absorbed and transfers its full energy. These are stochastic processes.

- **Photon absorption in matter:** Photons are absorbed stochastically, transferring their full energy to the medium.

  $$I(x) = I_0 e^{-\mu x}$$

  where μ is the mass absorption coefficient.
  Lambert-Beer equation

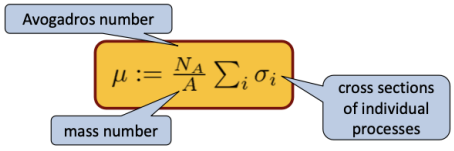

Neutrons

Neutrons don't carry electric charge, interaction in matter only via strong interaction: indirectly ionizing.

Nuclear interaction in matter:

- Elastic scatterig -> creates recoil proton or nucleus, which can ionize in turn -> main mechanism of radiation damage and dose deposition
- Inelastic scattering neutron excites a nucleus emission of MeV photons
- Neutron capture
  - emission of high energy photons/gammas
  - emission of individual nucleons -> charged, densly ionizing

• fission or spallation -> nuclear fragments also densly ionizing

Interaction of neutrons in matter via multitude of channels, but always indirectly!

Interaction of Charged Particles in Matter

Coulomb Interaction

- **Dominant interaction:** Charged particles primarily interact with shell electrons via Coulomb forces.
  - **Excitation and ionization:** Up to high energies, this is the dominant process.
  - **Radiative effects:** Become significant for $E > E_{\text{crit}}$.

Bethe-Bloch Formula

Describes energy loss through excitation and ionization:

$$-\left\langle \frac{dE}{dx} \right\rangle = K\frac{Z}{A}\rho\frac{z^2}{\beta^2}\left[\frac{1}{2}\ln\frac{2m_e c^2\beta^2\gamma^2 T_{\max}}{I^2} - \beta^2 - \frac{\delta(\beta\gamma)}{2} - \frac{C(\beta\gamma, I)}{Z}\right]$$

Components of the Formula

- $K = 4\pi N_A r_e^2 m_e c^2 \approx 0.307\,\mathrm{MeV cm^2/mol}$
- z, β: Charge and velocity of the projectile
- Z, A: Charge and mass of target nucleons (typically $Z/A \approx 0.5$ for most materials)
- I: Mean excitation energy of the target atoms
- $T_{\max}$: Maximum energy transfer per interaction
- δ: Density corrections at high energy
- C/Z: Shell corrections at low energy

Energy loss due to large number of individual stochastic scattering processes: **consider mean energy loss**

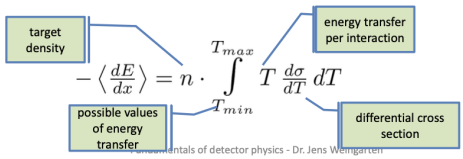

How to get to the formula?

Step 1: Energy loss due to Rutherford scattering with shell electrons

Assumption:
1. projectile much heavier than electron $M \gg m_e$
2. projectile fast wrt electron $E_{kin} \gg E_{bind}$
   → elektron „free“
3. charge of the projectile $q = z \cdot e$

Rutherford cross section:
$\frac{d\sigma}{dQ}|_{Ruth} = \frac{4\pi z^2\alpha^2\hbar^2c^2}{\beta^2}\frac{1}{Q^4}$
using momentum transfer $Q^2 = -(p_e - p_e')^2 = 2m_e c^2 T$
and velocity of projectile relative to shell electron βc

Account for spin of the electron→ Mott cross section
$\frac{d\sigma}{dQ}|_{Mott} = \frac{d\sigma}{dQ}|_{Ruth} \cdot \left(1 - \beta^2\frac{T}{T_{max}}\right)$

Calculate integral for $T_{min} \gg E_{bind}(e)$ and $T_{min} \ll T_{max}$

$-\left\langle \frac{dE}{dx} \right\rangle = \frac{2\pi z^2\alpha^2\hbar^2}{\beta^2 m_e} \cdot n_e \cdot \left(\ln\frac{T_{max}}{T_{min}} - \beta^2\right)$

Incoherent scattering with all shell electrons:
$n_e = Z\rho/V = Z\rho\frac{N_A}{A}$

Step 2: Minimum energy transfer T_{min}

Account for quantim mechanical effects
- minimum ionazation energy of the atom
- shielding of electric field of inner electrons due to outer ones
- small projectile energy, i.e. low velocity

→ Let others do it...

$$T_{min} = \frac{I^2}{2m_e c^2\beta^2\gamma^2}$$

Here, I is the mean excitation energy of the atom

γ^2 in the denominator describes effect of Lorentz transformation of projectile electric field
→ relativistic increase of energy loss for high energy projectiles

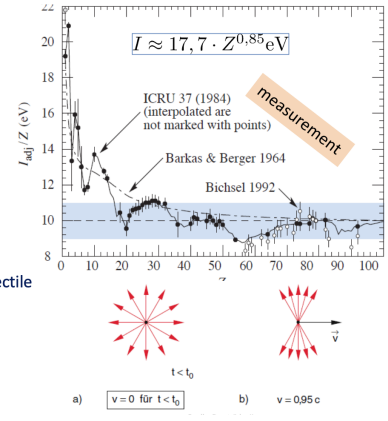

Energy Dependence of $\frac{dE}{dx}$

We typically quote $\frac{1}{\rho}\frac{dE}{dx}$

$$\Rightarrow \left[\frac{1}{\rho}\frac{dE}{dx}\right] = \frac{\mathrm{MeV cm}^2}{\mathrm{g}}$$

Mass Stopping Power or Massenbremsvermögen

→ (nearly) independent from target material

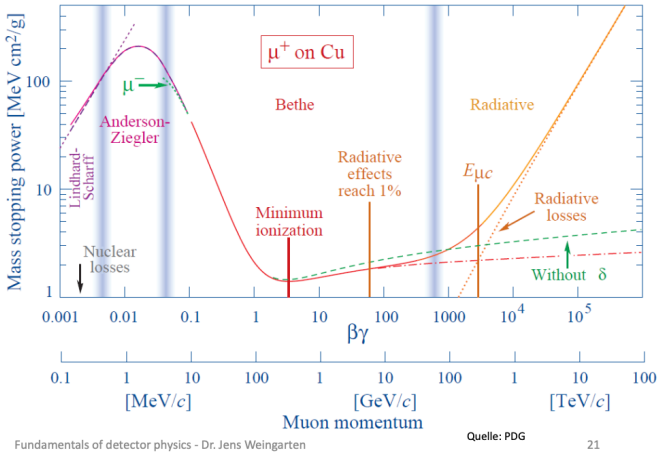

Quelle: PDG

Low Energy ($\beta\gamma < 0.95$)

- **Energy loss** $\propto \frac{1}{\beta^2}$:
  - Momentum transfer increases with longer interaction time ($\Delta t \approx b/\gamma v$).
  - At very low energy, elastic scattering dominates until the projectile is thermalized.

Minimum ($\beta\gamma \approx 3 \ldots 3.5$)

- **Wide minimum**: Energy loss is similar in most materials, with $\frac{1}{\rho}\frac{dE}{dx} \approx 1 \cdots 2\ \mathrm{MeV cm}^2/\mathrm{g}$.

High Energy

- **Energy loss** $\propto \ln\gamma$:
  - Maximum energy transfer increases $\propto \gamma$.
  - Relativistic effects and medium polarization slow the increase of $\frac{dE}{dx}$. PLUS relativistic expansion of the transverse component of the E-field increases the maximum impact parameter -> effect reduced by polarisation of medium (density correction)
  - Energy loss increases beyond the minimum by about 30%.

At high energy, projectiles also lose energy via Bremsstrahlung:

$$\frac{dW}{dt} \propto \ddot{\vec{x}}^2 \propto \frac{z^2 Z^2 e^2}{m^2} \xrightarrow{v \to c} \frac{E}{m^2}$$

- **Critical energy**: Kinetic energy where ionization energy loss equals Bremsstrahlung energy loss.
- **Significant for electrons/positrons**: For typical energies (< 100 GeV), Bremsstrahlung is significant primarily for these particles.

Energy loss per particle

Bethe-Bloch describes mean energy loss for many partices
→ large fluctuations per particle, due to stochastic nature of processes
→ per particle the energy loss distribution depends on material thickness
- thick layer: Gaussian (central limit theorem)
- thin layer: Landau-(Vavilov) distribution
  → tail towards large energy loss

Delta-Elektronen
central impact on shell electron
→ maximum energy transfer

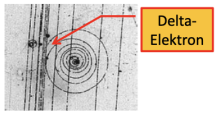

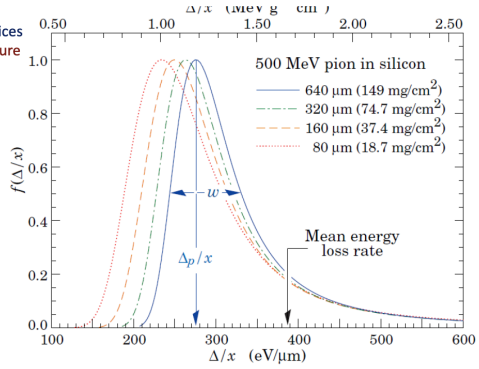

Multiple Coulomb scattering

Charged particles can scatter with the nucleus of the target material → (nearly) no energy loss, but change of direction If particle traverses a thickness Δx, this happens a lot → multiple Coulomb scattering (MCS) → scattering angle distribution

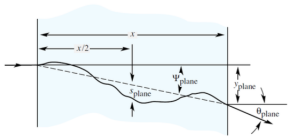

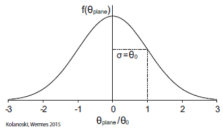

Exact description by Molière, Gaussian approximation of scattering angle distribution often good enough → characterized by $\sigma = \theta_0$

Parametrization of θ_0 in Highland formula

$$\theta_0 = \frac{13.6\mathrm{MeV/c}}{\beta pc} \cdot z \cdot \sqrt{\frac{x}{X_0}} \left(1 + 0.038 \ln \frac{x}{X_0}\right)$$

→ scattering angle depends on thickness of the material $\mathrm{x/X_0}$ (normalized to, radiation length) and momentum of the particle

LT2

Signal generation in detectors

Signal in detectors

Last week we talked about ionization with the Bethe Bloch formula but how this lead to a measurable signal?

Ionization:

- **Direct**: charged particles interact e.m. with shell electrons
- **Indirect**: neutral particles generate charged particle via other processes, these charged particle ionise

These carriers, comprising pairs of electrons and ions, move towards the electrodes within the detector. Their motion creates a time-dependent mirror charge, influencing the electrical current within the system.
Hence, ionization leads to the generation of a detectable signal.

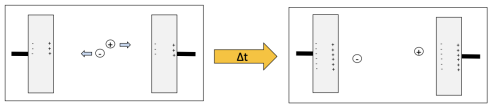

To understand how charges traverse within the detector, we need to consider two primary processes:: **diffusion** and **drift**

1. **Diffusion**
   A random, unordered motion with a velocity distribution which—in thermal equilib- rium and without external fields—is classically described by the Maxwell–Boltzmann distribution1. An external electric field can 'heat up' the carrier motion and hence change the distribution.
   Is a Brownian motion, meaning that is like a random walk, and if you imagine a random walk of particles you will notes effetct in movements in concentration gradients. This distribution tends towards a 3D Gaussian charge pattern, influenced by the concentration gradient.
   The speed of this diffusion is described by this formula

$$v_{Diff} = \bar{v} = \sqrt{\frac{8kT}{\pi \cdot m}} \quad \text{At room temperature} \quad \begin{matrix} v_{Diff}(e^-) \approx 10^6\ \mathrm{cm/s} \\ v_{Diff}(Ion) \approx 10^4\ \mathrm{cm/s} \end{matrix}$$

   For the ion is much slower because the size and **mass** of the nucleus.

   Fick's law describe that particle current density J is proportional to the gradient of the concentration

$$\vec{j}_D = -D\vec{\nabla}\rho \quad \text{With diffusion constant (material property)}$$

$$D = \frac{\lambda^2}{\tau}$$

Mean free path

Time between two collisions

If we should imagine how this diffusion moves -> *It follows the concentration gradient*.
The temporal evolution of the charge distribution $\rho(r)$ follows the continuation equation

$$\frac{\partial \rho}{\partial t} - D\Delta\rho = 0$$

When the diffusion is isotropic, then starting from a point like charge distribution, we expect after the time t a 3D Gaussian charge distribution

$$\rho(\vec{r},t) = \frac{N}{(4\pi Dt)^{3/2}} \exp\left(-\frac{\vec{r}^2}{4Dt}\right) \text{ mit } \sigma_x = \sigma_y = \sigma_z = \sqrt{2Dt}$$

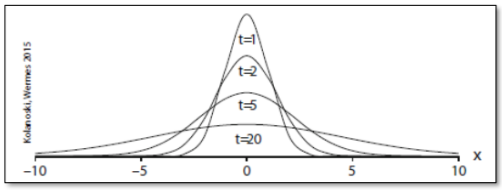

2. **Drift**

A drift motion whose direction is determined by the external electric and magnetic fields.

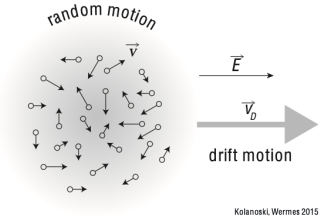

Fig. 4.1 Schematic illustration of the random, unordered motion of particles in a charge cloud and the superimposed drift motion in the direction of the electric field.

The drift velocity v_D results from an equilibrium between the accelerating electric force and a damping or friction force arising from collisions with surrounding atoms and molecules.

a) Drift in the electric field:

The drift velocity $\vec{v}_D$ depends on the mobility μ of charge carriers and the strength of the electric field $\vec{E}$.

$$\vec{v}_{Drift} = \frac{e}{m}\tau\vec{E} \cdot \frac{p_0}{p} := \mu\vec{E} \cdot \frac{p_0}{p}$$

With the mean time between two collisions $\tau = \tau(\vec{E},\sigma)$ and the mobility μ, which is a material property.

Medium	Charge carrier	typ. v_{Drift}
Gas	electrons	5 cm/µs
	ions	5 cm/ms
Silicon	electrons	10 cm/µs
	holes	3 cm/µs

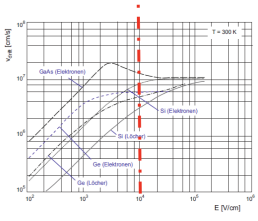

Mobility in gases strongly depends on mean molecule size (Ramsauer-

effect)-> strong variation of drift velocity as function as function of drift gas composition

Electrons in Ar + Methane and Ar + Ethan

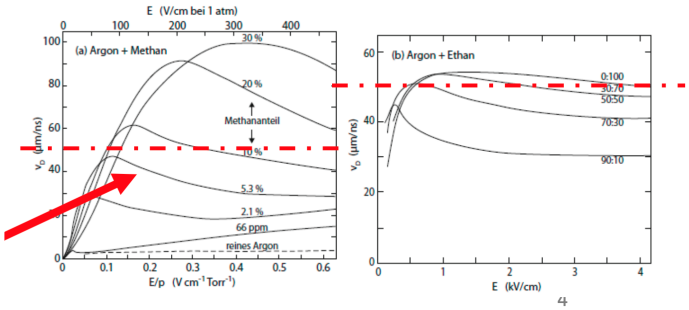

4

b) Drift in the magnetic field:

Coulomb force and Lorentz force act on the charge carriers

$$\vec{F}_{Coulomb} = q\vec{E} \quad \vec{F}_{Lorentz} = q\left(\vec{v} \times \vec{B}\right)$$

So the charge carrier gets deflected with a Lorentz angle.
So we will have a new drift velocity:

$$\vec{v}_{Drift} = \frac{\mu}{1+\omega^2\tau^2}\left(\vec{E} + \frac{\vec{E}\times\vec{B}}{B}\omega t + \frac{(\vec{E}\cdot\vec{B})\cdot\vec{B}}{B^2}\omega^2\tau^2\right)$$

Mobility $\mu = \frac{e}{m}\tau$

Special case: $E \perp B$:

Here, charge carriers follow a spiral path around the magnetic field lines. The radius of this spiral path (rr) is determined by the ratio of the transverse velocity (vTvT) to the cyclotron frequency ($\omega\omega$). In this configuration, transverse diffusion is suppressed, and the width of the charge cloud is significantly reduced, especially for large drift times. This effect is particularly crucial in devices like Time Projection Chambers.

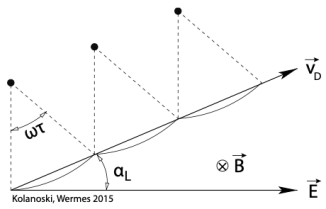

Fig. 4.4 Descriptive explanation of the Lorentz angle. The electron moves in the magnetic field on a curved orbit, here presented by a segment of a circle. During the collision time τ the electron has turned its direction by the angle $\omega\tau$. After each collision follows a similar segment of a circle if one assumes that the velocity vector vanishes on average after a collision. In contrast to this simplified picture, however, the segments are stochastically distributed. The whole sequence of such microscopic orbit segments yields a macroscopic change in the drift direction with respect to the direction of the electric field by the Lorentz angle α_L.

Special case: $E \parallel B$:
Carge carriers follow spiral path around B-field lines $r = \frac{v_T}{\omega}$. In this case transvers diffusion is suppressed and on top of all that the width of charge cloud gets strongly reduced for large drift times (TIme Projection Chamber!)

Saturation of drift velocity: Langevin equation

$$m\frac{d\vec{v}_{Drift}}{dt} = e(\vec{E} + \vec{v}_{Drift} \times \vec{B}) - K \cdot \vec{v}_{Drift} \quad \text{with } K = \frac{m}{\tau}$$

Friction caused by collisions

➔ Leads to constant drift velocity for $t >> \tau$

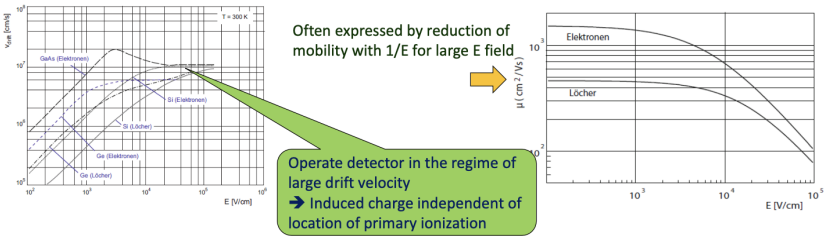

16.04.2024 Detectors 6

Influence

Charges influence mirror charges on the electrodes.
As charge carriers traverse the detector medium, their motion perturbs the distribution of charges on the electrodes. This interaction isn't static but evolves over time as charge carriers progress through the detector volume.

When electrodes are interconnected in a circuit, typically facilitated by a voltage source generating an electric field ((E)), the charges on the electrodes undergo *redistribution*. This redistribution process, known as **equilibration**, is driven by the applied electric field and aims to establish a stable charge distribution within the circuit.

The *culmination of this dynamic interaction* and equilibration process is the generation of a measurable current, often referred to as the **signal**.

Several consequences arise from this dynamic interplay:

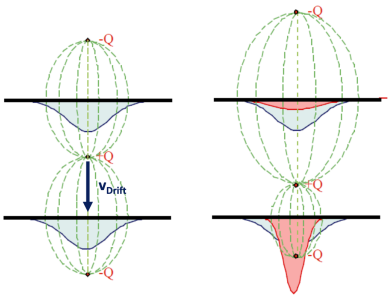

- The proximity of the primary charge to electrodes influences the magnitude of its influence on the mirror charges. Closer proximity results in a stronger influence, amplifying the signal.
- Current measurement it's immediate upon the initiation of charge carrier movement. This real-time measurement capability facilitates swift analysis of charge carrier dynamics.
  - The traditional concept of "charge collection" may oversimplify the process, as the measurable current reflects ongoing interaction rather than just the moment of charge collection.
- When the primary charge ceases its movement, the current = 0, signifying the cessation of interaction between charge carriers and electrodes.

- **Current depends on the speed of the primary charge, i.e. drift velocity, and the coupling strength to the electrodes**

Influence of external voltage and charge movement on the charges at the electrodes.

System Representation:
Consider a simplified system with two electrodes, symbolizing the essence of the detector setup. One electrode represents the electric field in the absence of charge but connected to an external voltage (U), while the other reflects the electric field generated by the charge. Together, they illustrate the superposition of these fields within the detector.

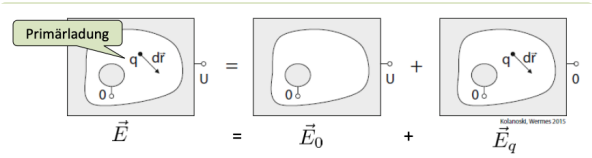

Influenced Charge at Electrodes:
The application of an external voltage U induces an influenced charge $+Q$ or $-Q$ at the electrodes.
This induced charge $Q = C \cdot U$, where (C) denotes capacitance) sets the stage for further interaction. As the primary charge (q) moves within the detector, it influences additional charge ($dQ(\vec{r}_q)$) at its location ($\vec{r}_q$).

The crucial question arises: How significant is this additional charge?

Work Done and Energy Conservation:
As the charge q traverses the detector, the external electric field $\vec{E}_0$ performs work

$$dW_q = q\vec{E}_0 d\vec{r}$$

This work, in turn, is subject to the principles of energy conservation. The total work done

$$dW_q + dW_U + dW_E = 0$$

incorporates contributions from the external voltage $dW_U = dQ \cdot U = q \cdot dU$ and the field

$$dW_E = 0$$

Indeed we can show (Greens theorem), that neither $\vec{E}_0$ nor $\vec{E}_q$ transfer energy to the charge q: $dW_E = 0$

$$dW_q + dW_U = q\vec{E}_0 d\vec{r} + dQ \cdot U = 0 \quad \rightarrow \quad dQ = -q\frac{\vec{E}_0}{U} d\vec{r}$$

where dQ is the influenced charge at the electrode.

BUT we still miss the field $\vec{E}_0$, or $\frac{\vec{E}_0}{U} = \vec{E}_w$, the so called weighting field.

The field $\vec{E}_0$ is given by the geometry of the electrodes and its value is proportional to U -> $\frac{\vec{E}_0}{U}$ and therefore

-> **the influenced charge dQ is independant of U**

Weighting Potential and Signal Calculation:
For further calculation by defining U = 1, we establish a reference point for the weighting potential $\phi_w = \frac{\phi_0}{U}$ and the weighting field $\vec{E}_w = -\vec{\nabla}\phi_w$.

Leveraging the weighting field, we use $\vec{E}_w$ to calculate the current signal:

$$dQ = -q\vec{E}_w d\vec{r} \quad \rightarrow \quad i_S = -\frac{dQ}{dt} = q\vec{E}_w\vec{v}$$
$$with \quad \vec{v} = \frac{d\vec{r}}{dt} = \vec{v}_{\text{Drift}}$$

Shockley-Ramo Theorem

Nota bene: the concept of weighting field is more than dividing E by U, especially in a multi electrode system.
Setup with k electrodes connected with potentials U1, U2,…, Uk.
How does E_W looks like?

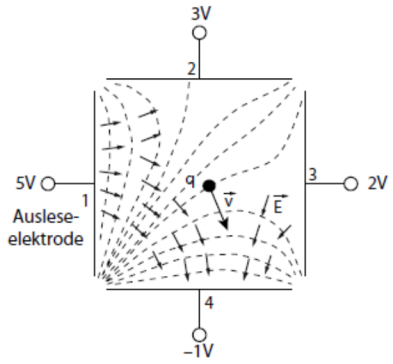

We consider an arrangement of k electrodes to which voltages $V_1, V_2, \ldots, V_k$ are applied. Thanks to the superposition principle the potential generated by the electrodes $\phi_0(\vec{r})$ in the space between the electrodes can be represented by a sum over different configurations of potentials $\phi_i (i = 1, \ldots, k)$. For each configuration i all electrodes remain at a potential 0 except for the potential of the electrode i which lies on its actual voltage V_i:

$$\phi_0(\vec{r}) = \sum_{i=1}^{k} \phi_i(\vec{r}), \quad \text{with} \quad \begin{matrix} \phi_i|_{S_i} = V_i, \\ \phi_i|_{S_j} = 0, j \neq i. \end{matrix}$$

That is

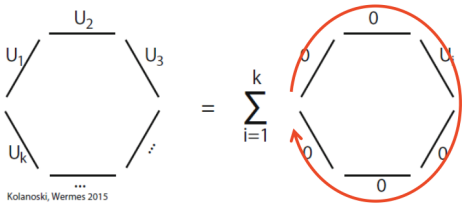

The weighting potential and weighting field, respectively, for each configuration i are

$$\phi_{w,i}(\vec{r}) = \frac{\phi_i(\vec{r})}{V_i}, \quad \vec{E}_{w,i} = -\vec{\nabla}\phi_{wi}.$$

Each weighting potential $\phi_{w,i}$ individually fulfils the Laplace equation with the above defined boundary conditions $V_i = 1$ and all other $V_{j\neq i} = 0$:

$$\Delta\phi_{w,i}(\vec{r}) = 0, \quad \text{with} \quad \phi_{w,i}|_{S_i} = 1, \quad \phi_{w,i}|_{S_{j\neq i}} = 0.$$

Shockley-Ramo theorem: states that the signal induced by a moving charge q on an electrode i is given by the weighting potential or the weighting field of the potential configuration $\phi_i(\vec{r})$:

$$dQ_i = -q\vec{E}_{w,i}d\vec{r} \qquad \text{For Sign. Charge}$$
$$i_{S,i} = q\vec{E}_{w,i}\vec{v} \qquad \text{For Sign. Current}$$

→ Signal only depends indirectly on applied voltage!

The ShockleyRamo theorem implies that the signals dQ_i or $i_{S,i}$ on an electrode do not directly depend on the strength of the electric field between the electrodes or on the applied high voltage. However, the electrical field usually determines the direction and the velocity of the charge motion and thus according to the Shockley-Ramo theorem the signal shape. The weighting field $\vec{E}_{w,i}$, which depends only on the geometry of the arrangement, determines the signal on the electrode i generated by the movement of the charge with the size and sign of the signal current being proportional to the velocity component in the field direction.

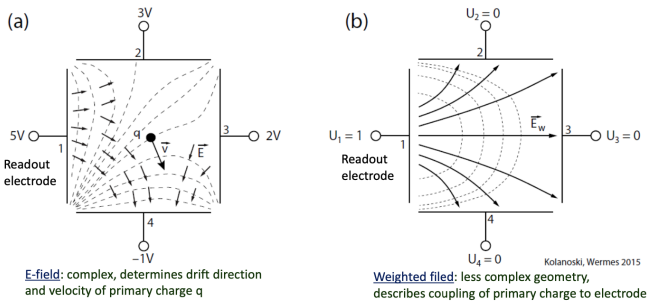

The Figure shows an example with four electrodes. The weighting field and the actual electric field, and thus the direction of motion of the charge, have different orientations at the position of the charge. If in addition space

charges are present, as in semiconductor detectors, then even in two-electrode systems the weighting and electric fields are no longer proportional.

Central Message

1. The electric field determines the velocity and the trajectory of the charge carriers inside the sensor volume. To determine these quantities the E-field must be determined with the help of the Gaussian theorem.
2. The weighted field is determined by the electrode geometry alone and tells, how the drifting charge couples to the electrodes and how there charge is influenced.
3. Only in two electrode setups the weighted field and the electric field have the same shape. Even here they are not identical but just proportional to each other!

How to calculate the signal current:

1. Determine the weighted filed of the electrode in question $\vec{E}_{w,i}$
2. Determine the velocity and the direction of the drifting charge $\vec{v}_{Drift}$
3. Use the above to calculate the signal current $i_{S,i}(t) = q\vec{E}_{w,i}\vec{v}_{Drift}$

Examples of weighted fields

1. Flat capacitor
   In a parallel plate capacitor with homogeneous space charge the electric field increases linearly with the distance x from an electrode as $E \propto x$. In contrast the weighting field remains constant, given as $E_w = 1/d$ where d is the electrode distance.

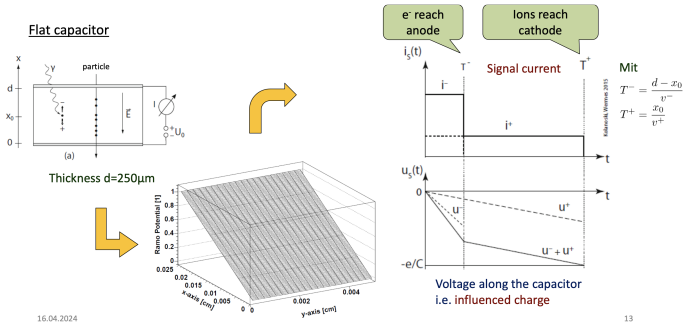

2. Semiconductor strip detectors
   It's a silicon strip detector with p and n regions. The geometric setup of the detector it's quite important

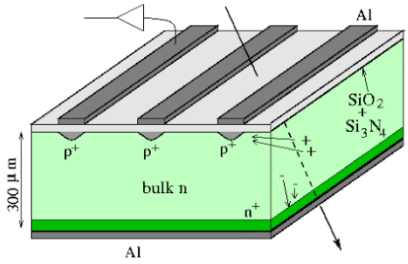

   Let's look at the potential plot, and eventually also the elctri fiels is this

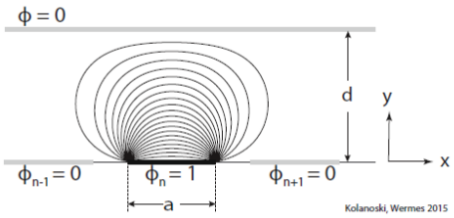

the result of the detectr will be determined by the fraciton between the strip width and the sensor thickness

$$a := \frac{strip\ width}{sensor\ thickness}$$

And if we change the a the value of the ϕ will change a lot because the strips will influence each other

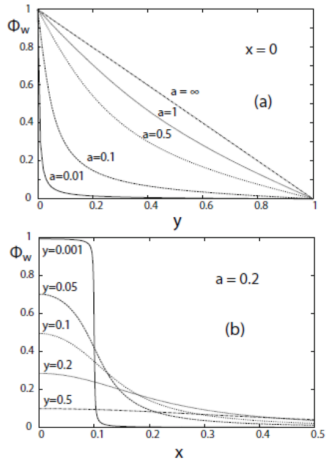

For segmented electrodes neighbours have to be accounted for! Of course the strips can share the signal of a track since they are near to each other.

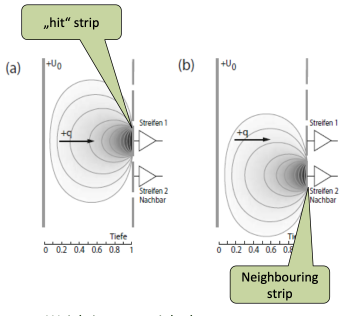

Here we can see the current and charge (in a row) for the strip 1 and the same for strip 2.

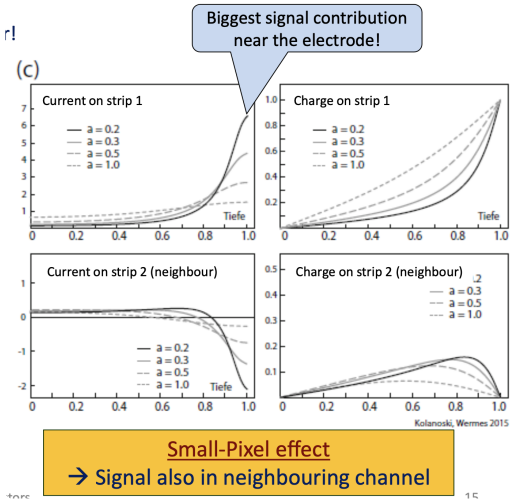

Example: signal current

Drift signals from exclusively electrons or (XOR) holes in silicon.

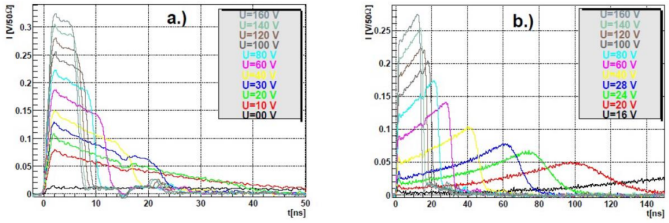

Electron signal Hole signal

Here you see that the current signal on the x there is the time and on the y the current. In the case of the electron (on the left) you see that is really fast the signal, and the holes are slower (because more spread in time)
Also we can see that for the electron the drift will be quire fast if the U is bigger and slow drift velocity if you decrease the voltages.
For the holes we have a **bigger** x values. There is a completely different behaviour. If we look at the green signal we see that it increases till a peak and than decrease.
The difference than is basically that the peak comes later for holes because they are slower.

Readout Electronics

Current pulse has to be digitized prior further processing, we need the **readout electronics**.

We Pick up the current signal from the sensor, then we amplify the signal (pulse shaping, discrimination) and then we do optimization of the output signal depends on application.
The tasks of the readout electronics in a detector system can be summarised as follows:

- electronic coupling to the detector to receive the detector signal
- amplification of the input signal and electronic processing (pulse shaping, discrimination);
- optimisation of the output signal depending on the application regarding
  - signal-to-noise ratio,
  - determination of the primary deposited energy in the detector (energy measurement),
  - determination of a precision mark of the signal arrival time (time measurement),
  - rate tolerance;
- digitisation and storage (buffering) of the output signal.

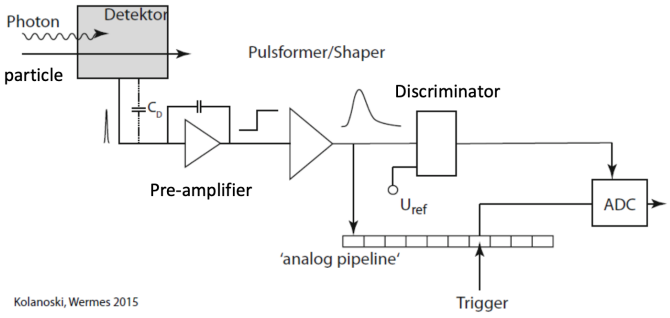

After the preamplifier we can see the Heaviside signal, then we give it a shape with the shaper and then we put it in the discriminator to compare the hight of the signal. We can store the signal after the shaper into a pipeline and we sae also the trigger to say if we have to save or not the entire pipeline.

The signal

We use the figure, which displays an individual example pulse (e.g. the output of a detector or a photomultiplier upon a detected photon or particle) to introduce some quantities for pulse characterisation. Such a pulse could for example be a drift chamber signal or the output of a photomultiplier on an oscilloscope

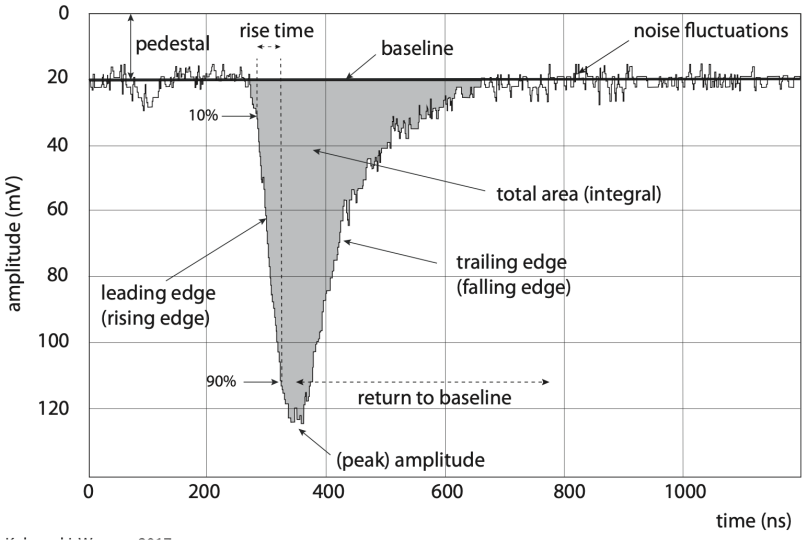

Assuming that the signal generation in the detector is short compared to the electronic processing times, which is a typical but not an always given case, an electronic pulse is characterised by the following quantities:

- The peak amplitude is the maximum pulse amplitude, also called pulse height. In linear systems its value is proportional to the primary deposited energy in the de- tector.
- The peaking time is the position of the peak amplitude in time.
- The area or pulse integral is the integral over the pulse shape. In linear systems and for short, δ-like signals, its value should be proportional to the primary deposited energy.
- The pulse width is the width of the pulse, usually defined as the full width at half maximum (FWHM).
- Leading and trailing edges are the rising and falling slopes of the pulse.
- The rise time characterises the steepness of the pulse’s rise. It is commonly defined as the time needed for the pulse to rise from 10% to 90% of its peak amplitude, but other definitions also exist.
- The slew rate indicates the voltage change per time dV/dt in units V/s.
- The baseline or pedestal value is the output value upon zero input. It defines the ‘zero’ level from which to measure the signal height. Although the baseline usually has a fixed value, deviations can occur for some (short) time. They are called baseline shifts.

Amplifier

Detector signals can be very small, in the nanoampere, femtocoulomb or microvolt range, and must be (pre)amplified before the data can be read out for further processing. Operational amplifiers (OpAmps) are commonly used for this purpose due to their high internal gain and versatile behavior determined by external circuit elements. In an ideal scenario, the open-loop gain of an OpAmp is infinite, but in practice, it's limited and frequency-dependent.

OpAmps have two voltage inputs and one output, and their operation can be described by two fundamental rules:

1. the output adjusts to nullify the voltage difference between the inputs
2. the inputs draw negligible current.

These rules make it possible to design various amplifier configurations tailored to specific needs, such as

- voltage amplifiers
- current amplifiers
- transconductance amplifiers
- transimpedance amplifiers
- and charge amplifiers.

The charge amplifier (Q → V) or charge-sensitive amplifier (CSA) shown in figure below is often used for detector readout, in particular when the signal-to-noise ratio for a detector is small.

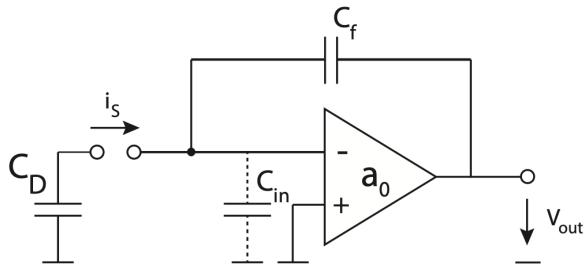

(b) Capacitive feedback.

This amplifier type can, for example, be realised by an (inverting) OpAmp with capacitive feedback (integrator). The signal current is integrated on the feedback capacitor Cf:

$$v_{\text{out}}(t) = -a_0 v_{in}(t) = -\frac{1}{C_f}\int_0^t i_S dt' = -\frac{Q_S(t)}{C_f}.$$

Over the feedback capacitor we have the voltage difference

$$v_f = v_{\text{in}} - v_{\text{out}} = v_{\text{in}}\,(a_0+1) = \frac{Q_f}{C_f}.$$

The charge Q_f on C_f is equal to the signal charge Q_S since no current flows into the OpAmp:

$$Q_S = Q_f = C_f\,(a_0+1)v_{in}$$

The amplifier hence has a 'dynamic' input capacitance

$$C_{in} = \frac{Q_S}{v_{in}} = C_f\,(a_0+1).$$

For large internal (open loop) gain a_0, we usually have $C_{in} \gg C_D$ and the charge amplification $A_Q = v_{\text{out}}/Q_S$ only depends on the capacitance C_f of the feedback capacitor and not on the detector capacitance C_D (see below):

$$A_Q = \left| \frac{v_{\text{out}}}{Q_S} \right| = \frac{a_0 v_{\text{in}}}{(C_D + C_{\text{in}})v_{\text{in}}} \approx \frac{a_0}{C_{\text{in}}} = \frac{a_0}{a_0+1}\frac{1}{C_f} \approx \frac{1}{C_f}.$$

The smaller the feedback capacitance C_f the larger is A_Q.

Frequency behaviour:*
Only an ideal integrator delivers a step function at the output which corresponds to an infinitely large bandwidth, which means that all frequencies are amplified equally.
Real amplifiers have limited bandwidths, resulting in finite output rise times. Its time response can be described by a single time constant τ.

The response in the frequency domain is shown in the fig below also in the time domain:

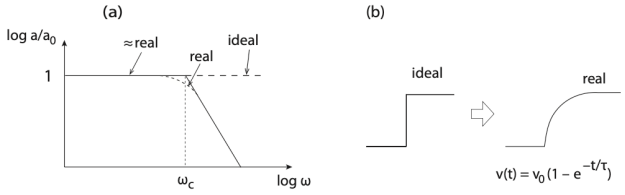

Using ω = 2πf, f =frequency, the dependence is given as

$$a(\omega) = -\frac{v_{\text{out}}}{v_{\text{in}}} = -\frac{i_{\text{out}}}{v_{\text{in}}}(r_0 \| C_0) = -g_m \frac{r_0}{1 + i\omega r_0 C_0} = \frac{a_0}{1 + i\frac{\omega}{\omega_c}},$$

where r_0 combines the two resistors r_{ds} (drain-source resistor of the transistor) and r_{0i} (resistor of the current source), while $g_m = i_{\text{out}}/v_{in}$ is the transconductance of the amplification transistor; $r_0 \| C_0$ denotes a parallel configuration of the corresponding impedances. The last equal sign uses the fact that in the DC-limit $(\omega \to 0)$ the open loop gain reads

$$a_0 = -\frac{v_{\text{out}}}{v_{\text{in}}} = -\frac{i_{\text{out}}}{v_{\text{in}}} r_0 = -g_m r_0$$

and introduces the cut-off frequency

$$\omega_c = \frac{1}{r_0 C_0}$$

corresponding to a time constant $\tau_0 = r_0 C_0$ which describes the rising edge of the output pulse in the time domain:

$$v_{\text{out}} = v_0 \left(1 - \mathrm{e}^{-t/\tau_0}\right).$$

Discharging Cf:
In the ideal case the charge seen at the input of the preamplifier is

integrated on Cf and the corresponding voltage value v_{out} is seen at the output.

For every newly arriving signal at the preamplifier input additional charge is added: The output voltage jumps accordingly by a value Δv_{out}. For subsequent pulses corresponding voltage steps appear at the output. At a certain amount of charge the limit of the dynamic range of the CSA is reached and the amplifier output saturates. The feedback capacitor, therefore, must be discharged in order that the system remains operative.

Several reset techniques are in use:

- discharging by a (transistor) switch:

By closing the switch the capacitor is discharged and the preamplifier is reset, ready for new signals. This method becomes problematic for high signal rates when high reset frequencies generate sharp transient pulses (switching noise).

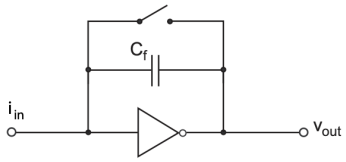

(a) Switch reset: circuit.

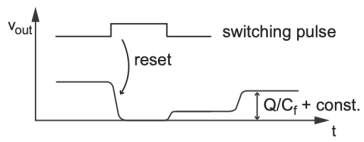

(b) Switch reset: output voltage.

- discharging with a resistor:

No switching is needed when the feedback capacitor Cf is discharged by a resistor. As soon as a signal pulse arrives the capacitor is discharged through the resistor with an exponential characteristic with (discharge) time constant $\tau_d = C_f R_f$. No external control is needed.
In particular at high signal rates a decay time as short as possible is desired to avoid superposition of signals at the output of the amplifier. Short time constants, on the other hand, increase the thermal noise contribution of the system. The time constants for discharging Cf through a resistor can be as large as 10–100 µs, for example in detector applications for spectroscopic measurements which require very low noise.

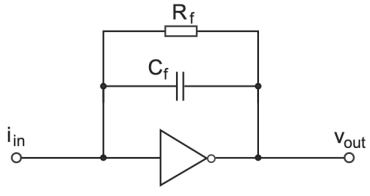

(c) Reset via resistor: circuit.

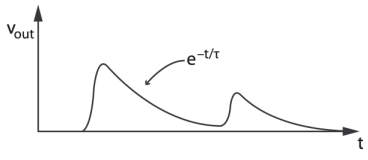

(d) Reset via resistor: output voltage.

- discharging by a constant current source:

In contrast to resistor discharging, the capacitor is here discharged by a constant current. This also results in a linear decrease with constant slope of the pulse after having reached the peak amplitude. The output pulse has a triangular shape. Its width in time Δt is proportional to the peak height as

well as to the total area of the pulse. A measurement of the time during which the output pulse is larger than a given threshold value hence is a measurement of the corresponding total signal, which itself is proportional to the energy deposited in the detector. This is a convenient and simple method to measure the pulse integral, called the time-over- threshold (**ToT**) method

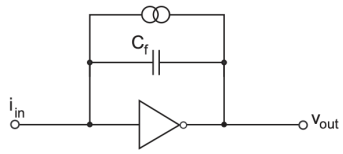

(e) Reset via current source: circuit diagram.

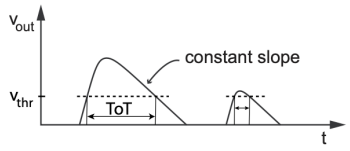

(f) Reset via current source: output voltage.

Pulse shaping

Further pulse processing is necessary
(a) to avoid pulse superposition (pile-up)
(b) to reduce noise by frequency filtering.

As described in the previous section, the feedback capacitor in the preamplifier must be discharged to avoid spurious superposition of output signals.

Typical decay times of electronic pulses of a preamplifier are in the range of some 10ns to about 10µs. If further signals arrive during the decay time, pile-up of pulses at the output still occurs despite discharging. The superimposed signals can be separated by an RC high-pass filter. A combination with an additional low-pass filter or even several high- and low-pass stages leads to more or less Gaussian shapes of the output pulses for every signal pulse at the input.

This electronic circuitry is hence called pulse former or **shaper**.

In practice the preamplifier output signals are superposed by noise signals which contributes at all frequencies (white noise).
To increase the SNR one can filter parts of the frequency spectrum.

Figure:
Readout system consisting of *detector*, *preamplifier* and *shaper*.

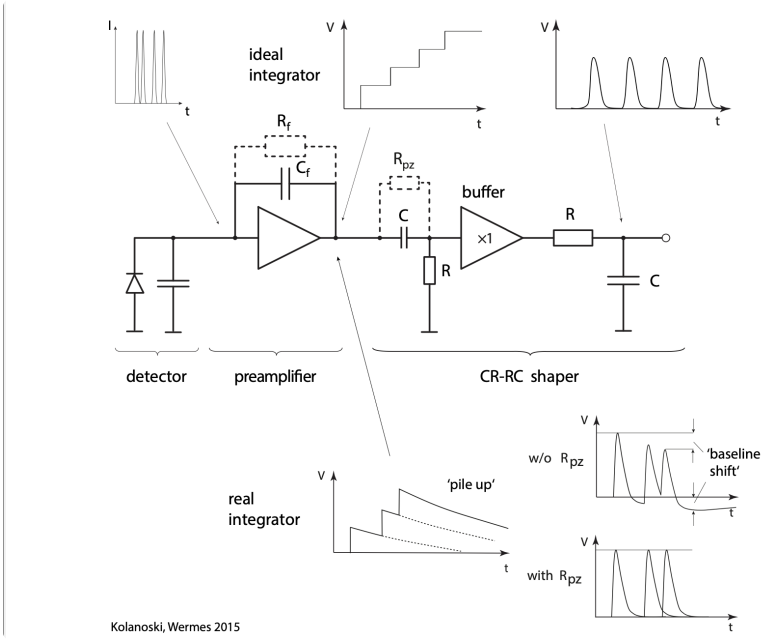

The pulse shapes at input and output of the preamplifier and at the output of the shaper are drawn at the top part of the figure for an ideal case (step functions without discharging) and at the bottom part for a real case (discharging of Cf , here by a resistor Rf , dashed). In the latter case an 'undershoot' develops at the shaper output.

By the resistor R_{pz} parallel to the capacitor of the high-pass filter (dashed) the undershoot is compensated (pole-zero cancellation).

The (×1)-amplifier in between the band-pass parts is a buffer preventing the low pass from supplying a real load to the high pass.

Balsiti Deficit:
Another problem appears if the pulse evolution (with time) at the shaper input lasts much longer than the high-pass time constant of the shaper. The former can be caused by a large charge collection time, for example when the drift velocity of charge carriers is slow, by a large input capacitance or also by an intrinsically slow preamplifier. In such a case the output amplitude of the shaper is trimmed by the slow rise of the preamplifier pulse. The falling edge of the shaper output already sets in before the preamplifier output has reached its maximum value. This problem is commonly called shaping loss or ballistic deficit.

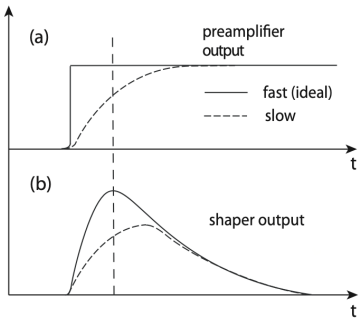

Fig. 17.15 Shaping loss: (a) step function pulse (without discharge) at the preamplifier output with a fast (solid line) and a slow rise (dashed line). (b) Resulting shaper output. If the shaper peaking time is short in comparison to the rise time of the preamplifier an amplitude loss occurs (*shaping loss* or *ballistic deficit*).

Discriminator

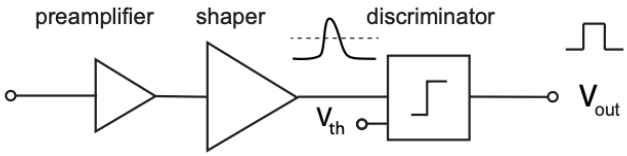

(a) Readout system with amplifier, shaper, and discriminator.

For a measurement one wants to distinguish real signals, generated for example by particles, from noise hits caused by electronic fluctuations and to suppress the latter.

A discriminator decides if an input pulse surpasses a set (voltage) threshold and, if so, generates a rectangular output pulse, usually in a logic standard. This way noise hits with amplitudes below the threshold are filtered out. At the same time digital output signals are created from analog inputs that can be used in further processing logic. Discriminators are particularly used also for gating and triggering of other parts of the electronics chain. Discriminator signals can for example control data recording of an oscilloscope (discriminator pulse on the trigger input of the oscilloscope) or of a multi-channel analyser (MCA, discriminator signal on gate input of the MCA) or they can be used as logic signals in subsequent electronic logic gates.

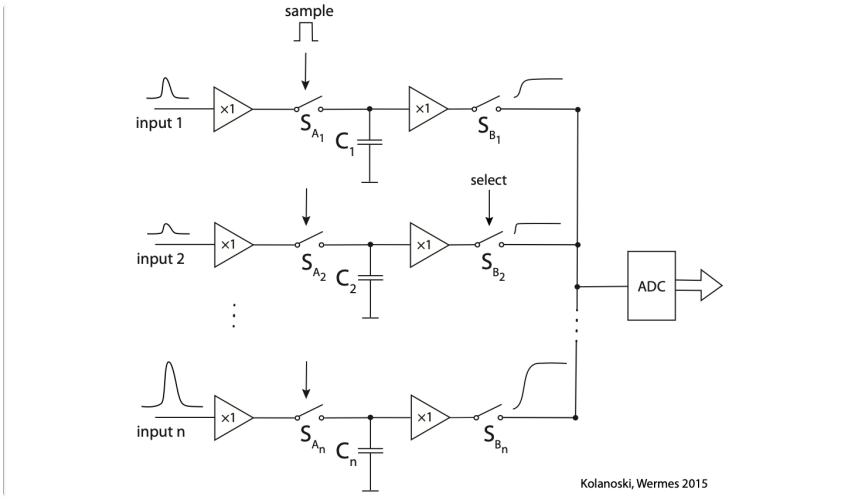

Time walk

In time-critical applications the problem of time walk is encountered for input pulses of different height. For different peak amplitudes at the discriminator input the output pulses are issued at different times depending on when the input pulse crosses the threshold. Figures below show how the response time depends on the pulse height of the input signals.

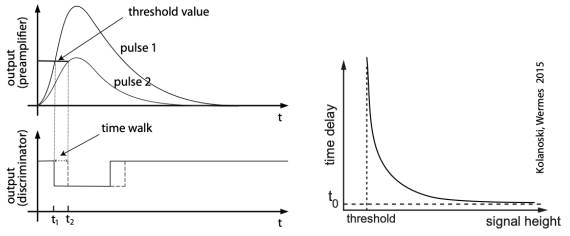

(b) Time walk.

(c) Dependence of time walk on the signal pulse height (schematic).

Specifically time walk occurs when the timing of output pulses from a discriminator is not solely determined by the arrival time of the input pulse, but also by its amplitude. Essentially, the discriminator's response time depends on the height or amplitude of the input pulses. When high-amplitude pulses are detected, the discriminator tends to respond more quickly, resulting in earlier output pulses. Conversely, low-amplitude pulses trigger delayed output pulses. This variation in timing can introduce timing errors, especially in applications where precise synchronization is essential, such as in high-speed data transmission or particle detection systems.

So for a simple discriminator the hit time depends on the signal amplitude (time walk).

Summary:

Discriminate signal from noise → discriminator

Output logic low if $u_{out}^{shaper}(t) < u_{thr}$
high if $u_{out}^{shaper}(t) > u_{thr}$

Discriminator output is a logic signal
→ ready for digital processing

Constant-fraction discrimination:

It was empirically found that for leading-edge discrimination the best timing resolutions are obtained if the threshold is set at about 10–20% of the pulse peak amplitude.
This has led to an extended method that generates a time mark by issuing an output pulse when reaching a predefined fraction k (constant fraction) of the peak amplitude. This point in time is independent of the absolute pulse height as long as the rising edge of the pulse is unchanged in shape:

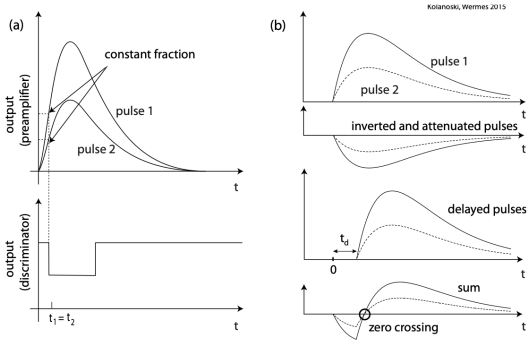

Fig. 17.19 *Constant-fraction triggering* features small timing fluctuations for pulses with constant shape. (a) Two pulses of different height are discriminated at a fixed peak-amplitude fraction; top: pulse shape, bottom: output of the discriminator, constant in time. (b) Electronic realisation: an inverted and attenuated pulse is superimposed on the delayed pulse. From top to bottom: two output pulses of different size; inverted and attenuated pulses; delayed pulses; addition of inverted and delayed pulses yielding with constant zero-crossing point.

The electronic realisation of constant-fraction discrimination is shown in fig(b).

The output pulse is split and in one branch inverted and attenuated by a fraction k < 1. In the other branch the output pulse is delayed by a time td, which must be smaller than (1 – k)tpeak , where tpeak is the peaking time of the pulse. The pulses of both branches are then superimposed:

$$v_{sum}(t) = v_{in}(t - t_{in}) - kv_{in}(t)$$

The zero-crossing point depends on the constant fraction k (not on the signal amplitude) by which the original pulse is attenuated. The method exhibits comparatively small timing fluctuations (typically 10–30 ps) over a large range of amplitudes.

Detector signal readout: Graphical summary

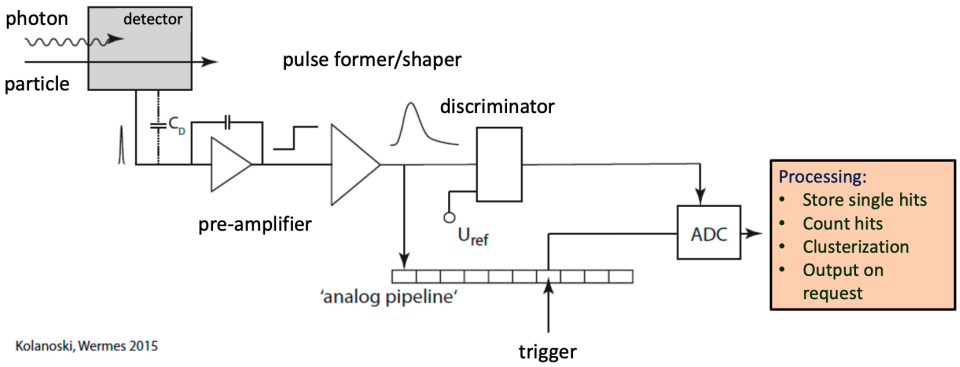

- Trigger decision is made with help of other detectors

Example LHCb detector

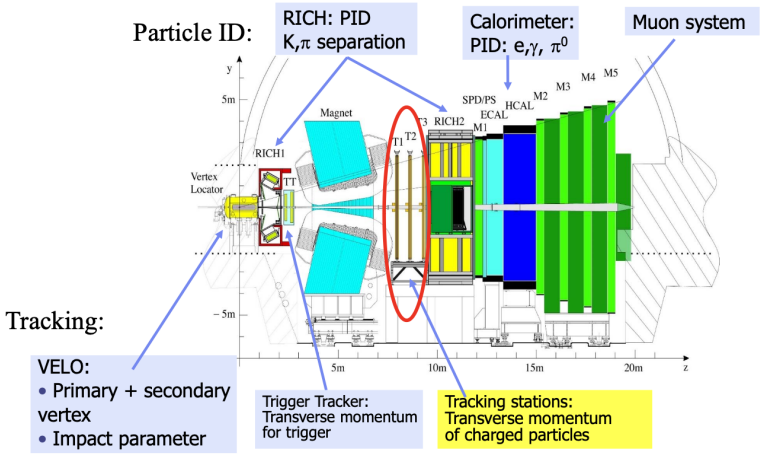

Outer Tracker

We know how a particle that traverses the gas can ionize atoms and get detected.

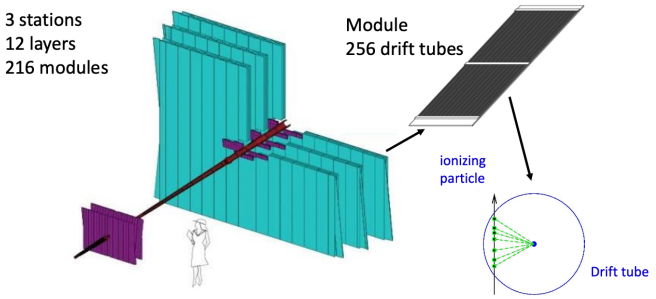

Specifications for the Outer Tracker

- There are 40 MHz collision rate:
  - Reference frequency
  - One event every 25ns
- 1.1 MHz readout rate
  - B hadron production rate c.a. 75 kHz
  - Radiation level for electronics 10 kRad
- Detector resolution
  - δp/p = 0.4% (20 GeV particle)
  - 200 μm in x
  - **1 ns drift time resolution**

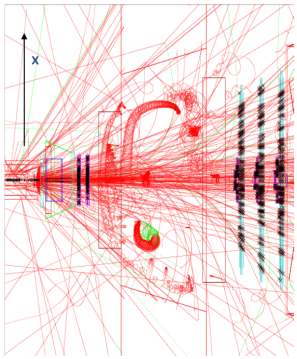

But from the electron on the drift tube to the actual signal, how do we do it?

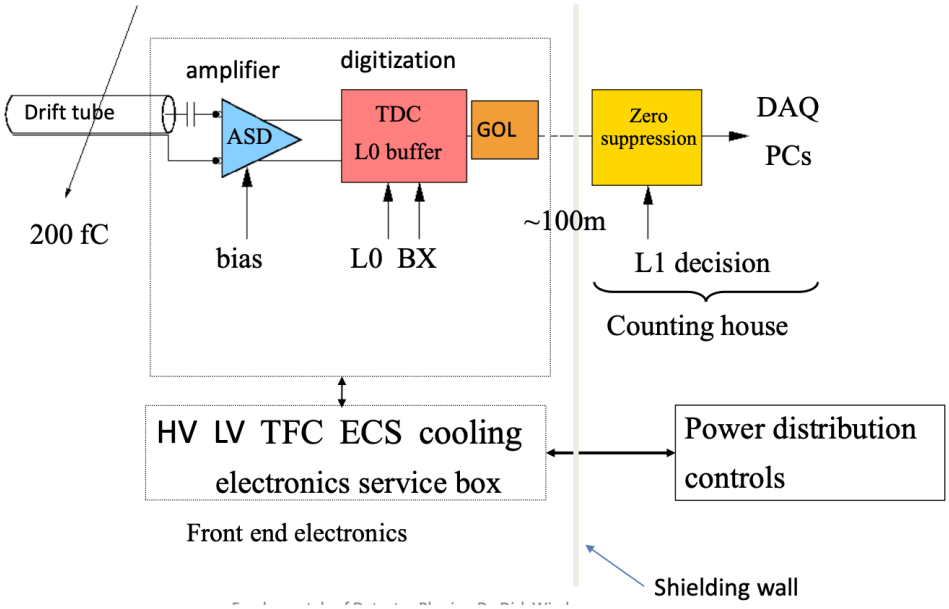

Amplifier

- Charge signal from detector
  - 40´000 electrons (6.4 fC)
- Signal is amplified
- Shaping:
  - 12 ns pulse (LHC bunch period is 25ns)
- 2 x 8 channels per amplifier card

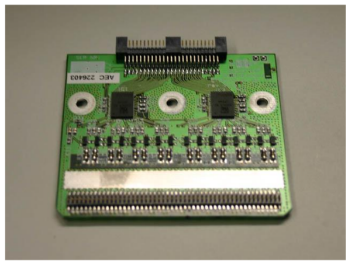

ASDBLR:
Amplifier **S**haper **D**iscriminator **B**ase **L**ine **R**estoration

Detector signal

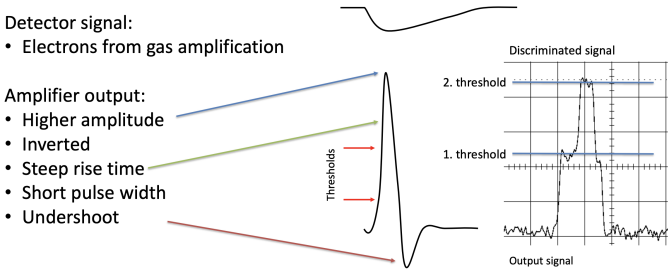

Digitizalition

The Time to Digital Converter (TDC) used in the LHCb experiment is used for measuring the time intervals between particle interactions. The TDC is primarily employed in the ring-imaging Cherenkov (RICH) detectors and the scintillator pad detectors.

The TDC is designed to convert the time difference between two events into a digital output.

It operates by measuring the time interval between the arrival of a particle at a reference point (e.g., the start of a detector) and its arrival at a detection point (e.g., the end of the detector). This time difference is then converted into a digital representation, typically in units of picoseconds or nanoseconds, depending on the precision required.

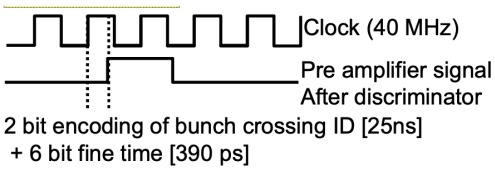

The specifications and features of a TDC system:

1. **32-channel TDC**: the system consists of 32 channels, meaning it can process timing information from up to 32 different input signals simultaneously.

2. **Fine time bin size: 25 ns/64 ≈ 390 ps:** This specifies the resolution or granularity of the TDC system. It indicates that each time bin, or division of time, corresponds to approximately 390 picoseconds (ps). This resolution defines the smallest time interval that can be measured by the TDC system.
3. **Time reference is LHC clock:** The timing information provided by the TDC system is synchronized with the clock signal of the Large Hadron Collider (LHC), which serves as the reference time for all measurements. Synchronization with the LHC clock ensures consistency and accuracy in timing measurements across different components of the experiment.
4. **Readout window: 75 ns:** This defines the duration of the time window during which the TDC system is actively collecting data. In this case, the readout window spans 75 nanoseconds (ns), indicating the period within which the TDC system captures timing information from incoming signals.
5. **Outer Tracker Time Information System (OTIS):** The Outer Tracker is a subdetector of the LHCb experiment, and the OTIS utilizes the TDC system to provide precise timing information related to particle interactions and trajectories within this detector.

TDC linearity

The TDC linearity time difference vs. drift time evaluates the accuracy of the TDC in measuring time differences relative to the expected drift times. Its linearity indicates that the TDC output consistently reflects the true time differences between events, regardless of the drift time variations.

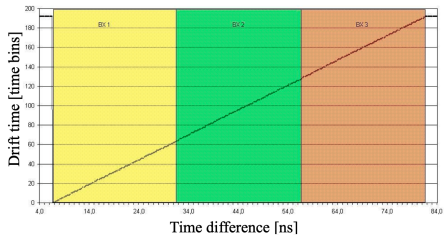

Drift time:

1. **Precisely Measured Drift Time:** Initially, the time taken by the charged particle to drift to the anode wire of the channel is accurately measured. This measurement is crucial for determining the position of the particle along the wire.
2. **Digitized Drift Time Sent to Computer:** The measured drift time is then converted into a digital format and transmitted to a computer for further analysis and processing. This digitization ensures that the drift time information can be efficiently handled and manipulated by computer algorithms.
3. **Calculation of Track Distance:** Using the digitized drift time information, the distance traveled by the charged particle from its origin to the anode wire of the channel is calculated. This distance measurement is essential for reconstructing the trajectory or path of the particle as it passes through the detection system.

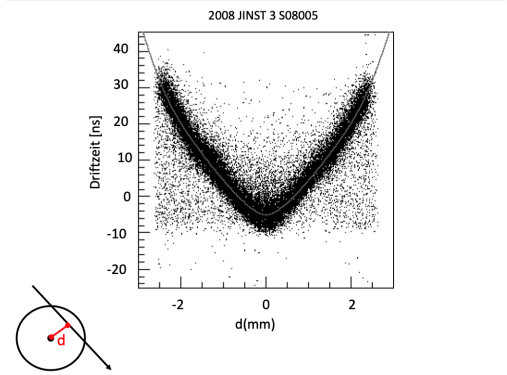

Gigabit Optical Link card - Detector electronic box - Optical receiver card - Data acquisition board

technische universität dortmund

Gigabit Optical Link card

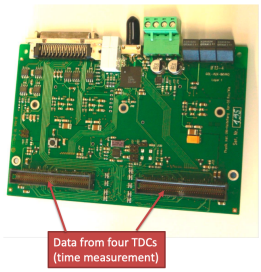

- Data of 4 x 32 detector channels
- 1.6 Gbit/s output
- 1 optical data fibre for 128 channels
- Fast and slow control
- Jitter filter (≤ 7ps RMS)
- Voltage regulators

23.04.2024 Fundamentals of Detector Physics, Dr. Dirk Wiedner 24

technische universität dortmund

Detector electronic box

Water cooling power: 20 W

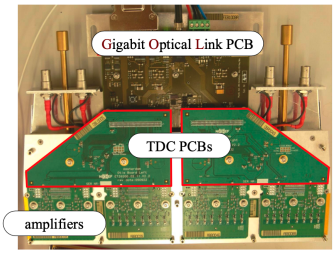

detector: 128 straw drift tubes

23.04.2024 Fundamentals of Detector Physics, Dr. Dirk Wiedner 25

technische universität dortmund

Optical receiver card

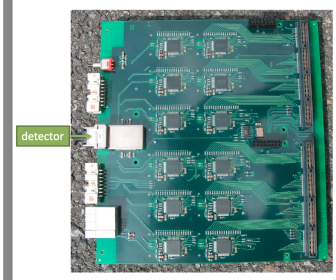

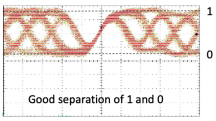

- Input mezzanine for data acquisition PCB (TELL1)
- 12 optical inputs
- 19,2 Gbit/s
- 288 parallel electrical outputs
- Bit error contribution $< 10^{-15}$

23.04.2024 Fundamentals of Detector Physics, Dr. Dirk Wiedner 26

technische universität dortmund

Data acquisition board

Detector

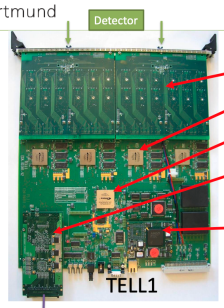

- Optical receiver card
- Processing FPGA
- SyncLink-FPGA: packet assembly
- Quad Gigabit Ethernet output to computing farm
- Credit Card PC: slow control via Ethernet

Computing farm

technische universität dortmund

Data acquisition board

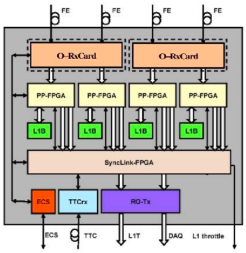

© Guido Haefeli

- Data from up to 24 half modules
- LHCb wide standard
- Tasks:
  - De-serialization
  - Synchronisation
  - Processing
  - Storage (60 ms = 65k events)
  - Ethernet output data for L1-trigger and event building

LT4

Particle Tracking

We want to identify particles.

Pattern recognition and track finding are essential steps in particle physics experiments. They involve identifying the trajectory of an individual particle within an ensemble of hits. Once the trajectory is recognized, **track reconstruction** comes into play. This step aims to find the best estimate for the particle's trajectory, enabling further analysis.

Track reconstruction facilitates the **measurement of the particle's momentum** by analyzing the bending radius within a magnetic field. This momentum measurement provides valuable information about the particle's properties and behavior.

After determining the trajectory and momentum, the next step is to extrapolate the track back to its origin. This process allows for the **reconstruction of the particle's primary or secondary vertex**, providing insights into the particle's interaction and decay processes.

However, throughout these processes, **estimating uncertainties** in the measured quantities is crucial. Factors such as detector layout and multiple scattering can influence the accuracy of the measurements. Hence, understanding and accounting for these uncertainties are essential for drawing meaningful conclusions from experimental data.

Example and *Nomenclature*:

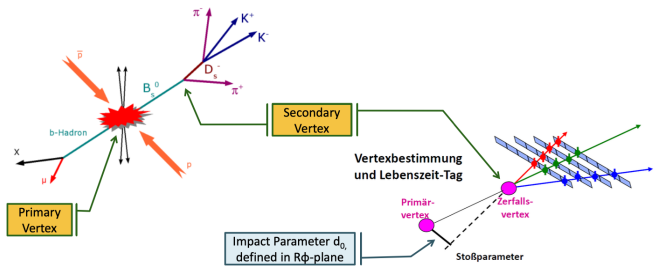

How to Parametrize a Track?

A particle without magnetic field will be a straight line

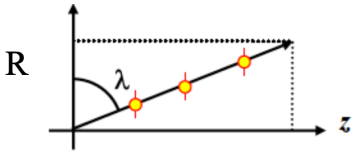

How to parametrize it? You can use, if the beam is the z direction, projecting particle track onto xz- and yz-plane

$$y = t_{xy} \cdot x + y_0$$
$$z = t_{zx} \cdot x + z_0$$

A straight line in space is given by four parameters, for example offset and slope for two orthogonal projections, taken here in the xy and xz planes.

If you do have a magnetic field that goes in the z direction, then the particle will travel following an helical line.

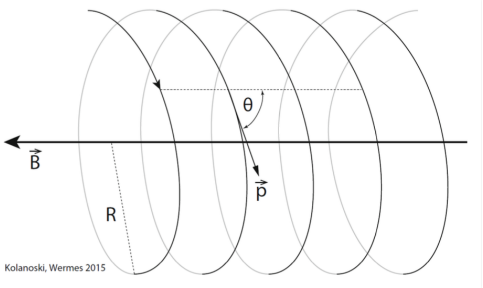

If the magnetic field is in the z direction

$$x = x_0 + R(cos(\psi_0 - \eta\psi) - cos(\psi_0))$$
$$y = y_0 + R(sin(\psi_0 - \eta\psi) - sin(\psi_0))$$
$$z = z_0 + \frac{\psi R}{tan(\theta)}$$

here $\eta = q/|q| = \pm 1$ is the sign of the charge.

The projection of the track length onto the xy plane is $s_{xy} = \psi R$. The direction of rotation is given by $\psi \geq 0$ and the sign of the charge, $\eta = q/|q|$. Positively charged particles rotate anticlockwise if viewed in the direction of the B field and negative particles rotate clockwise.

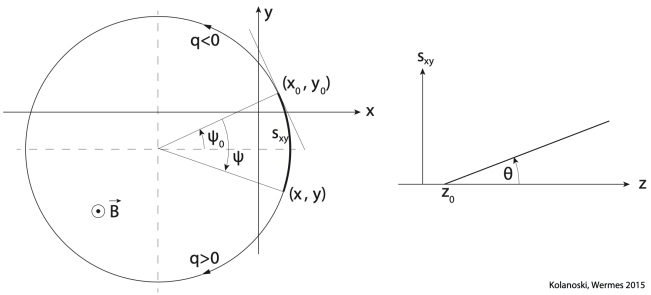

In the parametrization the point (x_0, y_0, z_0) is the starting point on the helix and the circle centre of the xy projection lies at $(x = x_0 - R\cos\psi_0, y = y_0 - R\sin\psi_0)$.

The helix has six parameters: the start coordinates x_0, y_0, z_0, the two angles ψ_0, θ and the curvature in the xy projection,

$$\kappa = -\eta/R \quad (\eta = q/|q| = \pm 1)$$

with the sign depending on the charge as given above.
The projection of the helix onto the plane perpendicular to the magnetic field describes a circle determined by the three parameters x_0, y_0 and R. The representation

$$y = y_0 + \sqrt{R^2 - (x - x_0)^2}$$

depends nonlinearly on the parameters x_0 and R. The expansion of the expression above for large radii R, corresponding to large momenta,

$$y = y_0 + R\left(1 - \frac{(x - x_0)^2}{2R^2} + \ldots\right) = \left(y_0 + R - \frac{x_0}{2R^2}\right) + \frac{x_0}{R}x - \frac{1}{2R}x^2 + \ldots$$

leads to a parabolic approximation of the trajectory which can be written as a linear function of three parameters:

$$y = a + bx + \frac{1}{2}cx^2 \approx a + bx$$

The new parameters a, b, c are functions of the parameters x_0, y_0, R corresponding to the first three coefficients in the expansion.

For very large R we have 2 parameters.

Track model

We now have a parametrised description of the trajectory. This is

- combination of straight lines and helices
- needs to take changes in momentum (energy loss, Bremsstrahlung) and direction, since it travel trough a detector. The particle scatter in the material and it do not loose energy but it changes direction (multiple Coulomb scattering).

All of that togheter is called a track model and we can say that more or less this model can have several parameter that it depends on. So we call the parameters $(\theta_1, \theta_2, \ldots, \theta_M)$ and we perform a fit using (usually) the lesat-squares-fit.

We can use the track model to extract **momentum** and **impact parameter**.

How does it looks in reality? *How we can build a detector?*

Forward spectrometers. The arrangement in figure below with a dipole magnet is typical for a fixed-target experiment. It is called a 'forward spectrometer' because the particles which are produced by a beam hitting a fixed target move preferentially into the forward direction within a narrow solid angle. Therefore the detectors are installed preferentially perpendicular to the beam direction (here the x-axis) and deliver measurement points y_i and z_i at fixed x_i. The interaction point can be exploited as a measurement point as well if it is sufficiently well localised.

In a homogeneous magnetic field the particle trajectories are *helices*, in front and behind the magnet they are *straight lines*.

The minimal number of measurements required for a full reconstruction are three points in the plane of momentum deflection and two points in the perpendicular plane.

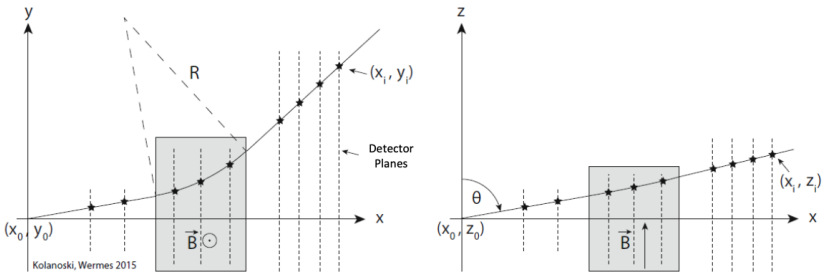

view of bending plane

view of non-bending plane

Typical layouts of (quasi) fixed-target experiments
- asymmetric detector
- dipol magnetic field along direction of travel of collision products

Examples: LHCb, Belle II

Solenoid spectrometers. The arrangement in fig. below with a solenoid magnet for momentum analysis is typical for a collider experiment where the beams usually cross in the centre of the solenoid. The beam size in the deflection plane xy is typically about $100\mu\mathrm{m}$ or less so that the centre of the beam cross section in the xy plane can often be considered as a measurement point. In general this beam constraint will not be required, however, in order to maintain the possibility to reconstruct tracks from decays which do not come from the primary vertex.

In many detector arrangements the tracks are measured inside the solenoid by cylindrical track detectors, the measurement coordinates being $(ri, zi, \varphi i)$. In cylindrical drift chambers or correspondingly arranged semiconductor detectors the detector cells lie on a cylinder surface with fixed radii r_i on which the azimuthal angle φ_i and possibly also z_i are measured.

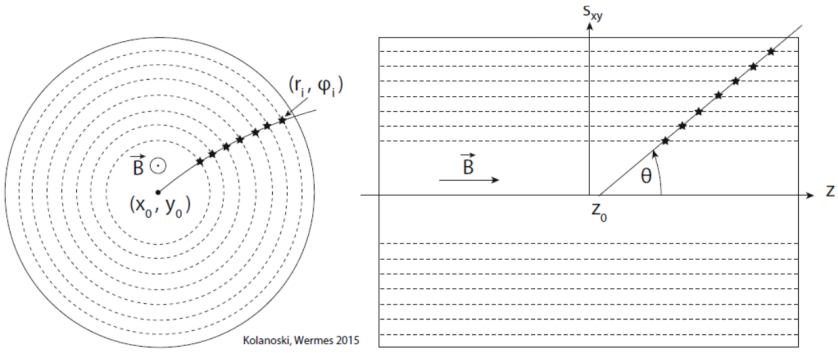

view along beam axis

side view

Typical layout of collider experiments:
- hermetic (4π) cylindrical detector
- solenoidal magnetic field

Examples: ATLAS, CMS, ALICE

Pattern Recognition

Which of the many hits belong to a track?

1. Check every possible combination of hits if they fit a track model: One might consider checking every possible combination of hits to see if they conform to a track model. However, this brute-force approach is highly inefficient due to the vast number of possible combinations.
2. To reduce combinatorial complexity, conditions can be applied to tracklet candidates:
   - tracklet points to interaction point
   - next step: combine into larger tracklets/tracks
   - algorithm has to be robust wrt
   - outliers (sometime the detector doesn't work properly)
   - missing hits (the de tector doesn't detect the track)
   - ambiguities

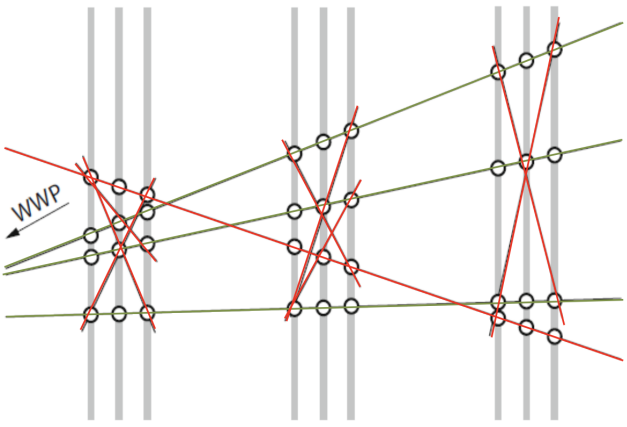

3. **Kalman-Filter algorithm**
   - starting from one hit predict hit position on the next plane (assuming a certain track model)
   - find predicted hit, use actual hit position to update prediction (scattering)
   - repeat until end of track is reached

-> pattern recognition and track reconstruction at the same time

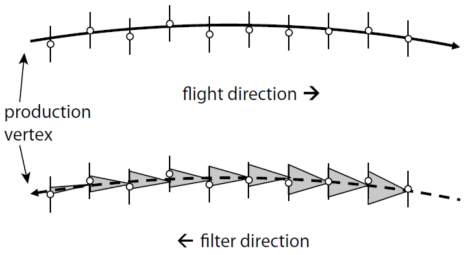

Those methods are local methods because they look at single hits. But there are several algorithms that looks at all the traks at once:

4. **Global methods:**
   neural nets, adaptive templates, etc.

Momentum: Forward Spectrometer

We consider a spectrometer but without the detectors inside the magnet, such that the particle trajectories are only measured in front and behind the magnet. In this case the momentum is determined by the change of the direction in front and behind the magnet.

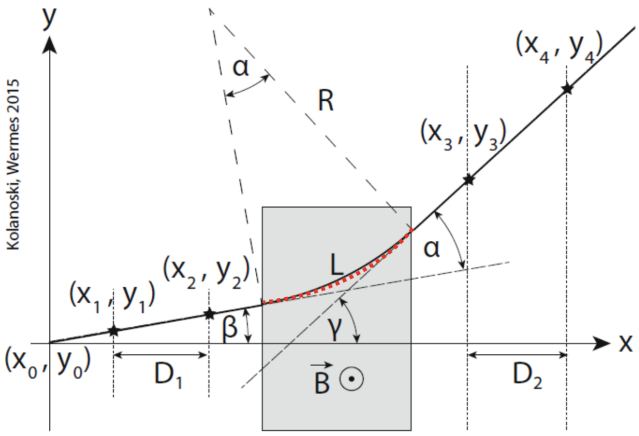

The deflection angle α can be obtained from the figure using the formula:

$$\alpha = \frac{L}{R} = \frac{q}{p_T} LB,$$

where L is the path length inside the magnet (we only consider the projection onto the plane perpendicular to the magnetic field).

The right-hand side of the formula follows from the R definition recovered form a magnetic field track:

$$R = \frac{p_T}{|q|B}$$

The bending power of the magnet is proportional to LB or in an inhomogeneous field proportional to the path integral over the momentum-deflecting field component:

$$\alpha = \int_L D dl$$

According to the figure the angle α is given by the difference of the slope angles of the line behind and before the magnet, $\alpha = \gamma - \beta$
Let the straight lines in front and behind the magnet both be determined by the minimal number of two measurement points.

The slope angles are then given by:

$$\tan\beta = \frac{y_2 - y_1}{x_2 - x_1} = \frac{y_2 - y_1}{D_1}, \quad \tan\gamma = \frac{y_4 - y_3}{x_4 - x_3} = \frac{y_4 - y_3}{D_2}.$$

Here $D_1 = x_2 - x_1$ and $D_2 = x_4 - x_3$ are the fixed distances of the measurement planes in which at fixed x coordinates the y coordinates are measured with the resolution σ_{meas} .

Under the assumption that σ_{meas} is the same for all measurements the errors of the slopes are

$$\sigma_{\tan\beta} = \sqrt{2}\frac{\sigma_{\text{meas}}}{D_1}, \quad \sigma_{\tan\gamma} = \sqrt{2}\frac{\sigma_{\text{meas}}}{D_2}.$$

In the approximation of small angles one obtains for the deflection angle α :

$$\alpha = \gamma - \beta \approx \frac{y_4 - y_3}{D_2} - \frac{y_2 - y_1}{D_1}.$$

The error of α follows from error propagation:

$$\sigma_\alpha = \sqrt{2}\sigma_{\text{meas}}\sqrt{\frac{1}{D_1^2} + \frac{1}{D_2^2}}$$

or for the same distances of the measurement planes $(D_1 = D_2 = D)$

$$\sigma_\alpha = \frac{2\sigma_{\text{meas}}}{D}.$$

Hence the resolution is proportional to the position resolution σ_{meas} of a measurement and inversely proportional to the lever $\text{arm}\, D$ over which the straight lines are measured. However, the resolution cannot be arbitrarily improved by enlarging D because there are always conditions constraining the size of the detector.

Momentum: Solenoid Spectrometer

We consider now the case where the curvature of a track is measured inside the magnetic field. The connection between the transverse momentum p_T and the curvature κ, as defined, is

$$p_T = |q|BR = \frac{|q|B}{|\kappa|}.$$

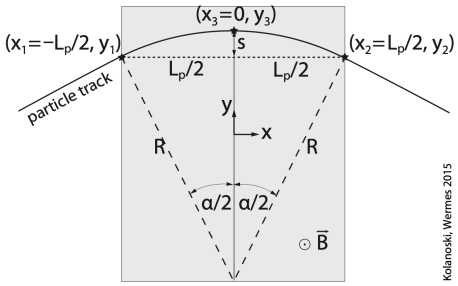

Fig. 9.12 Geometric relations for the deflection of a charged particle in a homogeneous magnetic field of length L_p. The drawing delineates the sagitta s of the circular arc in the magnetic field and the deflection angle α of the particle.

The measurement of a momentum in a homogeneous magnetic field boils down to the determination of the **sagitta**, that is, the largest perpendicular distance of the trajectory from the connecting line between the particle's entrance into and exit from the magnetic field volume. From the figure we obtain the following relations for the sagitta:

$$\frac{R-s}{R} = \cos\frac{\alpha}{2} \approx 1 - \frac{\alpha^2}{8} \quad \text{and} \quad \frac{L_p}{2R} = \sin\frac{\alpha}{2} \approx \frac{\alpha}{2}.$$

The approximations are valid for small deflection angles, respectively large momenta. This yields for the sagitta

$$s \approx \frac{R\alpha^2}{8} = \frac{1}{8}\frac{L_p^2}{R} = \frac{1}{8}L_p^2|\kappa|.$$

Hence the sagitta s is proportional to the curvature κ and therefore the error of the sagitta determination is also proportional to the error of the curvature from which the momentum is determined:

$$\sigma_\kappa = \frac{8}{L_p^2}\sigma_s$$

For the determination of a circular trajectory at least three measurement points are required which are optimally placed at the beginning, the end and in the centre of the magnetic field (the points are given by their coordinates in the deflection plane).

The three points may be measured by three detector planes positioned perpendicular to the mean direction of the particle trajectories (x direction) at $x = -L_p/2, 0, L_p/2$. The detectors deliver the y coordinates with errors σ_{meas}, assumed to be the same for all three points. From the measured points the sagitta is derived according to

$$s = y_3 - \frac{y_1+y_2}{2} \Rightarrow \sigma_s = \sqrt{\sigma_{\text{meas}}^2 + \frac{1}{4}2\sigma_{\text{meas}}^2} = \sqrt{\frac{3}{2}}\sigma_{\text{meas}}\,.$$

With the error of the curvature then follows as

$$\sigma_\kappa = \sqrt{\frac{3}{2}}\frac{8}{L_p^2}\sigma_{\text{meas}} = \frac{\sqrt{96}}{L_p^2}\sigma_{\text{meas}}\,.$$

The factor $\sqrt{96}$ is valid for $N = 3$ measurements. The general formula for N equally spaced measurements reads

$$\sigma_\kappa = \frac{\sigma_{\text{meas}}}{L_p^2}\sqrt{\frac{720(N-1)^3}{(N-2)N(N+1)(N+2)}}.$$

For many measurements $(N \gtrsim 10)$ one obtains

$$\sigma_\kappa \approx \frac{\sigma_{\text{meas}}}{L_p^2}\sqrt{\frac{720}{N+4}}$$

The resolution of the transverse momentum can be calculated by error propagation using the relation between transverse momentum and curvature in:

$$\sigma_{p_T} = \frac{p_T^2}{|q|B}\sigma_\kappa$$

When deriving the p_T resolution by Gaussian error propagation one has to keep in mind that the error of the transverse momentum is not normally distributed (even if the error of the curvature is), in particular at very large momenta (see also the corresponding discussion of the p_T dependence in the listing below). For N equally spaced points and in the limit of large N the resolution of the transverse momentum is then obtained

$$\left(\frac{\sigma_{p_T}}{p_T}\right)_{\text{meas}} = \frac{p_T}{0.3|z|}\frac{\sigma_{\text{meas}}}{L_p^2 B}\sqrt{\frac{720}{N+4}}$$

$$[p_T] = \text{GeV}/c, [L_p], [\sigma_{\text{meas}}] = \text{m}, [B] = \text{T}.$$

This relation, called the 'Gluckstern formula', describes the momentum resolution at high momenta where multiple scattering can be neglected.

How to optimize momentum resolution

The momentum resolution σ_{p_T} depends on the position resolution σ_{meas} of the points in the plane of momentum deflection, the number N of measurements and the length L_p of the track in the projection perpendicular to the magnetic field. The dependences of the equation on each of the parameters provide indications on how the momentum resolution can be optimised:

- $\propto \sigma_{\text{meas}}$: The position resolution of the detector should be optimised up to the point where other resolution contributions, for example multiple scattering, dominate. Other precision limitations come, for example, from mechanical tolerances and temperature dependences which can introduce larger uncertainties than the intrinsic detector precision, in particular in large detector arrangements.
- $\propto 1/L_p^2$: A large gain in momentum resolution comes from the length of the measured part of the track, that is, from the size of the detector.

However, the costs for a detector, for example at a collider, scale at least as strongly as L_p^2.

- $\propto 1/B$: For the same momentum a stronger magnetic field yields a larger curvature of the track leading to an improved resolution. However, too large curvatures hinder efficient pattern recognition, for example by curling low-energy tracks generating high hit density ('curlers').
- $\propto 1/\sqrt{N}$: A large number of measurements improves the resolution, but merely by the square root of the number of measurements. However, having many measurement points is also beneficial for pattern recognition and for measurements of the specific ionisation (dE/dx measurements).
- $\propto p_T$: For high momenta the tracks are less curved and eventually can no longer be distinguished from straight lines. Therefore the resolution function is not symmetric in p_T. However, the resolution function of the curvature, $|\kappa| = 1/R \propto 1/p_T$, is approximately normally distributed. In simulations, therefore, κ is usually generated according to a normal distribution and then converted into p_T. There nothing that we can do about it...

Error due to multiple scattering

Multiple scattering refers to the phenomenon where charged particles, such as electrons or protons, undergo numerous small-angle deflections as they pass through a medium

The mean sagitta $\langle s_{\text{plane}} \rangle$ due to multiple scattering is given by

$$\sigma_s = \langle s_{\text{plane}} \rangle = \frac{1}{4\sqrt{3}} L_p \frac{\theta_{ms}}{\sin\theta}.$$

we obtain

$$\sigma_\kappa = \frac{8}{L^2}\sigma_s = \sqrt{43}\frac{\theta_0}{L} = \frac{0.0136\,\text{GeV/c}}{p\beta L} z \sqrt{\frac{L/\sin\theta}{X_0}} \sqrt{1.33}$$

Multiple scattering increases momentum uncertainty:

$$\left(\frac{\sigma_{p_T}}{p_T}\right)_{\text{MCS}} = \frac{0.054}{LB\beta}\sqrt{\frac{L/\sin\theta}{X_0}}$$

The full transverse momentum resolution is obtained by quadratically adding the two different contributions:

$$\frac{\sigma_{p_T}}{p_T} = \sqrt{\left(\frac{\sigma_{p_T}}{p_T}\right)^2_{\text{meas}} + \left(\frac{\sigma_{p_T}}{p_T}\right)^2_{\text{scat}}} := \sqrt{(ap_T)^2 + b^2}.$$

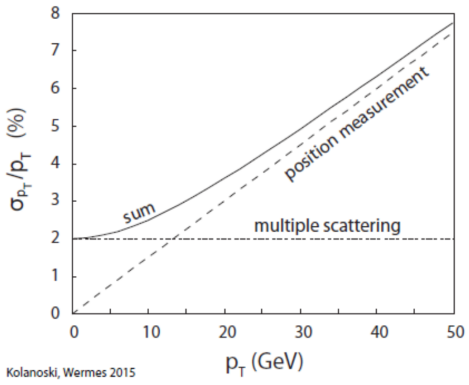

Example: Momentum Resolution in ATLAS

Rough estimate for original Inner Detector (Pixel + SCT + TRT)

- large p_T → neglect multiple scattering
- R_{min} = 5.05cm, R_{max} = 1082cm
- Pixel (5 - 12cm): N=3, σ=12μm
- SCT (30 - 55cm): N=4, σ=16μm
- TRT (55-105cm): N=36, σ=170μm
  → approximate as one measurement at : R=80cm, σ=28μm
- N = 3 +4 + 1 = 8
- <σ>~16μm

$$\Rightarrow \sigma_\kappa \approx \frac{\sigma_{\text{meas}}}{L^2} \times 7.56$$

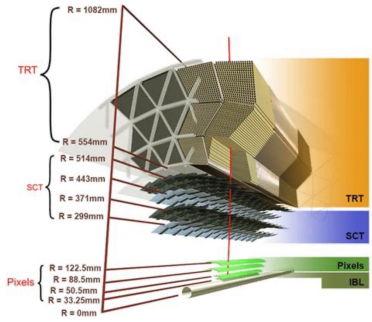

Why does momentum resolution depend on direction?
At $B = 2T$

$$\begin{aligned}\frac{\sigma_{p_T}}{p_T} &= \frac{\sigma_{\text{meas}}}{0.3BL^2} p_T \times 7.56 \\ &= 3.6 \times 10^{-4} p_T \quad \text{in GeV/c}\end{aligned}$$

At $p_T = 500\text{GeV/c} \quad \Rightarrow \frac{\sigma_p}{p} = 18\%$

Now look at this graph:

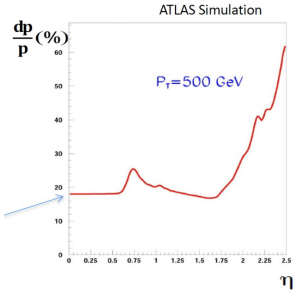

Why does momentum resolution depend on direction?

In the ATLAS detector the amount of material, often characterised by the radiation length, can vary with the pseudorapidity (η) of the particle trajectory.

The radiation length is a characteristic length scale that describes the mean distance over which a high-energy electron or photon loses a significant fraction of its energy through bremsstrahlung or photonuclear interactions. It

is a measure of the density of material in terms of its ability to interact with electromagnetic radiation.

In the ATLAS detector, regions of higher pseudorapidity (e.g., at η ≈ ±3) correspond to larger distances from the beam axis and thus may intersect more detector material. This can lead to a longer effective radiation length for particles traversing those regions compared to particles traveling closer to the beam axis.

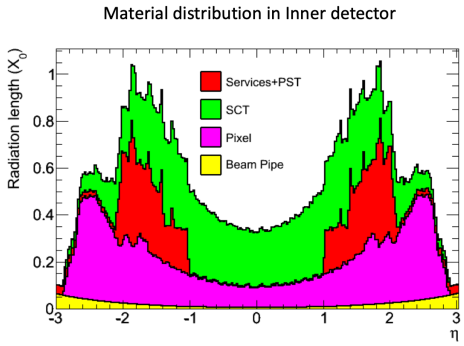

$\eta = -\ln \tan \theta/2$

Impact Parameter Resolution:

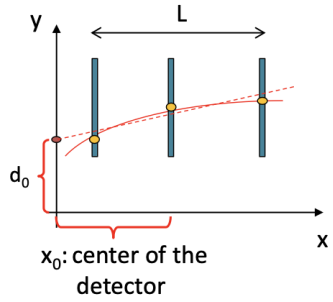

Use track model to extrapolate track towards vertex
Simplest case: Straight line $y = a + bx$

$$\Rightarrow \sigma_{d_0} = \sigma_y|_{x_0} = \sqrt{\sigma_a^2 + x_0^2 \sigma_b^2} = \frac{\sigma_{\text{meas}}}{\sqrt{N}} \sqrt{1 + \frac{12(N-1)}{(N+1)} r^2}$$

where $r := \frac{x_0}{L}$

Impact of multiple scattering:

$$\sigma_{d_0}^{\text{MS}} = \theta_{\text{MS}} \cdot r_B$$

$$\sigma_{d_0} = \frac{\sigma_{\text{meas}}}{\sqrt{N}} \sqrt{1 + \frac{12(N-1)}{(N+1)} r^2} \oplus \theta_0 r_B$$

→ high spatial resolution σ_{meas}
→ long lever arm L
→ first hit as close to vertex as possible
→ (large number of points along the track)

Even for an optimal geometry the impact parameter resolution will not significantly exceed the spatial resolution of individual hits.

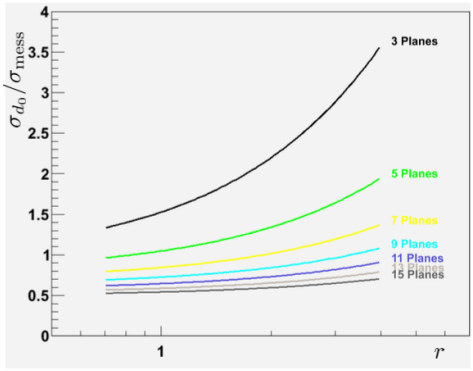

Example: ATLAS Pixel Detector

Original 3-layer Pixel Detector:
- N=3, σ=10µm
- x_1=5.05cm, x_2=8.85cm, x_3=12.25cm
- L=7.3cm, r=x_2/L=1.22

$$\Rightarrow \sqrt{1+\frac{12(N-1)}{(N+1)}r^2} = 3.15$$

Straight-line track model yields:

$$\sigma_{d_0} = 18.2\,\mu\text{m}$$

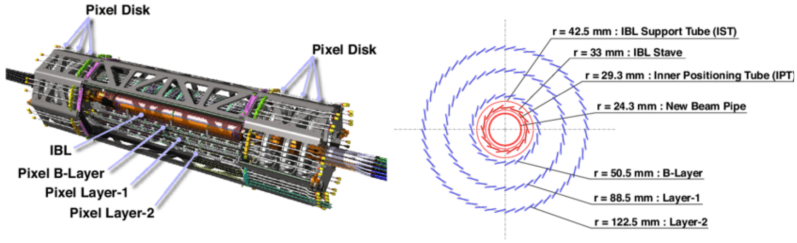

With IBL (N=4, x_0 = 3.55 cm)

$$\sigma_{d_0} = 12.5\,\mu\text{m}$$

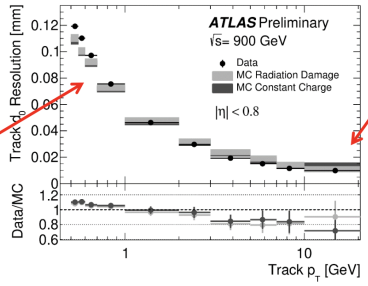

Large curvature for low momentum
→ straight-line approximation not valid
→ resolution becomes worse

σ_{d0}~10µm

Did not take multiple scattering component into account. It is often the dominant one…

Spatial Resolution of Small Electrodes

Binary readout (hit/no hit) or very narrow charge cloud

-> hit in only one channel (pixel/strip)

Typically set hit position = geometric centre of the electrode

But: Where was the hit really?

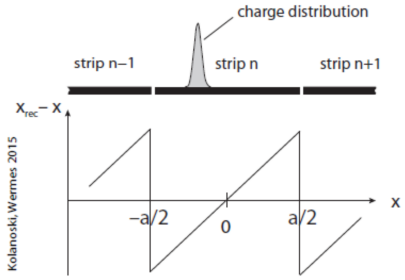

Assumptions:

- pitch, i.e. spatial frequency (channel distance middle-middle) is a
- channel registers the hit if charge deposited in interval (-a/2, a/2)

• hit probability constant across channel

Standard deviation of a uniform distribution in [-a/2, a/2]: $\sigma_x = \frac{a}{\sqrt{12}}$

If multiple channels are hit (cluster), and information about signal amplitude available
-> use centre of gravity of charge distribution as estimator for real hit position

Centre-of-gravity (COG) Method: $x_C = \frac{\sum S_i x_i}{S_i}$

Gaussian charge cloud of width σ

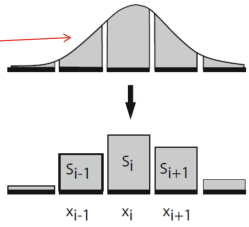

Can we use extended clusters to improve spatial resolution?

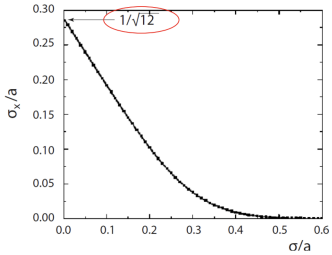

Highest spatial resolution σ_x (w/o noise) using c.o.g. for gaussian charge cloud (width σ) and electrode pitch a if

$$\frac{\sigma}{a} \geq \frac{1}{2}$$

0:00 / 1:33:34

LT5

Particle Identification

Characteristic Shape of the Signal in the Detector

Modern particle detectors consist of multiple sub-detectors that each play a role in identifying particles. These include **tracking systems** that detect the paths of charged particles, **electromagnetic and hadronic calorimeters** that measure energy deposition from particle interactions, and **muon systems** designed specifically to identify muons, which can penetrate other materials that stop most particles.

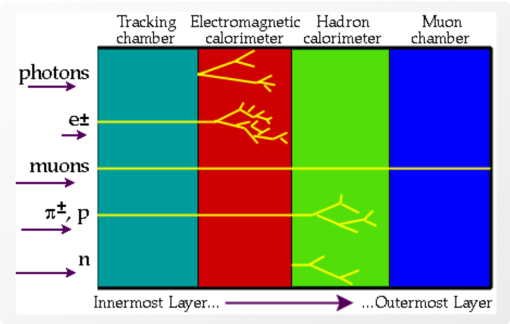

In practice, the signals produced by particles as they interact with these detectors are characteristic and can be used for identification.
Electrons and photons, for instance, produce electromagnetic showers in the electromagnetic calorimeter. Hadrons, on the other hand, are identified by the showers they create in the hadronic calorimeter, distinguished by deeper penetration and different interaction profiles compared to electromagnetic showers.
Muons are typically identified because they can pass through much of the detector material without being stopped, unlike most other particles.
This is a slice of the CMS detector and we can use the knowleedge gained before to identify particles:

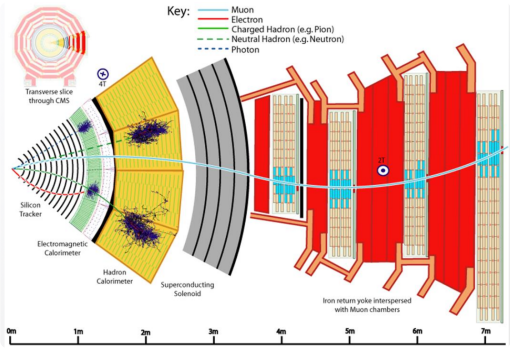

B-vertex determination

B-vertex determination is a critical technique used in particle physics to measure the properties of particles that decay via weak interactions. By analyzing the decay vertices —the points where particles decay— physicists can gain insights into the lifetimes and other properties of these particles. This

technique utilizes a Vertex Locator (**Velo**) in LHCb, which is a highly precise silicon detector positioned close to the particle collision point.

For instance, the Velo can be as close as $8mm$ from the LHC beam with a spatial resolution of about $5um$, achieving an impact parameter resolution of approximately $30um$.

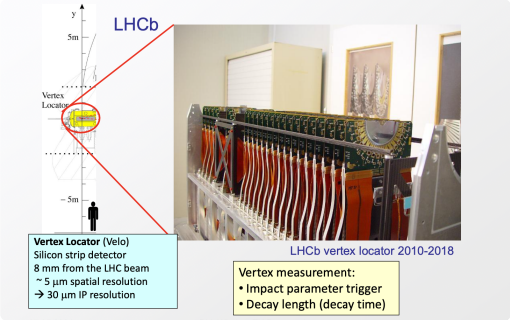

Through B-vertex determination, subtle differences in decay paths and times can be quantified, offering vital clues about the underlying processes involving particles like B_s and D_s mesons, critical for testing the Standard Model of particle physics.

An example: $B_s \to D_s K$

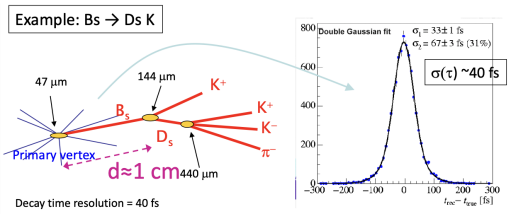

Reminder: ENERGY LOSS BY IONIZATION

The optical properties of a medium, crucial for understanding how particles interact with that medium, are characterized by the complex dielectric constant ϵ
This constant is a measure of a *material's ability to polarize in response to an electric field*, affecting how light and other electromagnetic radiation pass through it.

1. Refractive Index (n): Represented as \text{Re} \sqrt{\epsilon} , the refractive index is fundamental in determining how much light bends, or refracts, as it enters the medium. It dictates the phase velocity of light in the material relative to the vacuum.
2. Absorption Parameter (k): Given by \text{Im} \epsilon , this parameter indicates how much light is absorbed by the medium per unit distance. It directly affects the attenuation of light as it travels through the material.

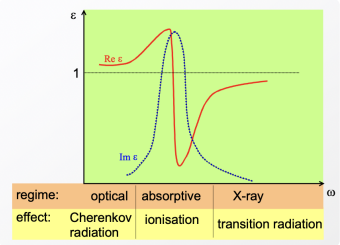

The graph distinctly marks different interaction regimes and their corresponding effects on charged particles:

Optical Regime:
- Effect: Cherenkov Radiation
- Occurs when charged particles travel faster than the speed of light in that particular medium, causing them to emit a glow, known as Cherenkov radiation. This phenomenon is used in detectors like Cherenkov detectors to identify particles.

Absorptive Regime:
- Effect: Ionization
- In this regime, charged particles lose energy primarily through ionization, where they knock electrons out of atoms, creating ions. This process is critical for understanding how particles lose energy as they pass through a detector.

X-ray Regime:
- Effect: Transition Radiation
- Transition radiation occurs when charged particles pass through the boundary between two materials with different dielectric properties. This type of radiation is especially useful for identifying high-energy particles that might not interact strongly with other materials.

Instead of ionizing an atom or exciting the matter, under certain conditions the photon can also escape from the medium:

- Emission of **Cherenkov** or **Transition** radiation (see later).
- The photon emission contributes to energy loss

Interaction of charged particles

The average differential energy loss $\frac{dE}{dx}$ is a crucial concept in understanding how charged particles lose energy as they travel through a medium. This energy loss is primarily due to interactions with electrons in the medium and is described by the Bethe-Bloch formula.

Energy Loss in a Single Encounter

When a charged particle passes near another electron in the medium, it exerts a force and causes the medium's electron to move, thereby transferring energy.

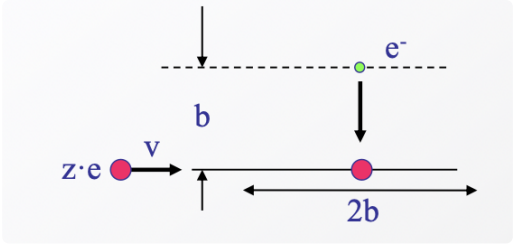

The force F_c experienced by the electron due to the passing charged particle can be described by the following equation:

$$F_c = \frac{ze^2}{b^2}$$

where:

- (z) is the charge number of the incoming particle,
- (e) is the elementary charge,
- (b) is the impact parameter (the perpendicular distance between the paths of the incoming particle and the electron).

Given the time ($\Delta t = \frac{2b}{v}$) it takes for the particle to travel past the electron, the change in momentum (Δp_e) of the electron can be calculated as:

$$\Delta p_e = F_c \Delta t = \frac{ze^2}{b^2} \cdot \frac{2b}{v} = \frac{2ze^2}{bv}$$

The energy transferred to the electron (ΔE_e) can be expressed as:

$$\Delta E_e = \frac{(\Delta p_e)^2}{2m_e} = \frac{(2ze^2)^2}{2m_e b^2 v^2}$$

usoing ht edefinitjion of the classical electron angle and the definition of the β we have

$$\Delta E_e = \frac{(\Delta p_e)^2}{2m_e} = \frac{(2ze^2)^2}{2m_e b^2 v^2} = \frac{2r_e^2 m_e c^2 z^2}{b^2} \cdot \frac{1}{\beta^2}$$

with $r_e = e^2/m_e c^2$

This was fo one single electron, but how many electrons are there?

The number of such encounters (N_e) a charged particle has as it passes through the medium is proportional to the electron density (N of the medium:

$$N_e \propto \frac{Z}{A} N \rho$$

where:

- Z is the atomic number of the medium,
- A is the atomic mass,
- ρ is the density.

Putting togheter all this claculation we recover at least one part of the bethe block formula:

$$\left\langle \frac{dE}{dx} \right\rangle = -4\pi N_A r_e^2 m_e c^2 z^2 \frac{Z}{A}\frac{1}{\beta^2}\left[\frac{1}{2}\ln\frac{2m_e c^2\gamma^2\beta^2 T^{\max}}{I^2} - \beta^2 - \frac{\delta}{2}\right]$$

where:

- (N) is Avogadro's number,
- (r_e) is the classical electron radius,
- (m_e) is the electron mass,
- (c) is the speed of light,
- ($\beta = v/c$),
- (γ) is the Lorentz factor,
- (I) is the mean excitation potential,
- (δ) is the density effect correction.

Graphical Representation of dE/dx

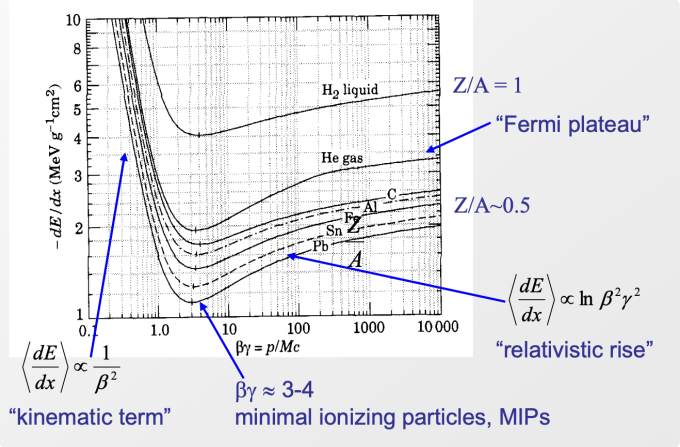

The graph provided in the slide shows ($\frac{dE}{dx}$) as a function of particle speed in terms of ($\beta\gamma$) for various materials. It highlights key features such as:

- **Fermi Plateau:** Where $\frac{dE}{dx}$ reaches a minimum and becomes relatively constant, reflecting the saturation of energy loss in highly ionized mediums.
- **Relativistic Rise:** As ($\beta\gamma$) increases beyond 3-4, ($\frac{dE}{dx}$) increases again due to the relativistic effects, indicating higher energy losses for very fast particles.
- **Minimal Ionizing Particles (MIPs):** Particles in this regime have the minimal interaction with the medium, which is crucial for detecting particles in particle physics experiments.

Other terms of the formula

Bethe - Bloch formula $\left\langle \frac{dE}{dx} \right\rangle = -4\pi N_A r_e^2 m_e c^2 z^2 \frac{Z}{A}\frac{1}{\beta^2}\left[\frac{1}{2}\ln\frac{2m_e c^2\gamma^2\beta^2 T^{max}}{I^2} - \beta^2 - \frac{\delta}{2}\right]$

relativistic rise - $\ln\gamma^2$ term – attributed to relativistic expansion of transverse E-field contributions from more distant collisions.

relativistic rise cancelled at high g by "density effect", polarization of medium screens more distant atoms. Parameterized by δ (material dependent) Fermi plateau

Particle identification using dE/dx measurements

• **Measurement of Energy Loss:** dE/dx is utilized to identify particles based on their energy loss profiles. Each type of particle (electron, muon, pion, kaon, proton, deuteron) has a characteristic energy loss pattern which can be observed and measured.

• **Calibration:** Accurate dE/dx measurement requires calibration to account for variations in detector response and to ensure precise energy loss measurement across different types of particles.

• **Momentum Measurement:** In addition to energy loss, the momentum of the particle is also measured. This is necessary because dE/dx varies with the velocity of the particle, which in turn depends on its momentum.

TPC measurement

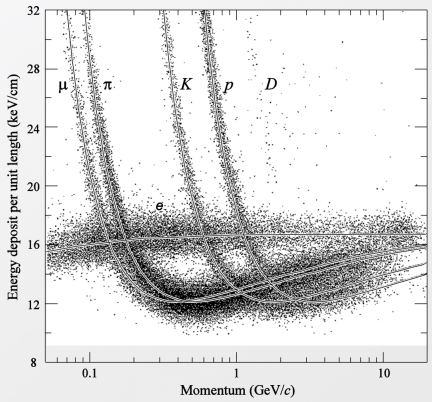

• **Electrons (e):** Typically lose more energy at lower momenta and follow a distinct curve due to their low mass.

• **Muons (μ), Pions (π), Kaons (K), Protons (p),** and **Deuterons (D):** Each type of particle shows a unique dE/dx curve which allows them to be distinguished from one another in the momentum range of approximately 0.1 to 10 GeV/c.

Other interactions with charged particles

Besides ionization there are further types of energy loss!

-> Emission of real photons through processes like elastic scattering and the conservation of energy and momentum.

A photon in a medium follows a *dispersion relation*, which relates the frequency ω of the photon to its wavelength λ, the speed of light (c), and the refractive index (n) of the medium:

$$\omega = 2\pi f = 2\pi \frac{c/n}{\lambda} = k\frac{c}{n} \qquad \omega^2 - \frac{k^2c^2}{\varepsilon} = 0 \qquad \varepsilon = n^2$$

Here, $\epsilon = n^2$ represents the squared refractive index which characterizes the optical properties of the medium. This equation simplifies the relationship between a photon's frequency and its propagation characteristics within different media.

Emission of Real Photons

Real photons can be emitted through elastic scattering involving energy and momentum conservation. The equation:

$$\omega \approx \vec{v} \cdot \vec{k} = vk\cos\theta$$

describes how the frequency of the photon (ω) relates to the velocity (v) of the particle, the wave number (k) of the photon, and the angle (θ) between the particle's velocity vector and the direction of the emitted photon.

The angle (θ) of photon emission, considering the speed of the particle and the speed of light in the medium, is given by:

$$\cos\theta = \frac{\omega}{vk} = \frac{kc}{nvk} = \frac{1}{n\beta}$$

where $\beta = v/c$ is the particle's velocity relative to the speed of light in vacuum.

Cherenkov radiation

A light cone, so called Cherenkov radiation is emitted

- When charged particles pass through matter
- With a velocity v exceeding the velocity of light in the medium
- Measure angle of light cone → v of particle; Particle ID possible

Conditions for Photon Emission:

- The particle's velocity (v) must satisfy (v \beta c) being higher than the speed of light in the medium (c/n).
- The angle (\theta) where (\beta = 1/(n \cos \theta)) must be such that (\beta \geq 1/n).

This leads to the condition that a particle emits real photons in a dielectric medium if its velocity exceeds the phase velocity of light in that medium, resulting in Cherenkov radiation.

This is a critical effect used in various particle detectors to identify particles and measure their properties based on the light they emit while

traveling through a medium.

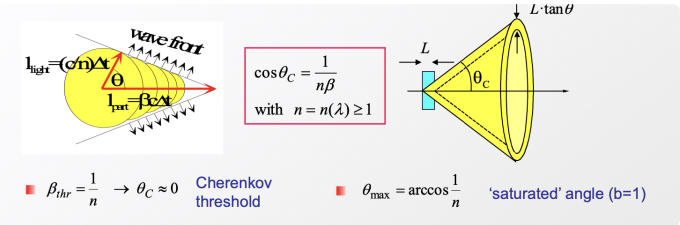

Number of emitted photons per unit length and unit wavelength interval

$$\frac{d^2N}{dxd\lambda} = \frac{2\pi z^2\alpha}{\lambda^2}\left(1-\frac{1}{\beta^2n^2}\right) = \frac{2\pi z^2\alpha}{\lambda^2}\sin^2\theta_C$$

$$\frac{d^2N}{dxd\lambda} \propto \frac{1}{\lambda^2} \quad \text{with } \lambda = \frac{c}{v} = \frac{hc}{E}\frac{d^2N}{dxdE} = \text{const.}$$

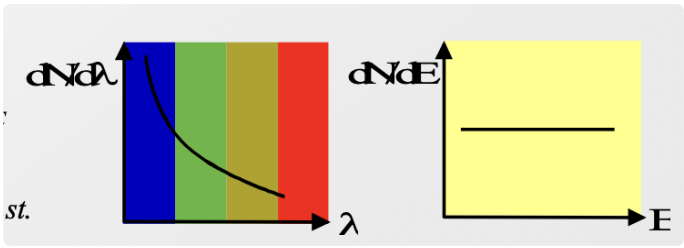

Example: Estimate the energy loss by Cherenkov radiation in quartz

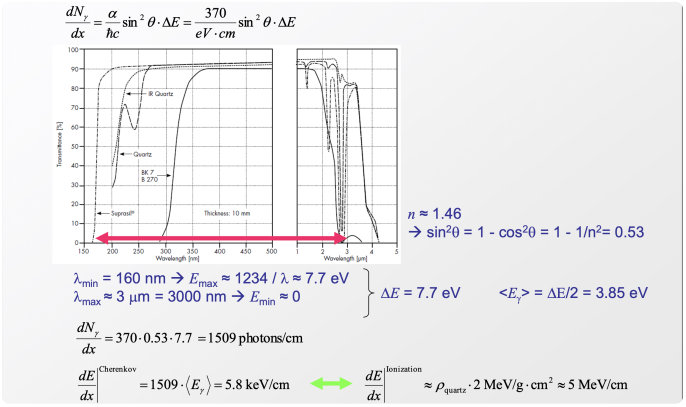

Cherenkov detectors

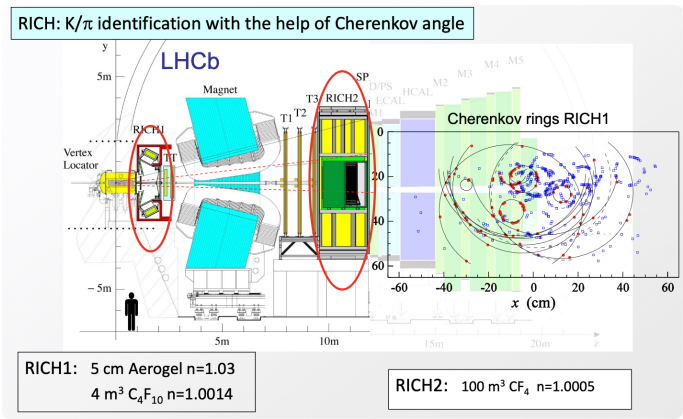

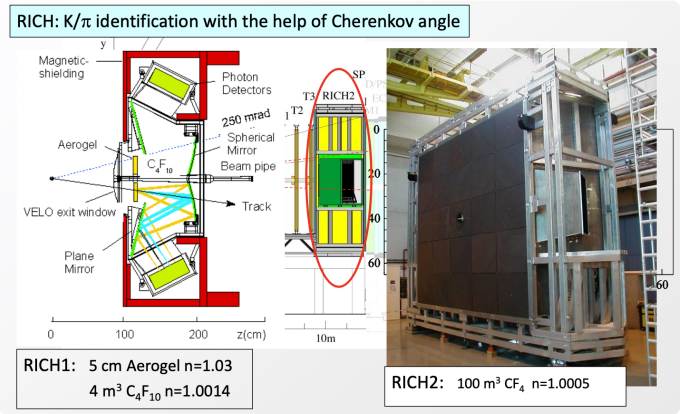

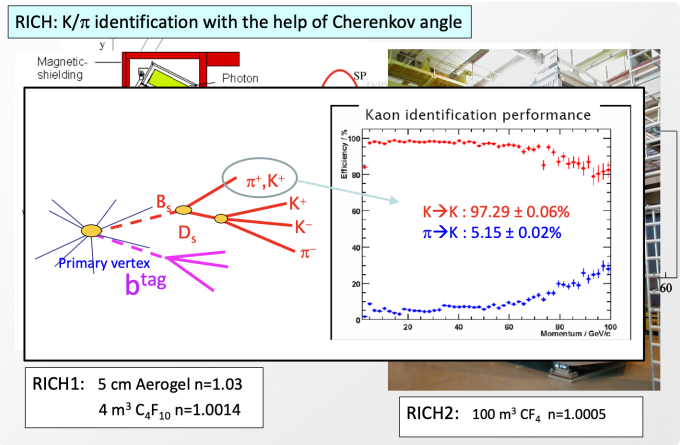

Time of flight measurement

Basic idea:
Measure signal time difference between two detectors with good time resolution
[start and stop counter; also: beam-timing & stop counter]

Typical detectors:
Scintillation counter Resistive Plate Chamber (RPC)

Coincidence setup or TDC measurement with common start/stop from interaction time

Time of flight measurement
Distinguishing particles with ToF:

Particle 1 : velocity v_1, β_1; mass m_1, energy E_1
Particle 2 : velocity v_2, β_2; mass m_2, energy E_2
(particles have same momentum p)
Distance L : distance between ToF counters

$$\Delta t = L\left(\frac{1}{v_1} - \frac{1}{v_2}\right) = \frac{L}{c}\left(\frac{1}{\beta_1} - \frac{1}{\beta_2}\right) \quad \text{Distance } L: \text{distance}$$
$$= \frac{L}{pc^2}(E_1 - E_2) = \frac{L}{pc^2}\left(\sqrt{p^2c^2 + m_1^2c^4} - \sqrt{p^2c^2 + m_2^2c^4}\right)$$

Relativistic particles, $E \simeq pc \gg m_i c^2$:

$$\Delta t \approx \frac{L}{pc^2}\left[\left(pc + \frac{m_1^2 c^4}{2pc}\right) - \left(pc + \frac{m_2^2 c^4}{2pc}\right)\right]$$
$$\Delta t = \frac{Lc}{2p^2}\left(m_1^2 - m_2^2\right)$$

Example:

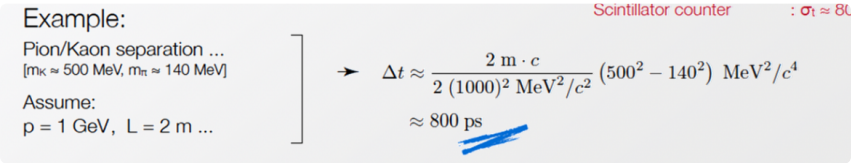

For mass resolution
Use:

$$\beta = L/\tau$$
$$\gamma = \left(1-\beta^2\right)^{-1}$$
$$c = 1$$

and knowing $* = \frac{p^2\tau^2}{L^2} = m^2 + p^2 = E^2$

Then

$$p = \beta\gamma m$$
$$m^2 = p^2\left(\frac{1}{\beta^2} - 1\right) = p^2\left(\frac{\tau^2}{L^2} - 1\right)$$
$$\rightarrow \delta\left(m^2\right) = 2p\delta p\underbrace{\left(\frac{\tau^2}{L^2} - 1\right)}_{m^2/p^2} + \underbrace{2\tau\delta\tau\frac{p^2}{L^2} - 2\frac{\delta L}{L^3}p^2\tau^2}_{\text{use } *}$$
$$= 2m^2\frac{\delta p}{p} + 2E^2\frac{\delta\tau}{\tau} - 2E^2\frac{\delta L}{L}$$

We obtain

$$\rightarrow \sigma\left(m^2\right) = 2\left[m^4\left(\frac{\sigma_p}{p}\right)^2 + E^4\left(\frac{\sigma_\tau}{\tau}\right)^2 + E^4\left(\frac{\sigma_L}{L}\right)^2\right]^{1/2}$$

Usually:

$$\left[\frac{\delta L}{L} \ll \frac{\delta p}{p} \ll \frac{\delta\tau}{\tau}\right] \quad \rightarrow \quad \sigma\left(m^2\right) = 2E^2\frac{\sigma_\tau}{\tau}$$

Uncertainty in time measurement dominates.

Transition radiation

Transition Radiation was first predicted by Ginzburg and Franck in 1946 and is often referred to as "sub-threshold Cherenkov radiation" because it occurs under conditions where Cherenkov radiation does not typically happen, due to the particle's speed being below the threshold for Cherenkov radiation in a given medium.

- **Medium Polarization:** As a charged particle (such as an electron) traverses the boundary between different media, it causes a temporary displacement of the electron density in the medium, leading to the formation of a dipole. This dipole varies over time as the particle passes through, emitting radiation known as Transition Radiation.
- **Radiated Energy Calculation:**
  - The formula for radiated energy per medium/vacuum boundary is given by:

$$W = \frac{1}{3}\alpha\omega_p\gamma$$

  - Here, (\alpha) is the fine-structure constant, (ω_p) is the plasma frequency of the medium, and (γ) is the Lorentz factor of the particle.
  - The plasma frequency ω_p can be expressed as:

$$\omega_p = \sqrt{\frac{N_e e^2}{\epsilon_0 m_e}}$$

    where (N_e) is the electron density, (e) is the elementary charge, (\epsilon_0) is the vacuum permittivity, and (m_e) is the electron mass.

Characteristics:

- **Directionality:** Due to the Lorentz transformation, the radiation is highly forward-peaked, meaning that the emitted photons stay very close to the particle track, making it easier to correlate detected photons with the passing particle.
- **Energy and Intensity:**
  - Typical photon energy for TR is about 20 eV for plastic radiators, which can go up to about 10 keV for x-rays, depending on the particle's energy and the medium.
  - The number of photons N_{ph} per boundary that can be emitted is approximately proportional to:

$$N_{ph} \approx \frac{W}{\hbar\omega} \approx \frac{1}{137}$$

    reflecting the dependence on the fine-structure constant.

Transition Radiation is particularly useful in particle identification for high-energy particles. Only particles like high-energy electrons have sufficient energy and Lorentz factor to emit Transition Radiation of detectable intensity. This property makes TR detectors valuable in experiments where distinguishing between different types of high-energy particles is crucial, such as in collider experiments or cosmic ray studies.

Detector Design

- Transition Radiation detectors are designed to have many boundaries (e.g., layers of different materials) to maximize the probability of detecting

radiation and thus enhance the sensitivity and resolution of the detector.

0:00 / 1:26:25

LT6

Gaseous detectors 1

Gaseous Detectors Overview:

- **Ionization, Drift, and Avalanche:** Incident radiation ionizes gas molecules, producing electron-ion pairs. Electric fields cause electrons to drift, and in some detectors, they undergo multiplication (avalanche).
- **Choice of Gas:** Depends on operating conditions, particle types, and application. Common gases include argon, xenon, and helium.
- **Operation Modes:** Proportional, avalanche, and drift modes offer different trade-offs in sensitivity, resolution, and dynamic range.
- **p-Measurement:** Precision measurement of particle positions within the detector, crucial for trajectory reconstruction.
- **B x E Effects:** Magnetic fields cause charged particle bending; electric fields affect electron drift and avalanche processes.

Detector Types:

1. **MWPC:** Parallel wire chambers for tracking charged particles.
2. **Drift Chambers:** Measure electron drift time for spatial resolution.
3. **TPC:** Time Projection Chambers enable 3D track reconstruction.
4. **RPC:** Resistive Plate Chambers for fast response in high-rate environments.
5. **MPGD:** Micro-Pattern Gaseous Detectors, like GEMs and Micromegas, offer high resolution and operate in high-rate conditions.

Ionization of Gases

Fast charged particles ionize atoms of gas. Often, the resulting primary electrons will have enough kinetic energy to *ionize other atoms*.

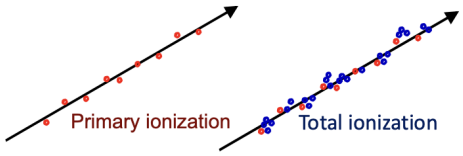

$$n_{\text{total}} = \frac{\Delta E}{W_i} = \frac{\frac{dE}{dx}\Delta x}{W_i}$$

    n_{\text{total}} \approx 3 \ldots 4 \cdot n_{\text{primary}}

n_{total}- number of created electron-ion pairs
DE = total energy loss
Wi = effective energy loss/pair

How to read the signal?

Cluster counting with a hybrid gas detector: pixel readout chip + micromegas foil.

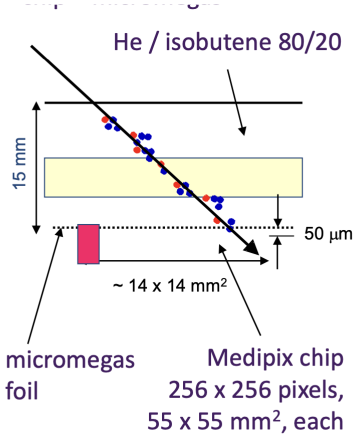

We have a chip in the bottom part that record the free charge due to ionization.

Example: track by cosmic particle (mip): 0.52 clusters / mm, ~3 e-/cluster

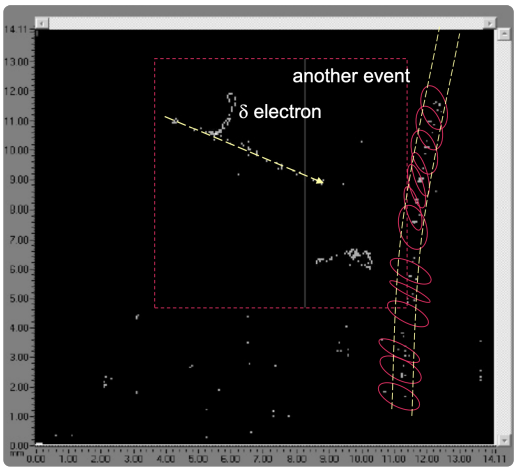

- the delta electron is an electron that get kicked out from an atom if a particle has huge momentum.

Mathematical description: Ionization of Gases

The actual number of primary electron/ion pairs produced is Poisson distributed:

$$P(m) = \frac{\mu^m e^{-\mu}}{m!}$$

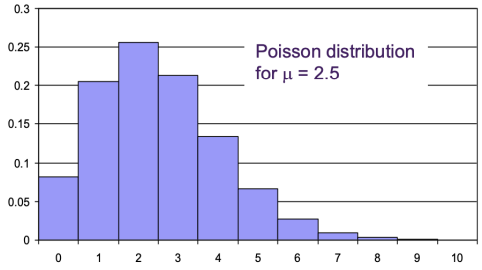

We actually have a probability of detecting 0 particles that is not a good thing, but as we can see from the graph is different from 0.

The detection efficiency is therefore limited to :

$$\varepsilon_{\text{det}} = 1 - P(0) = 1 - e^{-\mu}$$

For thin layers e_{det} can be significantly lower than 1.
For example for $1\,\text{mm}$ layer of Ar: $n_{\text{primary}} = 2.5 \rightarrow e_{\text{det}} = 0.92$.

Consider a $10\,\text{mm}$ thick Ar layer

$$\rightarrow n_{\text{primary}} = 25 \rightarrow e_{\text{det}} = 1$$
$$\rightarrow n_{\text{total}} = 80 - 100$$

100 electron/ion pairs created during ionization process are not easy to detect.

Typical noise of the amplifier $\approx 1000\text{e}^-$ (ENC) $\rightarrow$ we will increase the number of charge carriers by gas amplification.

Single Wire Proportional Chamber

Electron Drift Towards Anode: When electrons are liberated by ionization, they drift towards the anode wire due to the electric field applied within the detector.

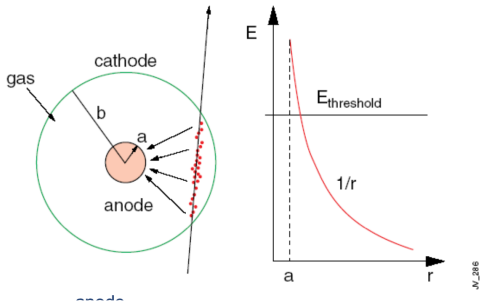

- **Avalanche Effect:** As electrons approach the anode wire, the electric field strength increases significantly (see the graph). In regions where the electric field exceeds a certain threshold (typically above 10 kV/cm), electrons gain enough energy to ionize further gas molecules, leading to an avalanche effect—a rapid and exponential increase in the number of electron-ion pairs.

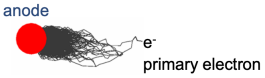

- Here the formulas for electric field and electric potential:

$$E(r) = \frac{CV_0}{2\pi\epsilon_0}\frac{1}{r}$$
$$V(r) = \frac{CV_0}{2\pi\epsilon_0} ln(\frac{r}{a})$$

Geometry and Electric Field: Cylindrical geometry (commonly found in proportional counters) is not the only configuration capable of generating a

strong electric field. Other geometries, such as parallel plate, strip, hole, or groove configurations, can also create strong electric fields conducive to avalanche multiplication.

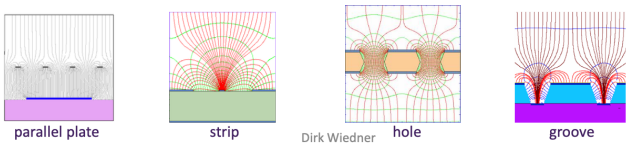

What are the interesting properties that we want to use?

The multiplication of ionization is described by the first Townsend coefficient $a(E)$

$$dn = n \cdot \alpha dx \qquad \alpha = \frac{1}{\lambda} \qquad \lambda\text{-mean free path}$$
$$n = n_0 e^{\alpha(E)x} \quad \text{or} \quad n = n_0 e^{\alpha(r)x}$$

- $\alpha(E)$ is determined by the excitation and ionization cross sections of the electrons in the gas.It depends also on various and complex energy transfer mechanisms between gas molecules.

There is no fundamental expression for $\alpha(E) \rightarrow$ it has to be measured for every gas mixture.

From α we can arrive at the following expression:

$$M = \frac{n}{n_0} = \exp\left[\int_a^{r_C} \alpha(r)dr\right]$$

Amplification factor or Gain with $(E/p =$ reduced electric field $)$

In this plot we can see that that depending on the mixture, we get more or less collisions

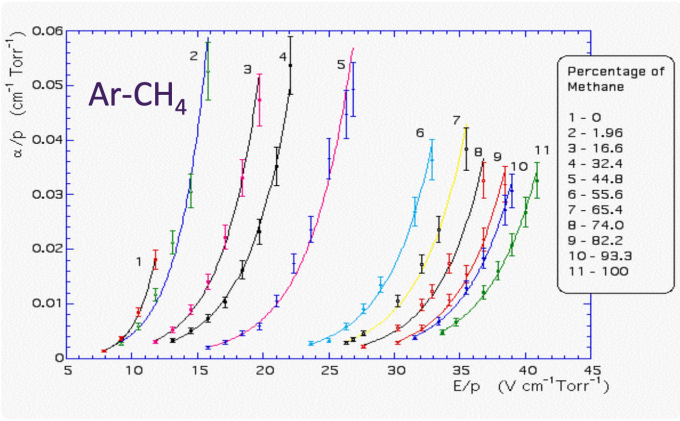

SWPC – Choice of Gas

Ionization Dominance in Noble Gases:

- In noble gases like argon, ionization is the predominant process during interactions with incoming particles.
- There are also excited states, but ionization is the primary effect observed.

De-excitation of Noble Gases:

- Noble gases de-excite by emitting photons.
- Example: Argon emits photons with an energy of 11.6 eV during de-excitation.

Energy Thresholds:

- *The energy level of emitted photons from noble gases (e.g., 11.6 eV for argon) is above the ionization threshold of many metals (e.g., copper at 7.7 eV).*
- This high energy can cause **new avalanches** and lead to permanent discharges, which are undesirable.

This is the process graphically explained:

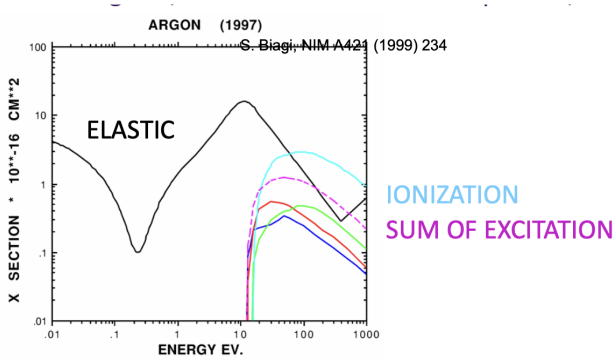

Solution: Polyatomic Gas Quencher:
Adding a polyatomic gas acts as a quencher: polyatomic gases absorb photons over a large energy range due to many vibrational and rotational energy levels.

Graph for explanation for CO2:

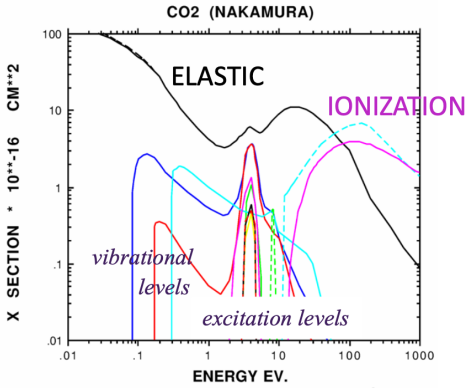

Explanation graph:

Relevance to Single Wire Proportional Chamber:

- In a proportional chamber, electrons liberated by initial ionization drift towards the anode wire.
- As they gain energy in the high electric field near the anode, their energy increases, transitioning from the low to high energy regime on the graph.
- Initially, electrons scatter elastically (black curve) and can cause vibrational and electronic excitations (colored curves).

2. **Quenching Effect of CO2:**

- CO2 acts as a quenching gas in proportional chambers, absorbing excess energy through various excitation states.
- The vibrational and electronic excitation levels allow CO2 to absorb a wide range of photon energies, preventing further ionization and stabilizing the avalanche multiplication.

3. **Preventing Continuous Discharges:**

- The absorbed energy by CO2 reduces the probability of continuous avalanches by dissipating energy through collisions or dissociation into smaller molecules.

SWPC – Operation Modes

In the plot there is the voltage on the x axis and the # of ions collected on the y.

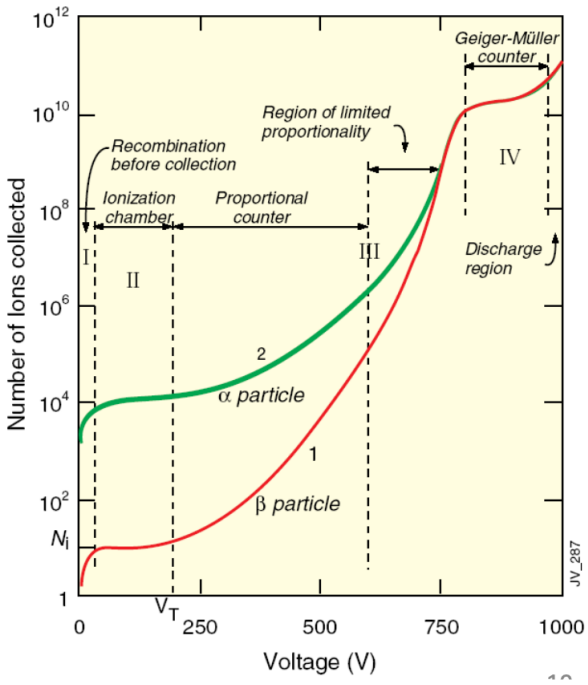

The plot is divided in regions.

I Recombination before collection

• **Description:** At very low voltages, ionized electrons and ions tend to recombine before they can be collected by the electrodes.
• **Recombination:** Electrons and ions that are produced by ionizing radiation may recombine back into neutral atoms or molecules before they reach the anode or cathode.
• **Voltage Effect:** As the applied voltage increases, the electric field strength also increases, reducing the likelihood of recombination because the electrons and ions are more quickly swept to their respective electrodes.
• **Signal Collection:** Only a small fraction of the created ion pairs are collected at very low voltages.

II. Ionization chamber

- **Description:** When the voltage is sufficiently increased, the ionization chamber operates in a regime where all ion pairs created by the radiation are collected, but without any further multiplication.
- **Charge Collection:** In this region, the electric field is strong enough to collect all the ion pairs produced by the ionizing radiation before they can recombine.
- **No Multiplication:** The collected charge is directly proportional to the amount of ionizing radiation; no additional ionization occurs.
- **Flat Curve:** The curve flattens after a certain threshold voltage V_T, indicating that further increases in voltage do not lead to more collected charge because all ion pairs are already being collected.
- **Gain:** The gain is approximately 1, meaning the signal corresponds directly to the number of initial ion pairs created by the radiation.

III. Proportional counter

- **Description:** Beyond a certain voltage threshold, the detector enters the proportional counter region where primary ionization electrons gain enough energy to cause further ionizations, leading to an avalanche effect.
- **Secondary Ionization:** Electrons accelerated by the electric field gain enough kinetic energy to ionize additional gas molecules, creating more electrons and ions.
- **Avalanche Process:** This leads to an exponential increase in the number of collected ions, known as an avalanche. The total collected charge is proportional to the initial ionization event.
- **Useful Range:** This region is useful because the amount of charge collected is proportional to the energy of the incoming radiation, allowing for energy measurements.
- **Distinguishing Particles:** The green curve (alpha particles) and the red curve (beta particles) show different ionization levels, allowing the detector to distinguish between different types of radiation based on their energy deposition.
- **Quenching Requirement:** Quenching gases are needed to absorb excess energy and prevent continuous avalanches that would lead to discharges.

- **Gain:** The gain in this region ranges from 10^4 to 10^5, providing significant signal amplification.

IV. Region of limited proportionality:

- **Description:** As the voltage increases further, additional processes like excitation and de-excitation become significant, leading to the emission of UV photons.
- **UV Photons:** These photons can ionize additional gas atoms, causing secondary ionizations that are not directly proportional to the initial ionization event.
- **Photon Absorption:** UV photons emitted during de-excitation are absorbed by other gas atoms, leading to further ionization.
- **Curve Merging:** The red and green curves start to merge, indicating similar ionization levels for different particles due to the non-linear amplification.
- **Strong Photoemission:** Photoemission becomes significant, causing secondary avalanches to merge with the primary one, resulting in larger signals.
- **Quenching and Electronics:** Requires strong quenching or pulsed high voltage to control the signal, but the large signals allow for simpler electronics.
- **Gain:** Gain is around 10^{10}, providing very high signal amplification but with reduced proportionality.

V. Geiger-Muller counter:

- **Description:** At very high voltages, the detector operates in the Geiger-Müller region, where a single ionizing event can trigger a discharge that spreads along the entire anode wire.
- **Massive Photoemission:** Photoemission leads to ionization along the entire length of the anode wire.
- **Discharge Control:** The discharge is stopped by cutting off the high voltage or by using quenching gases to absorb the energy.
- **Quenching Requirement:** Strong quenchers are essential to stop the discharge and prevent continuous operation.
- **Gain:** Gain can be extremely high, often leading to a situation where the signal is independent of the initial ionization event’s energy.

Discharge region:

- **Description:** In this region, the detector experiences continuous discharge, similar to the operation of fluorescent tube lights.
- **Behavior:** The detector cannot operate properly because the high voltage causes continuous ionization and discharge, preventing accurate measurement of ionizing events.

SWPC – Signal Formation

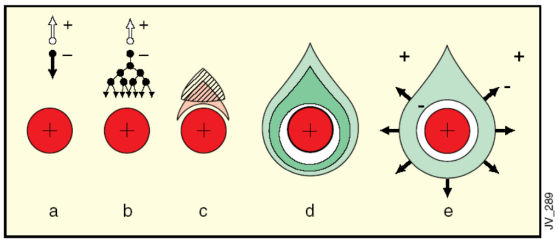

The proportional gas counters are based on the secondary ionization process which occurs only when the high voltage is applied between the anode and the cathode. When strong electric field is applied between the electrodes, the electrons are attracted to the anode and the collision between the accelerated electrons and neutral gas molecules supervenes. These collisions generate the Townsend avalanche.
The time development of the Townsend avalanche is shown in Figure above.

Firstly an ion-electron pair is created by the primary ionization (a). The created electron is accelerated by the electric field toward the anode, while next electrons are created (b) due to the collisions with neutral gas molecules. The electrons surround the anode, grouping in a drop-shaped avalanche (c, d). This process is terminated when all the free electrons are collected on the anode (very fast process lasting approximately 1 ns). However, the positive ions have lower drift velocity than the electrons, so there is still a cloud of them moving slowly toward the cathode (d).

1. **Electrons Collected by Anode Wire:**
    - The electrons move quickly towards the anode wire and are collected over a small distance (few mm).
    - They contribute only a small fraction to the total detected signal because their collection happens rapidly.
2. **Ions Drift Back to Cathode:**
    - The positive ions drift towards the cathode over a larger distance (few mm).
    - The signal duration is largely determined by the ion drift time, which is slower compared to electron collection.

Avalanche Formation:
- Occurs within a few wire radii and within less than 1 ns.
- This rapid process induces signals on both the anode and cathode due to the movement of electrons and ions.

- **Signal Induction:**
    - Signals are induced on both the anode and cathode due to the movement of charges (electrons and ions).
    - The induced voltage change (dv) is described by the equation:

$$dv = \frac{Q}{LCV_0}\frac{dV}{dr}$$

where Q is the charge, L is the inductance, C is the capacitance, and

V_0 is the applied voltage.

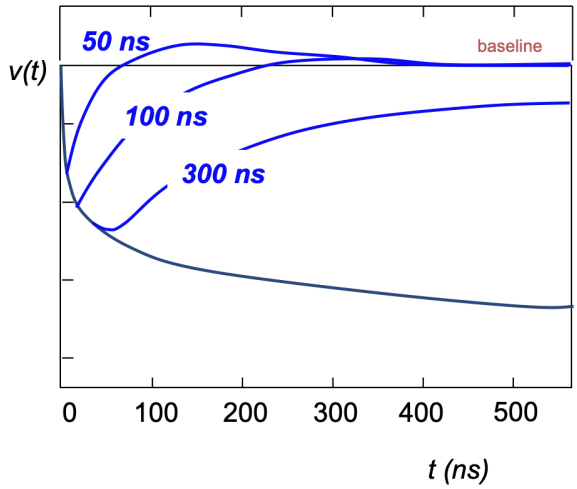

er

3. **Need for Electronic Signal Differentiation:**
   - To limit dead time (the time during which the detector is unable to record another event), electronic signal differentiation is needed.
   - This helps in separating the fast electron signal from the slower ion signal, improving the detector's response time.

Multi-Wire Proportional Chamber (MWPC):

MWPCs consist of a series of parallel wires stretched across a gas-filled chamber.

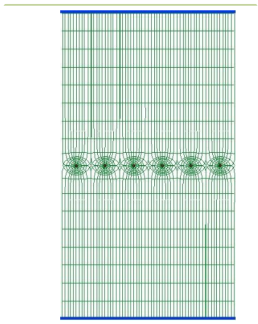

When a charged particle passes through the chamber, it ionizes the gas along its path, creating electron-ion pairs. The electric field between the wires causes the electrons to drift towards the anode wires, where they induce signals proportional to their charge. Due to the electric field configuration, electrons from a single ionization event can trigger avalanches, resulting in signal amplification.

This amplification allows for precise localization of the particle's trajectory and can be used for particle tracking in experiments. The concept of using multi-wire proportional chambers was awarded the Nobel Prize in Physics in 1992.

CSC – Cathode Strip Chamber:

CSCs are a type of gaseous detector. They consist of arrays of positively-charged anode wires crossed with negatively-charged copper cathode strips within a gas volume.

When muons pass through, they knock electrons off the gas atoms, which flock to the anode wires creating an avalanche of electrons. Positive ions move away from the wire and towards the copper cathode, also inducing a charge pulse in the strips, at right angles to the wire direction.

Because the strips and the wires are perpendicular, we get two position coordinates for each passing particle.

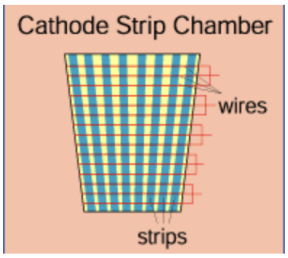

RPC – Resistive Plate Chamber:

RPCs are gas detectors consisting of two parallel plates separated by a gas volume and equipped with resistive electrodes on the inner surfaces. When a charged particle passes through the gas volume, it ionizes the gas, creating electron-ion pairs.

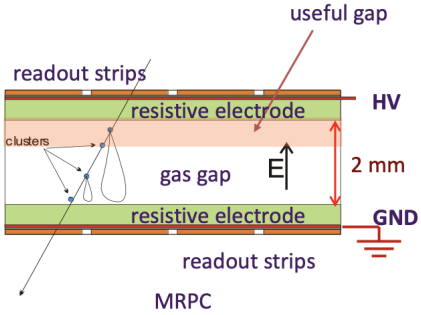

The resulting electrons drift towards the anode, while the positive ions drift towards the cathode. If the electric field is sufficiently high, the electrons can trigger avalanches, resulting in a detectable signal. RPCs are known for their fast response time and are often used in high-rate environments, such as in the trigger systems of particle detectors in high-energy physics experiments. (CMS)

0:00 / 1:22:22

LT7

Gaseous detectors 2

Diffusion of Free Charges

Free Ionization Charges Energy Loss and Diffusion

Free ionization charges lose energy in collisions with gas atoms and molecules (thermalization).

This is described by the Maxwell-Boltzmann Energy Distribution

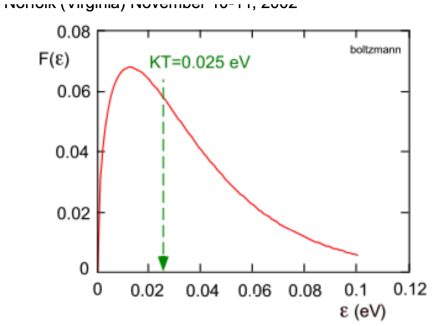

The Maxwell-Boltzmann energy distribution describes the probability of finding a particle with energy ϵ in a gas at thermal equilibrium. It is given by:

$$F(\epsilon) \propto \sqrt{\epsilon} \cdot e^{-\frac{\epsilon}{kT}}$$

The average thermal energy of free ionization charges can be approximated using the equation:

$$\epsilon_r = \frac{3}{2} kT \approx 0.040\,\mathrm{eV}$$

Diffusion Equation

The diffusion equation describes the fraction of free charges at a distance x after time t:

$$\frac{dN}{N} = \frac{1}{\sqrt{4\pi Dt}} e^{-\frac{x^2}{4Dt}} dt$$

where D is the diffusion coefficient.
The root mean square (RMS) of linear diffusion is given by:

$$\sigma_x = \sqrt{2Dt}$$

Plot Diffusion of Ions in Air:

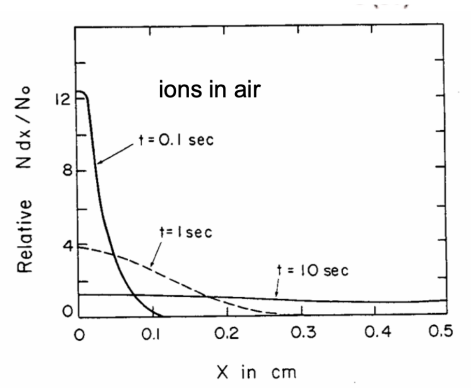

- This plot shows the relative number of ions $\frac{N \cdot dx}{N_0}$ as a function of distance x in cm for different times.

- The curves represent the diffusion of ions in air at $t = 0.1$ sec, $t = 1$ sec, and $t = 10$ sec.

- As time increases, the ions spread further from the origin, demonstrating diffusion.

In particle identification we want to use an external field to have drift and avalanches. In realty because the temperature is more than zero Kelvin, the electrc field is non zero.

This is a simplified picture of what will happen

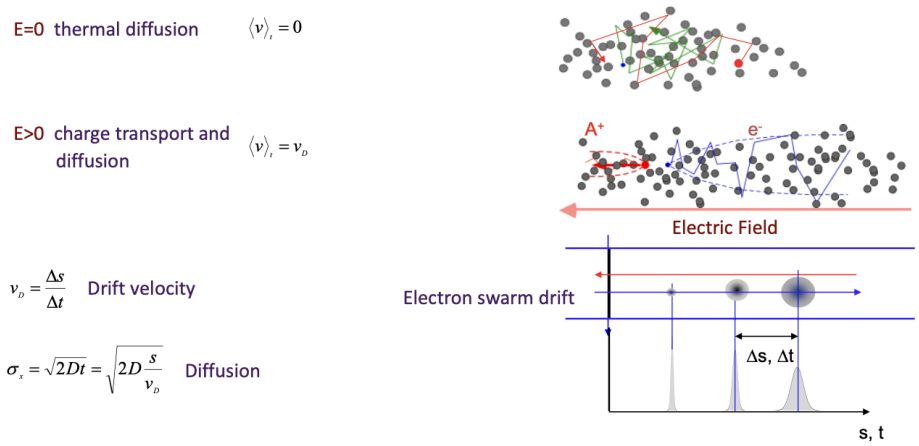

The electrons drift and those electros are not point like anymore, they form a Gaussian shape (simplify in 1d), after further time the gaussian distribution is wider.

Definitions:

Drift Velocity

The drift velocity v_D is defined as the displacement Δs of charges over the time interval Δt:

$$v_D = \frac{\Delta s}{\Delta t}$$

Diffusion

The root mean square (RMS) of linear diffusion (\sigma_x) can be expressed in two equivalent forms:

$$\sigma_x = \sqrt{2Dt} = \sqrt{\frac{2D \cdot s}{v_D}}$$

where:

- D is the diffusion coefficient.
- t is the time.
- s is the displacement.

Some people tried to describr this in formulas: **Simplified Electron Transport Theory**

Let's see how they did:

Townsend expression:

$$v_D = a\tau = \frac{eE}{m}\tau = \mu E$$

Time between collisions τ:

$$\tau = \frac{1}{N\sigma(\epsilon)\nu}$$

Energy balance:

$$\frac{x}{v_D\tau}\lambda(\epsilon)\epsilon_E = eEx$$

collision losses = energy gained in E-field

Number of collisions:

$$\frac{x}{v_D\tau}$$

Fractional energy loss per collision:* $\lambda(\epsilon)$

Equilibrium energy (excl. thermal motion):

$$\epsilon_E = \frac{1}{2}m\nu^2$$

with ν = instantaneous velocity

By plugging the definition of τ in the definition of the drift velocity, also using the definition of the number of collisions and the energy equilibrium we find:

$$v_D^2 = \frac{eE}{mN\sigma(\epsilon)}\sqrt{\frac{\lambda(\epsilon)}{2}}$$

So there are several consequences:

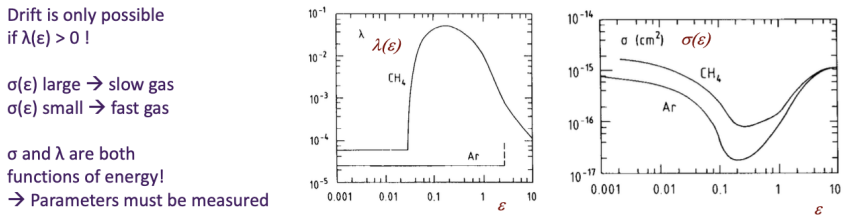

- **Energy Transfer $\lambda(\epsilon)$:** For CH_4, the energy transferred per collision increases after a certain threshold but then decreases after a while. This indicates a peak in energy transfer efficiency at a specific energy level.
- **Collision Cross Section $\sigma(\epsilon)$:** The graph shows that the collision cross-section (σ_ϵ) for CH_4 decreases significantly around $\epsilon \approx 0.2$

Let's see those plots now:

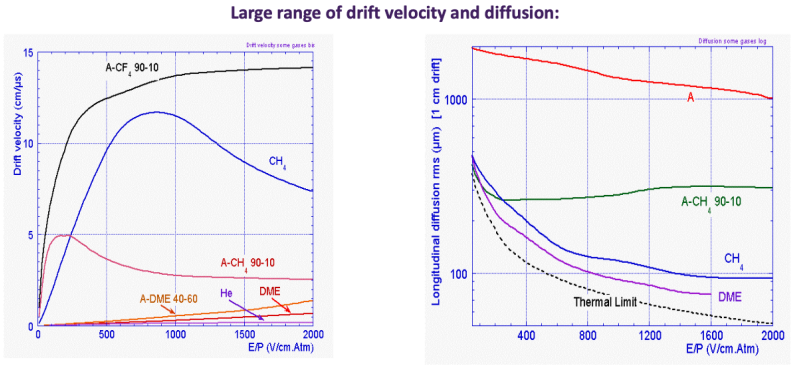

Left Graph: Drift Velocity

- **Drift Velocity vs. Electric Field (E/P):** This graph depicts the drift velocity of electrons as a function of the electric field (E) divided by the nominal atmospheric pressure (P) per centimeter.
  - CF_4 (90-10): Previously used due to its high drift velocity, CF_4 is less favored now because of environmental concerns, particularly its impact on climate change.
  - CH_4: Commonly used nowadays, CH_4 offers moderate drift velocities.
  - A-CH (90-10): Notable for its constant drift velocity, making it useful for detector calibration.

Right Graph: Longitudinal Diffusion

- **Longitudinal Diffusion (LD):** This refers to the spread of electrons in the direction of the drift.
  - **Argon-CH_4 Mixture:** Shows a large but constant longitudinal diffusion, which might be beneficial for certain applications.
  - **Argon:** Exhibits extremely high longitudinal diffusion, typically undesirable for precision measurements.

Tule of thumb: The drift velocoty of electrons is 5 cm/us

Rule of thumb: v_D (electrons) ~ 5 cm/μs = 50 μm / ns. Ions drift ~1000 times slower.

Now those graphs:

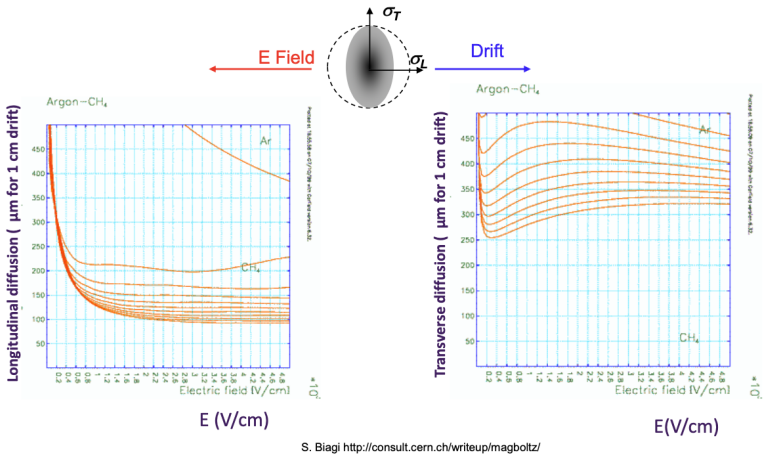

This graph is saying that the diffusion along the path of the electron is different from the diffusion along the perpendicular direction.

Longitudinal diffusion is overall smaller.

The measurement are a function of the electric field.

Drift Chambers

In the end we want to measure the spatial coordinate and for doing this we also use the **time** of arrival. How do we do it in practice?

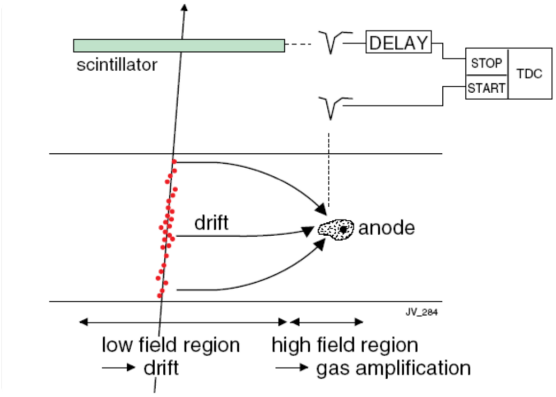

Measuring Electron Arrival Time

We can measure the time it takes for an electron to arrive at the anode. Specifically, we measure the arrival time of electrons at the sense wire relative to a time t_0.

Trigger Requirement

To get the start time, we use external information, usually a scintillator, which indicates the start time of the electron's movement in the detector.

Timing Mechanism

The physical start signal is counted as a stop signal because we apply a known delay. The physical stop signal (electrons at the anode) is recorded and used as the start signal. Then, everything goes to the Time to Digital Converter (TDC) and gets converted.

Resolution Determination

The resolution is determined by several factors:

- Diffusion
- Primary ionization statistics (if you have high ionization statistics, the number of electrons produced when a charged particle passes through the detector)
- Path fluctuations and electronics

Example of Real Measurement:

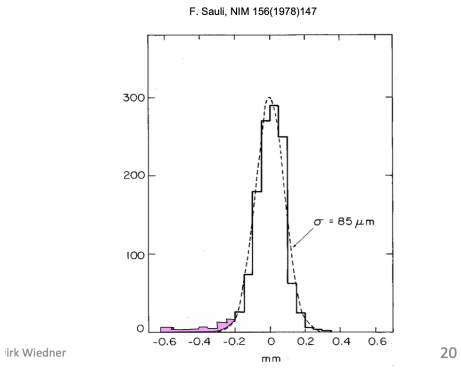

In reality, instead of having ONE SINGLE WIRE we have huge areas of detectors covered by a lot of wires.

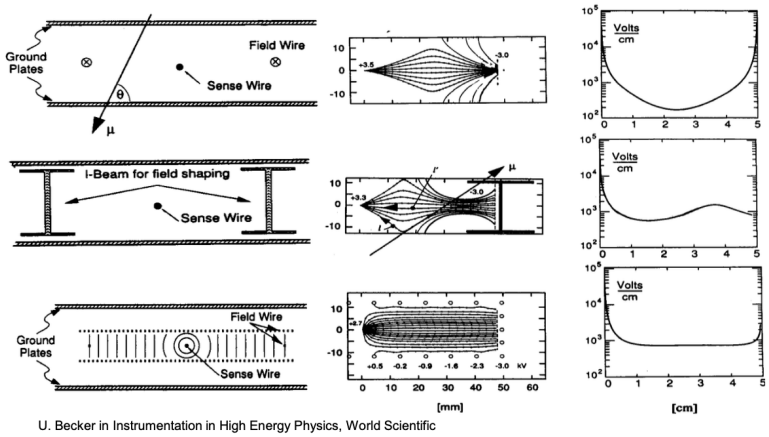

U. Becker in Instrumentation in High Energy Physics, World Scientific

First picture: The first picture shows a detector setup where multiple wires are used instead of a single wire. This arrangement helps in covering a larger

area of the detector, improving its efficiency and accuracy.

Second picture: The second picture depicts the electric field generated in the detector setup. This configuration provides a more constant electric field, which is advantageous for the detection process.

Thirs picture: Plot of the intensity of the electric field The last picture presents a plot showing the intensity of the electric field. This plot demonstrates that the electric field is more constant, which is beneficial for precise measurements.

The second row is better than the first one because the E is more constant but overall the last is the best because it's more constant.

Momentum measurement - Intermezzo

After the collision of 2 protons for example you get a lot of particles. If you want to measure the momentum of those a particles you use the magnetic field to measure them that in the fist picture is parallel to the beam pipe.

We see that the particles that experience the magnetic field they get bend. The second row of the plot is the a different perspective of the same interaction.

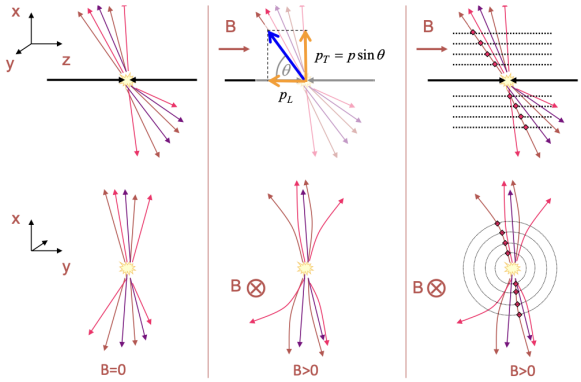

In practice?

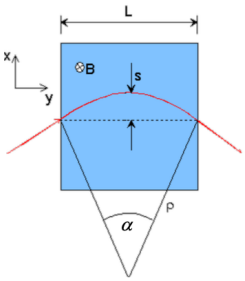

We measure only p-component transverse to B field !

$$p_T = qB\rho \quad \rightarrow \quad p_T\,(\mathrm{GeV/c}) = 0.3B\rho \quad (\mathrm{T\cdot m})$$

$$\frac{L}{2\rho} = \sin\alpha/2 \approx \alpha/2 \quad \rightarrow \quad \alpha \approx \frac{0.3L\cdot B}{p_T}$$

$$s = \rho(1-\cos\alpha/2) \approx \rho\frac{\alpha^2}{8} \approx \frac{0.3}{8}\frac{L^2B}{p_T}$$

Determination of Sagitta with Error s(x)

The sagitta s is determined by three measurements with error s(x):

$$s = x_2 - \frac{x_1 + x_3}{2}$$

The relative error in the transverse momentum measurement is:

$$\left(\frac{\sigma(p_T)}{p_T}\right)^{\text{meas.}} = \frac{\sigma(s)}{s} = \frac{\sqrt{\frac{3}{2}}\sigma(x)}{s} = \frac{\sqrt{\frac{3}{2}}\sigma(x)\cdot 8p_T}{0.3\cdot BL^2}$$

Hence,

$$\left(\frac{\sigma(p_T)}{p_T}\right)^{\text{meas.}} \propto \frac{\sigma(x)\cdot p_T}{BL^2}$$

For N equidistant measurements, one obtains:

$$\left(\frac{\sigma(p_T)}{p_T}\right)^{\text{meas.}} = \frac{\sigma(x)\cdot p_T}{0.3\cdot BL^2}\sqrt{\frac{720}{(N+4)}} \quad (\text{for } N \geq\sim 10)$$

Multiple scattering considerations

If you use a gas detector the particle will be scatter n the matririal iteself and we have to take this into account.

If we assume that this multiple scattering term will stay constant we geta total momentum resolution

$$\frac{\sigma(p)}{p_T} \propto \sigma(x)\cdot p_T$$

- The error in position due to multiple scattering $\sigma(x)$ is proportional to the scattering angle θ_0 , which is inversely proportional to the momentum p:

  $$\sigma(x)^{\text{MS}} \propto \theta_0 \propto \frac{1}{p}$$

  Thus, the relative error in transverse momentum due to multiple scattering $\left(\frac{\sigma(p)}{p_T}\right)^{\text{MS}}$ is constant, i.e., independent of p :

  $$\frac{\sigma(p)}{p_T}^{\text{MS}} = \text{constant}$$

In the low momentum the total function will be govern by the multiple scattering, in the high momentum range the line will be more straight since the particle are very fust, in the detector not oso much will happen

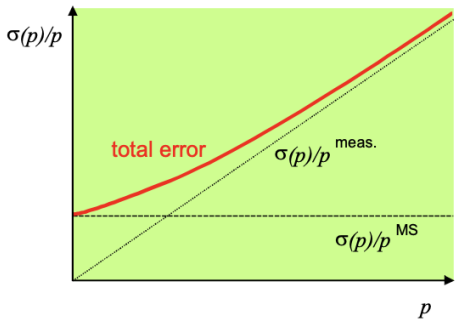

- The red line represents the total error, combining both measurement error and multiple scattering error.
- The dashed line \sigma(p)/p represents the error due to measurements.
- The dotted line \sigma(p)/p represents the error due to multiple scattering.

As illustrated, the measurement error increases with momentum, while the multiple scattering error remains constant, independent of momentum.

Example:

Example:

$p_t = 1$ GeV/c, $L = 1$m, $B = 1$ T, $N = 10$

$\sigma(x) = 200$ μm: $\left.\frac{\sigma(p_T)}{p_T}\right|^{meas.} \approx 0.5\%$

Assume detector (L = 1m) to be filled with 1 atm. Argon gas (X_0 = 110m),

$\left.\frac{\sigma(p)}{p_T}\right|^{MS} \approx 0.5\%$

Now, lets look again the Drift in presence of E and B Fields.

Equation of Motion of Free Charge Carriers in the Presence of Electric and Magnetic Fields

The motion of free charge carriers, such as electrons, in the presence of electric $\vec{E}$ and magnetic $\vec{B}$ fields is governed by the following equation:

$$m\frac{d\vec{v}}{dt} = e\vec{E} + e(\vec{v} \times \vec{B}) + \vec{Q}(t)$$

where:

- $\vec{Q}(t)$ is the stochastic force resulting from collisions: how the particles hits the gas and slow down.

Time-Averaged Solutions

Assuming time-averaged solutions with $\vec{v}_D = \langle \vec{v} \rangle = \text{const.}$ and $\langle \vec{Q}(t) \rangle = \frac{m}{\tau}\vec{v}_D$ (friction force), we get:

$$\left\langle \frac{d\vec{v}}{dt} \right\rangle = 0 = e\vec{E} + e(\vec{v}_D \times \vec{B}) - \frac{m}{\tau}\vec{v}_D$$

- τ is the mean time between collisions.

Drift Velocity $\vec{v}_D$:
The drift velocity $\vec{v}_D$ is given by:

$$\vec{v}_D = \frac{\mu|\vec{E}|}{1+\omega^2\tau^2}\left[\hat{E} + \omega\tau(\hat{E}\times\hat{B}) + \omega^2\tau^2(\hat{E}\cdot\hat{B})\hat{B}\right]$$

where:

- $\mu = \frac{e\tau}{m}$ is the mobility.
- $\omega = \frac{eB}{m}$ is the cyclotron frequency: frequency that the a free charged particle will have in a field.

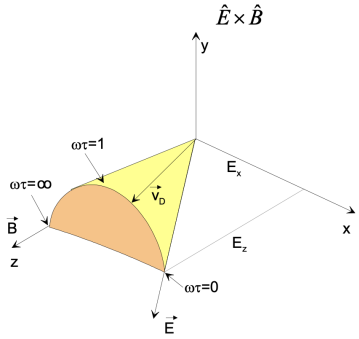

Special Cases:

$B=0 \rightarrow \vec{v}_D^{\,B} = \vec{v}_D^{\,0} = \mu\vec{E}$

$\vec{E} \parallel \vec{B} \rightarrow v_D^B = v_D^0$

$\vec{E} \perp \vec{B} \rightarrow v_D^B = \frac{E}{B}\frac{\omega\tau}{\sqrt{1+\omega^2\tau^2}}$

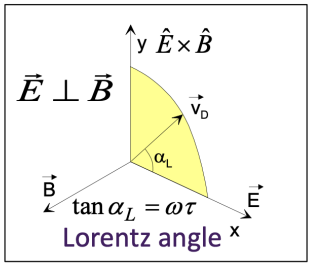

14.05.2024

Conclusion:

- For $\omega\tau \ll 1$, particles predominantly follow the E field.
- For $\omega\tau \gg 1$, particles predominantly follow the B field.

How this effect the measurements? *Diffusion Magnetic Anisotropy*

If you witch on the magnetic field the σ_T will decrease with the increase of the magnetic field.

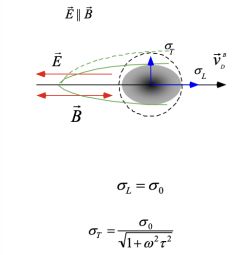

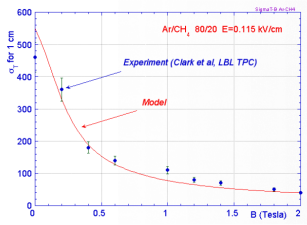

TPC – Time Projection Chamber

Time Projection Chamber full 3D track reconstruction: x-y from wires and segmented cathode of MWPC (or GEM) z from drift time

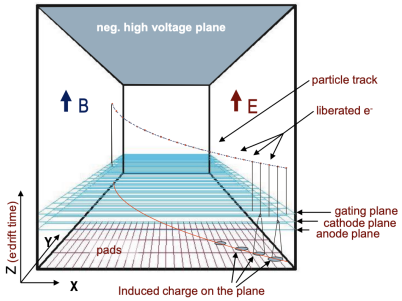

- momentum resolution
  space resolution + B field
  (multiple scattering)
- energy resolution
  measure of primary ionization

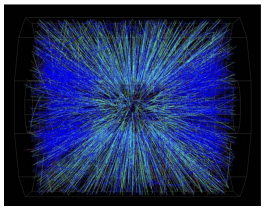

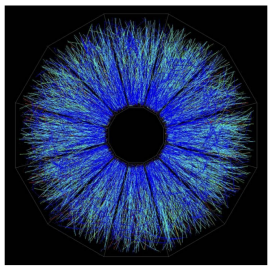

Events from STAR TPC at RHIC
Au-Au collisions at CM energy of 130 GeV/n
Typically ~2000 tracks/event

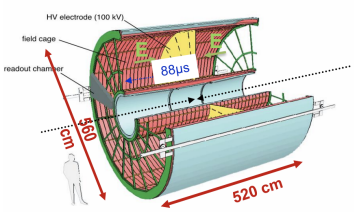

Alice TPC
HV central electrode at –100 kV
Drift length 250 cm at E = 400 V/cm
Gas Ne-CO_2 90-10
Space point resolution ~500 µm
dp/p = 2%@1GeV/c; 10%@10 GeV/c

Micro Pattern Gas Detectors (MPGD)

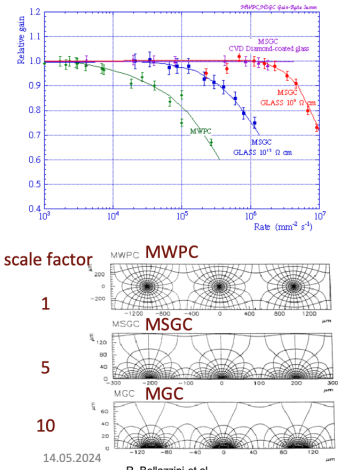

General advantages of gas detectors:

- low radiation length
- large areas at low price
- flexible geometry
- spatial, energy resolution …

Main limitation:

- rate capability limited by space charge defined by the time of evacuation of positive ions

Solution:

- reduction of the size of the detecting cell (limitation of the length of the ion path) using chemical etching techniques developed for microelectronics and keeping at same time similar field shape.

14.05.2024 Dirk Wiedner 29

MSGC – Micro Strip Gas Chamber

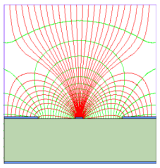

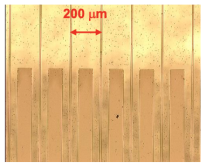

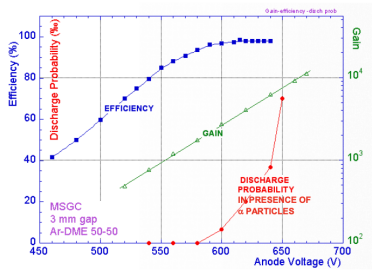

Thin metal anodes and cathodes on insulating support: glass, flexible polyimide …

Problems:

High discharge probability under exposure to highly ionizing particles caused by the regions of very high E field on the border between conductor and insulator.

Charging up of the insulator and modification of the E field → time evolution of the gain.

insulating support slightly conductive support

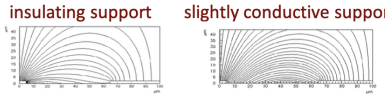

R. Bellazzini et al.

Solutions:

- slightly conductive support
- multistage amplification

Micromegas– Micromesh Gaseous Structure

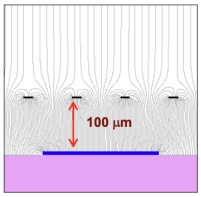

micromesh

Metal micromesh mounted above readout structure (typically strips).

E field similar to parallel plate detector.

E_a/E_i ~ 50 to ensure electron transparency and positive ion flow back suppression.

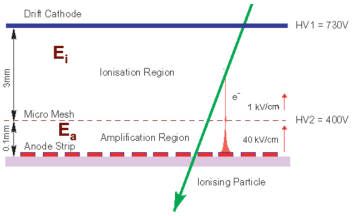

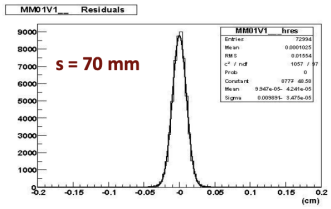

Spatial resolution

0:00 / 1:28:55

LT8

Basics of Semiconductor Detectors

Limits of Gas-Filled Detectors

1. **Low Drift Velocity**
   - Limits hit rate
2. **Mechanics of the Wires**
   - Limits spatial resolution
3. **Large Ionisation Energy**
   - Results in a small signal

Semiconductors as Sensitive Material

- **Advantages:**
  - **Small Ionisation Energy and High Density**
    - Larger signal and better energy resolution
  - **High Charge Carrier Mobility**
    - Fast signal, resulting in a high hit rate
  - **Profit from Image Sensor and Processor R&D**
    - Leverages advancements in technology
- **Challenges:**
  - High Energy Physics (HEP) is a small customer in the market.

Materials Overview

material	band gap [eV]	intrins. charge carrier density [cm^{-3}]	average Z	w_{eh} [eV]	μ_e [cm^2/Vs]	μ_h [cm^2/Vs]
silicon	1.12	$1.01*10^{10}$	14	3.61	1450	505
germanium	0.66	$2.4*10^{13}$	32	2.96	3900	1800
GaAs	1.42	$1.8*10^{6}$	32	4.35	8800	320
CdTe	1.44	10^{7}	50	4.43	1050	100
diamond	5.48	≈0	6	13.1	1800	1400

- **Silicon:** is the best known material, but there are many others
- **Germanium:** Higher charge carrier density and mobility, but lower band gap.
- **GaAs:** High electron mobility but low hole mobility.
- **CdTe:** High atomic number and good for energy resolution.
- **Diamond:** Exceptional properties but challenging to utilize due to high band gap.

Semiconductor Physics

1. Intrinsic Semiconductors

- Very few impurities with respect to the number of thermally stimulated charge carriers, e.g. high-purity silicon

Reminder: Band model
-> highest energy occupied states: Valence Band
-> lowest energy free states: Conduction Band

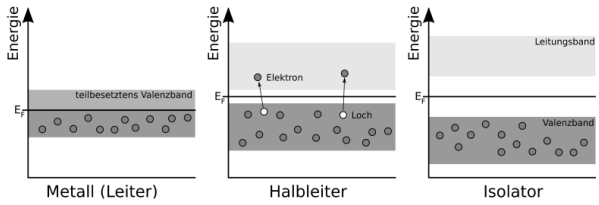

Band Gap and Charge Carriers in Silicon

The band gap in silicon is $1.1eV$, which allows electrons to be thermally excited into the conduction band at **room temperature**.

When an electron is excited in this manner, it leaves behind a covalent bond with one "missing" electron. This "missing" electron can be filled by a neighboring electron, and the resulting wandering "missing" electron is described as a positive charge carrier, known as a hole.

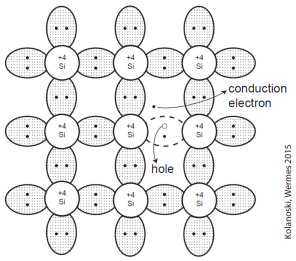

Silicon is classified as an **indirect semiconductor**, meaning that the minimum of the valence band (VB) and the minimum of the conduction band (CB) lie at different wave vectors (k).

This distinction requires momentum transfer to the crystal lattice for excitation or de-excitation processes. In contrast, materials like GaAs are direct semiconductors, where the minimum of the VB and CB occur at the same wave vector (k), allowing for direct transitions without the need for momentum transfer.

The mean energy required to create an electron-hole pair in silicon is **3.6 eV**, though this value is dependent on temperature. This property is crucial in determining the efficiency and behavior of silicon in semiconductor applications.

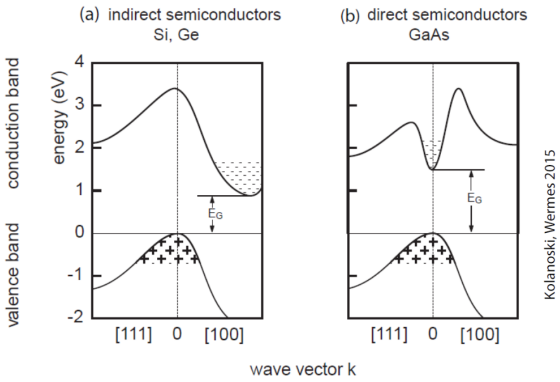

The visual representations of conduction and valence bands in indirect and direct semiconductors show that indirect semiconductors like silicon and germanium require a two-step process involving phonons for electron excitation.
On the other hand, direct semiconductors such as GaAs allow direct transitions between the valence band and the conduction band. This difference significantly impacts their performance and suitability for various applications in electronics and photonics.

Soo this means that there are a lot of electrons in the condution band. How many?

To determine the number of electrons in the conduction band at room temperature, we begin with the occupation probability of charge carriers (fermions), which follows the Fermi-Dirac statistics. The occupation probability $F(E)$ is given by:

$$F(E) = \frac{1}{1 + \exp\left(\frac{E - E_F}{kT}\right)}$$

where E_F is the Fermi energy, k is the Boltzmann constant, and T is the temperature in Kelvin.

Skipping the calculations...

The crystal, as a whole, is electrically neutral, meaning that the concentration of electrons (n) is equal to the concentration of holes ((p)), which is equal to the intrinsic carrier concentration ((n_i)). The Fermi energy ((E_F)) is given by:

$$E_F^i = \frac{E_C + E_V}{2} + \frac{3kT}{4} \ln\left(\frac{m_p}{m_n}\right)$$

where (E_C) and (E_V) are the energy levels at the conduction and valence band edges, respectively, (k) is the Boltzmann constant, (T) is the temperature in Kelvin, and (m_p) and (m_n) are the effective masses of holes and electrons.

At room temperature, the density of free charge carriers in silicon is approximately:

$$n_i \approx 1.01 \times 10^{10}\,\mathrm{cm}^{-3}$$

That is a lot.

This value indicates a significant number of thermally generated charge carriers.

When a minimum ionizing particle (MIP) passes through the sensor, it deposits about 97 electrons per micrometer. For a sensor with a thickness of 300 micrometers, this results in the generation of 30,000 electron-hole pairs. However, this poses a problem because the signal-to-background ratio S/B **is much less than 1**, indicating that the signal generated by the MIP is overwhelmed by the background noise from thermally generated carriers.

To address this issue, we need to consider how to reduce the intrinsic charge carrier density in the sensor.

2. Extrinsic Semiconductors

In order to solve the issue we can add impurities to the charge carrier density.

n-type Doping

n-type doping involves the addition of pentavalent atoms (atoms with five valence electrons). This introduces one additional electron to the semiconductor material. The donor state created by these pentavalent atoms is close to the conduction band edge (EC), making it easy for the extra electron to be excited into the conduction band.

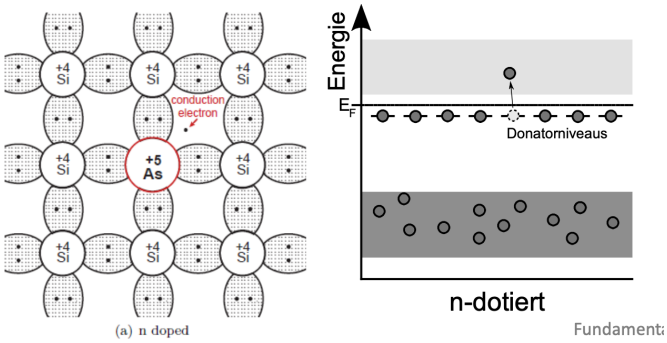

p-type Doping

p-type doping, on the other hand, involves the addition of trivalent atoms (atoms with three valence electrons). This introduces one missing electron, effectively creating one additional hole. The acceptor state formed by these trivalent atoms is close to the valence band edge (EV), facilitating the creation of holes.

-> Typical doping concentration: $10^{12}/10^{16}$ cm^{-3}

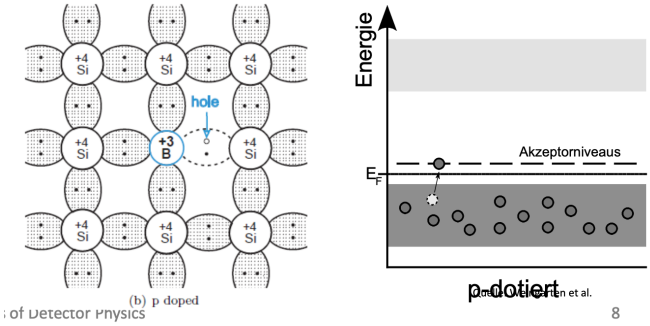

We can combine the things:

When donor and acceptor states are introduced through doping, they alter the Fermi energy levels of the semiconductor.
In thermal equilibrium, the Fermi energy E_F must remain uniform throughout the crystal, causing **shifts** in the conduction band edge E_C and the valence band edge E_V

Diffusion and Depletion

In a pn-junction, free charge carriers diffuse along the concentration gradient:

- Electrons move from the n-doped region into the p-doped region.
- Holes move from the p-doped region into the n-doped region.

As these charge carriers **recombine** near the junction, they create a depleted region **devoid of free charge carriers**. This recombination of charge carriers close to the junction leads to the formation of a space charge region.

Space Charge Region and Electric Field
The localized doping atoms, **now charged**, create an electric field that opposes further diffusion of charge carriers. This electric field counteracts the diffusion current, leading to a dynamic equilibrium. The equilibrium between diffusion and drift currents determines the thickness of the depleted region.

The diagram illustrates this process, showing the drift and diffusion of charge carriers and how the band edges E_C and E_V adjust to maintain equilibrium across the pn-junction.

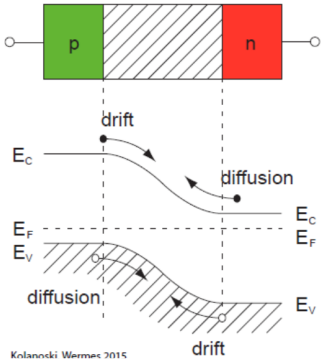

pn Junction under External Voltage

When an external voltage is applied to a pn-junction, it creates an additional electric field that can either reduce the thickness of the depletion region (*1. forward biasing*) or increase the thickness (*2. reverse biasing*).

1. Forward Biasing

In forward biasing, the external voltage reduces the thickness of the depletion region. As the voltage increases, it eventually reaches a point where the depletion region vanishes entirely. At this point, free charge carriers are present throughout the junction, allowing current to flow freely across it.

2. Reverse Biasing

In reverse biasing, the external voltage increases the thickness of the depletion region. As long as the depletion region has a non-zero thickness, no current can flow across the junction, effectively preventing current conduction.

Diode Behavior

The behavior of the pn-junction under different biasing conditions leads to the formation of a diode, a fundamental electronic component that allows current to flow in one direction (forward bias) but not in the opposite direction (reverse bias).

The diagrams illustrate these concepts:

1. The top diagram shows the band structure and depletion region under no external voltage.

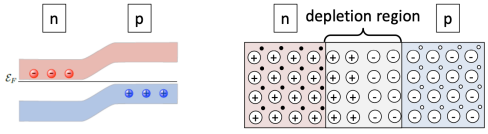

2. The middle diagram shows the junction under forward bias, where the depletion region is reduced, allowing current flow.

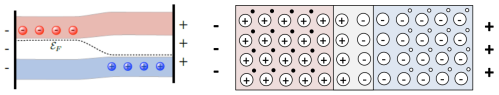

3. The bottom diagram shows the junction under reverse bias, where the depletion region is increased, preventing current flow.

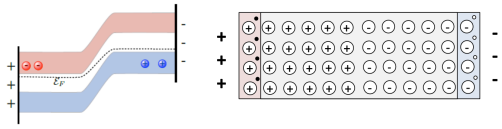

Space-Charge Region and Electric Field

In a semiconductor pn-junction, the space-charge region is created by the immobile ionized donors and acceptors. This region has a built-in electric field ((E)) and potential ((\Phi)) due to the separation of charge carriers.

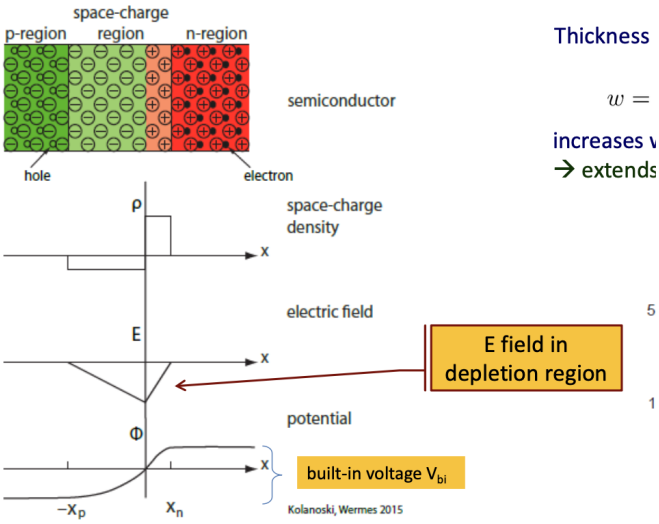

Thickness of Depletion Region

The thickness of the depletion region changes with the application of an external bias voltage V_{bias}. The relationship is given by:

$$w = w_p + w_n + \left\{ \frac{2\epsilon_0 (N_A + N_D)}{q N_A N_D} (V_{\text{bias}} + V_{\text{bi}}) \right\}^{1/2}$$

where:

- w_p and w_n are the depletion widths in the p and n regions, respectively.
- ϵ_0 is the permittivity of free space.
- N_A and N_D are the acceptor and donor concentrations.
- q is the charge of an electron.
- V_{bi} is the built-in voltage.

The thickness of the depletion region increases with the square root of the bias voltage and extends further into the lower doped region.

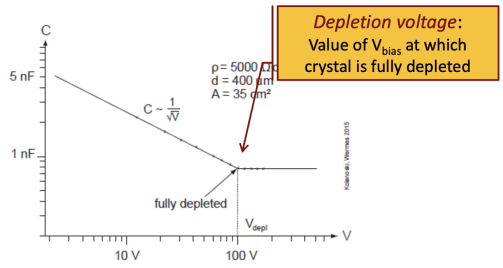

Depletion Voltage

The depletion voltage V_{depl} is the value of V_{bias} at which the crystal is fully depleted. At this voltage, the capacitance C of the junction becomes constant. The graph illustrates how capacitance varies with applied voltage and shows that capacitance is inversely proportional to the square root of the voltage until the depletion voltage is reached.

IV Characteristic of a Diode

The Shockley equation describes the current-voltage (IV) characteristics of a diode under forward bias:

$$I_D(V,T) = I_S(T)\left(e^{\frac{V}{mV_T}} - 1\right)$$

where:

- (I_D) is the diode current.
- (I_S) is the saturation current.
- (V) is the applied voltage.
- (V_T) is the thermal voltage (($V_T = \frac{kT}{q}$)).
- (m) is the ideality factor, typically between 1 and 2 for real diodes.

Temperature Dependence

The saturation current I_S and the slope of the IV curve in forward bias depend on temperature. The relationship between the diode voltage and temperature is given by:

$$\frac{\partial U_D}{\partial T} \approx -2\,\text{mV/K}$$

This means that for each degree Kelvin increase in temperature, the forward voltage drop decreases by approximately 2 millivolts.

Saturation Current and Thermal Runaway

The saturation current is typically in the nanoampere to microampere range and

doubles approximately every 8 degrees Kelvin ((\Delta T \approx 8K)). As the current increases, it raises the junction temperature, which in turn increases the saturation current, leading to a positive feedback loop known as thermal runaway. To prevent this, detectors must be actively cooled.

The graph shows the IV characteristics of a diode:

- In the forward bias region, the current increases exponentially with voltage.
- In the reverse bias region, the current remains very small until breakdown occurs.

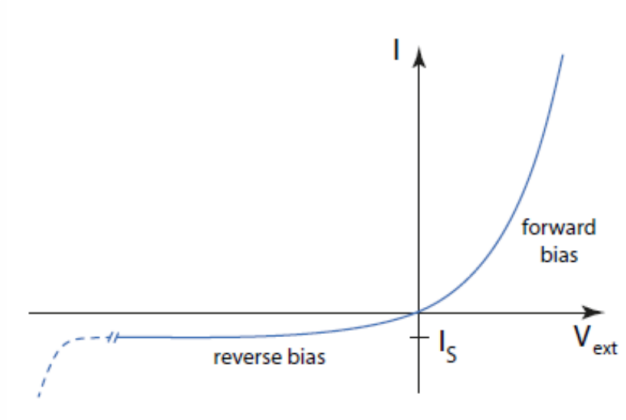

Particle detection

Energy Deposition of a Minimum Ionizing Particle (MIP) in Silicon

The energy deposition of a Minimum Ionizing Particle (MIP) in a 300 µm silicon detector is approximately 0.39 keV/µm, which translates to around 117 keV over 300 µm. This calculation leads to a mean charge deposition of about 32,000 electron-hole pairs per event (approximately 5 femtocoulombs).

Drift Velocity and Signal Collection

At a typical drift velocity of around 50 µm/ns, charge carriers travel very quickly to the collecting electrode. The drift time t_{drift} can be calculated as:

$$t_{\text{drift}} = \frac{d}{v_{\text{drift}}} \approx \frac{300\,\mu\text{m}}{50\,\mu\text{m/ns}} = 6\,\text{ns}$$

This rapid drift time is significantly faster compared to gas-filled detectors, making semiconductor detectors highly efficient for applications requiring fast signal collection.

The graph in the image depicts the energy deposition ((\Delta/x)) distribution for a 500 MeV pion in silicon, represented for different silicon thicknesses:

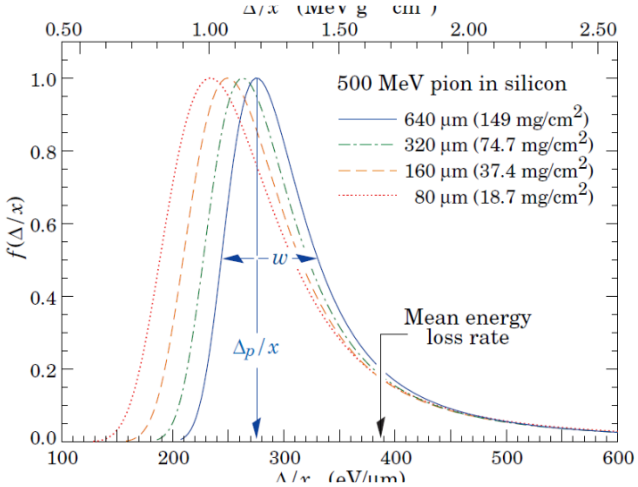

Each curve shows the frequency $f(\Delta/x)$ of energy deposition rates. The x-axis represents the energy deposition per unit length $(eV/\mu m)$, and the y-axis represents the probability density function of energy deposition. The curves indicate how energy deposition varies with the thickness of the silicon detector. The mean energy loss rate and the distribution width (w) are highlighted, demonstrating the relationship
between the thickness of the detector and the energy deposition profile.

-> Very fast in comparison to gas-filled detectors!

Types of Diode Detectors

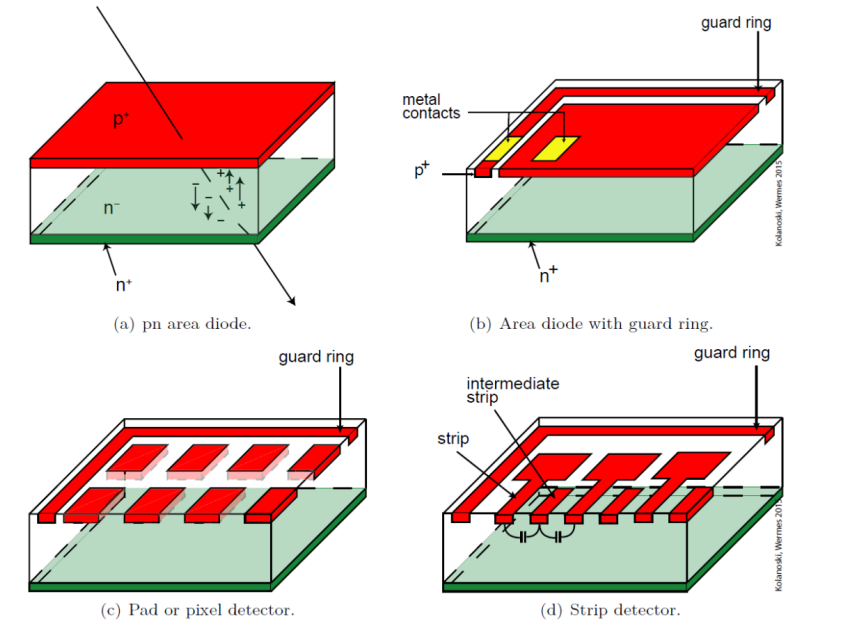

(a) pn area diode. (b) Area diode with guard ring.

(c) Pad or pixel detector. (d) Strip detector.

(a) pn Area Diode

The pn area diode consists of a p+ region and an n+ region. The junction between these regions forms the depletion area where charge carriers (electrons and holes) recombine. This basic structure is widely used in various semiconductor devices for detecting charge carriers.

(b) Area Diode with Guard Ring

An area diode with a guard ring includes a p+ region, an n+ region, and a guard ring surrounding the active area. The guard ring helps in isolating the active region from the edges of the diode, reducing leakage currents and enhancing the performance of the diode by maintaining a more uniform electric field across the junction.

(c) Pad or Pixel Detector

Pad or pixel detectors are structured with multiple small p+ regions embedded in an n+ substrate. Each p+ region acts as an individual detecting element, allowing for spatial resolution of the incident particles. This type of detector is commonly used in imaging applications, where each pixel corresponds to a specific location on the detector surface.

(d) Strip Detector

Strip detectors feature a series of parallel p+ strips in an n+ substrate, with intermediate strips and a guard ring surrounding the active area. The strip design allows for one-dimensional position sensing, making them suitable for tracking and measuring particle trajectories. The intermediate strips help in collecting the charge carriers efficiently and reduce the capacitance of the detector.

Example: Strip Detectors

Strip detectors consist of electrodes segmented into strips on one side, providing one-dimensional spatial information and the radius of the detector plane. The pitch, or distance between the strips, typically ranges from 50 to 100 µm. This design allows for spatial resolution in the short direction between 15 to 30 µm. The typical sensor thickness for strip detectors varies from 100 to 300 µm. The readout electronics are located outside the sensor, making this a hybrid detector.

The illustration of a strip detector shows the electrodes (implantation and contact) and their segmentation into strips on one side of the silicon layer.

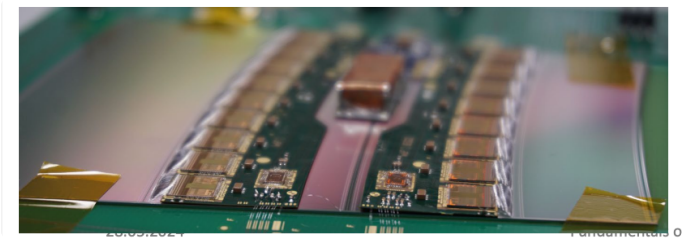

The transverse diffusion graph highlights how the particle track induces charge carriers that diffuse transversely, affecting adjacent strips. This diffusion impacts the spatial resolution and precision of the detector. The

hybrid design, with external readout electronics, allows for sophisticated data processing and analysis without compromising the sensor's structure.

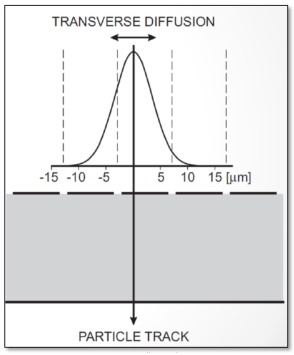

From Strips to Pixels

2D Information from Strip Detectors

To achieve two-dimensional spatial resolution using strip detectors, two detectors can be crossed orthogonally. This setup provides good spatial resolution in both directions. However, this method has limitations:

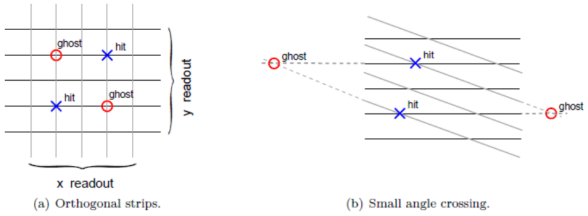

Quelle: Kolanoski, Wermes

1. **Orthogonal Strips:** The diagram on the left shows a setup with orthogonal strips. While it provides 2D information, it can also lead to "ghost" hits, which are false indications of particle interactions due to overlapping signals from different strips.
2. **Small Angle Crossing:** The diagram on the right illustrates a setup with strips crossing at a small angle. This configuration can also produce ghost hits and does not completely eliminate the problem.

Challenges with High Occupancy

At high occupancy, which refers to the number of hits per unit time and area, the limitations of strip detectors become more pronounced. The ghost hits and ambiguities in spatial resolution increase with higher hit rates, making it difficult to accurately determine particle trajectories.

Need for Real 2D Segmentation

To overcome these challenges, real 2D segmentation is required. This is where pixel detectors come into play. Pixel detectors provide true two-dimensional segmentation, allowing for precise spatial resolution without the ambiguities and limitations associated with strip detectors. Each pixel acts as an

independent detector, significantly reducing the likelihood of ghost hits and improving overall accuracy in high-occupancy environments.

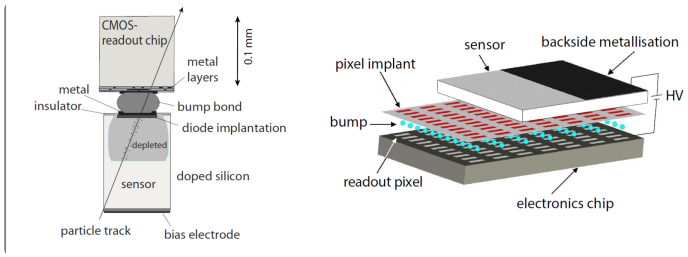

Sensor Tests

Quality Assurance (QA) Tests for Pixel and Strip Sensors

In series production, it is crucial to ensure that only working sensors are processed further due to the high costs involved. Therefore, rigorous QA tests are performed on pixel and strip sensors to verify their functionality.

IV Characteristic (Diode in Reverse Bias)

The primary method for testing these sensors involves measuring the current-voltage (IV) characteristic in reverse bias. This helps to identify any defects or inconsistencies in the sensor's performance. The process includes:

1. **Contact Setup:** Establishing contact between the unsegmented backside of the sensor and the strip/pixel side. This ensures that every single strip or pixel is individually connected and tested.
2. **Bias Grid:** Implementing a high ohmic short (bias grid) between all pixels to provide a single contact point. This setup helps in maintaining a consistent test environment and simplifies the connection process.

Components and Configuration

- **Bias Ring:** Encircles the sensor area to provide a stable reference voltage.
- **Poly Silicon Resistor:** Used in the bias grid to create a high-resistance path between the pixels.
- **Punch-Through Contact:** A specific type of contact that allows for reliable electrical connections between different layers of the sensor. This is depicted in the lower right section of the diagram, showing various stages of punch-through contact under different bias conditions.

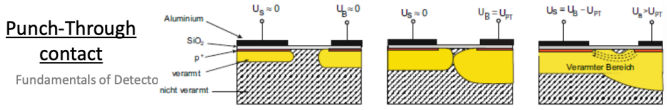

By implementing these QA tests, manufacturers can ensure the reliability and performance of pixel and strip sensors, crucial for their application in high-precision environments such as particle detectors.

Radiation Damage

Introduction

Radiation damage in semiconductor detectors can significantly impact their performance.

Types of Radiation Damage

1. Ionizing Damage

- **Mechanism:** Ionizing radiation (such as photons, electrons, and protons) deposits energy in the semiconductor material, creating electron-hole pairs.
- **Effects:**
  - **Trapped Charges:** Charges become trapped in the oxide layers or at the interfaces within the semiconductor, altering local electric fields.
  - **Ionizing Energy Loss (IEL):** This can lead to changes in the behavior of electronic components (e.g., transistors), affecting their threshold voltages and introducing parasitic currents.
  - **Single Event Effects (SEE):** These occur when a single ionizing particle disrupts the normal operation of electronic components, such as changing the state of a RAM cell, or causing damage to transistors and diodes.

2. Non-Ionizing Energy Loss (NIEL)

- **Mechanism:** High-energy particles (neutrons, protons) displace atoms from their lattice positions, creating defects.
- **Effects:**
  - **Point Defects:** Displaced atoms (primary knock-on atoms, PKAs) create point defects in the crystal structure.
  - **Cluster Defects:** High-energy PKAs can cause secondary displacements, leading to clusters of defects.
  - **Impact on Bulk Properties:** These defects introduce localized energy levels within the band gap, acting as traps that capture charge carriers, reducing signal efficiency.

Substrate Damage

- **Normalization:** Substrate damage from NIEL is often normalized to the damage caused by a 1 MeV neutron, using hardness factors and equivalent fluence.
- **Fluence Measurement:** Damage is measured in neutron equivalents per square centimeter (neq/cm²).

Process of Substrate Damage

- **Coulomb Scattering:** Charged particles scatter off silicon nuclei, transferring energy.
- **Elastic Scattering:** Neutrons scatter elastically, displacing silicon atoms.
- **Threshold Energy:** A minimum energy ($T > 25$ eV) is required to displace silicon atoms from the lattice.
- **Defect Mobility:** Defects can migrate within the crystal lattice, influenced by temperature. Controlled annealing can be beneficial initially but may become detrimental over time. Storing detectors at low temperatures ($<0^{\circ}C$) can help stabilize defects.

Main Effects of Radiation Damage

1. **Change in Effective Doping Concentration (Neff)**
   - **Additional Donor/Acceptor Levels:** Radiation creates new energy levels, altering the effective doping concentration.
   - **Change in Depletion Voltage:** This affects the voltage required to fully deplete the sensor.
   - **Type Inversion:** Over time, the majority carrier type can switch (e.g., from n-type to p-type), altering the sensor's characteristics.
   - **Reverse Annealing:** Post-irradiation, the properties of the sensor can degrade due to reverse annealing processes.
2. **Increase in Leakage Current (Ileak)**
   - **Higher Leakage Currents:** Radiation-induced defects increase leakage currents, leading to higher noise levels and power dissipation.
   - **Thermal Runaway:** If not adequately cooled, increased power dissipation can lead to thermal runaway, where the sensor overheats, further increasing leakage currents.
3. **Charge Trapping**
   - **Trap Centers:** Created by radiation damage, these centers capture electrons or holes, reducing the mean free path of charge carriers and the overall signal amplitude.

Mitigation Strategies for Radiation Damage

1. **Defect Engineering**
   - **Controlled Annealing:** Intentional annealing processes can help manage and reduce defects.
   - **Material Modification:** Increasing oxygen concentration in p-type silicon can reduce the impact of donor removal, enhancing the material's resistance to radiation damage.
2. **Device Engineering**
   - **Adjusting Doping Profiles:** Altering doping to prevent type inversion and allow partial depletion operation can improve resilience.
   - **Reducing Drift Distance:** Shorter drift distances reduce the impact of charge trapping, enhancing signal collection efficiency.
   - **Thin Sensors:** Thinner sensors help maintain high electric fields close to implant borders, reducing the effects of trapping and improving

performance.

Implications for Detector Operation

- **Change in Neff:** Requires adjusting bias voltage or accepting signal loss due to partial depletion.
- **Increased Ileak:** Necessitates improved cooling to prevent thermal runaway and manage noise.
- **Charge Trapping:** Needs careful design to minimize the drift path, ensuring that most charge carriers are collected before being trapped.

LT9

Active R&D on Semiconductor Detectors

The development of semiconductor detectors is highly application-specific, with tailored requirements for different fields such as high-energy physics, astronomy, and medical physics.

- **In high-energy physics**, detectors are essential for tasks like flavour tagging and low transverse momentum (pT) tracking. These applications demand detectors that are lightweight and can cover large areas. The specific requirements include achieving single-point spatial resolutions between 3 to 10 micrometers, time resolutions of less than 10 picoseconds, and maintaining low mass, specifically between 0.1 to 0.2% of the radiation length (X0) per layer.
- **Astronomy** applications for semiconductor detectors prioritize a wide spectral range and single-photon sensitivity. To meet these needs, detectors must have transparent surfaces, low dark count rates, and no insensitive gaps. These characteristics are vital for capturing faint astronomical signals with high fidelity and ensuring comprehensive coverage of the observed spectral range.
- For **medical physics**, detectors are used for ultra-high rate applications and spectral imaging. These applications require good energy resolution across a dynamic range to accurately differentiate between various energy levels. Additionally, the detectors must function without saturation or deadtime even at high charge rates, ensuring reliable and continuous operation during high-rate imaging processes.

Particle Physics Detectors

In the realm of particle physics, the requirements for detectors are meticulously defined to ensure precise and reliable measurements. These requirements are influenced by various factors, including the physics goals, the detector environment, and specific technical specifications.

Physics Goals:
Detectors are critical for several key physics measurements and processes. They are employed in flavour tagging and low transverse momentum (pT) tracking. They also play a role in vertex and jet charge determination, requiring precise momentum resolution and tracking efficiency. These detectors must also ensure effective track separation and minimize the chances of low pT fake track rejection. Furthermore, achieving a vertex resolution down to a few micrometers and maintaining a momentum resolution of approximately $\frac{\sigma_{pT}}{p_T^2} \approx 2 \times 10^{-5} \mathrm{GeV}^{-1}$ is essential for accurate data.

Environment Considerations:
The environment in which these detectors operate significantly influences their design and functionality. Bunch separation times range from 20 to 3000

ns.
Power pulsing is utilized at linear colliders but not at circular ones. Beamstrahlung, or beam-induced background, is a considerable factor for linear colliders but remains low for circular colliders. Detectors must also withstand significant radiation, requiring radiation hardness up to O(100 kRad/yr) and O(10^{11}) neq/yr.

Detector Requirements:
Detectors must have a large lever arm (large in radius), indicated by Rmin and Rmax, and provide comprehensive coverage with $|\cos\theta| < 0.99$ (or $\eta > 2.7$). This implies the need for a large area, such as the Silicon Wrapper at IDEA, which covers approximately 90 m^2.

For spatial resolution, a single-point resolution of around 3 µm for vertex detectors and about 10 µm for tracking detectors is required. In terms of timing, detectors should achieve a time resolution of about 1 ns, with some layers needing to be even more precise, such as the TOF (Time-of-Flight) layer, which requires less than 100 ps.

The goal is to maintain a **low mass**, around 0.1 to 0.2% X_0 per layer, including additional contributions from the beam pipe, which is around 0.14% X0 at the International Linear Collider (ILC) or 0.3% X0 at the Future Circular Collider (FCC).

Gas flow cooling is typically used to manage heat. Low power consumption is also critical, with a target of less than 50 mW/cm^2. Additionally, services associated with low mass, such as power distribution and data rate, are essential, with innovations like silicon photonics being considered for data management.

The development of semiconductor detectors encompasses several key areas, each with specific topics that need to be addressed. Despite the diversity of detector concepts, all designs integrate different types of silicon detectors, such as

- vertex detectors,
- tracking detectors,
- Time-of-Flight (TOF) layers for particle ID.

Development Strategies:
The development of these detectors can be divided into two main strategies:

1. **Extremely High Performance:**
   This approach focuses on improving spatial and temporal resolution. Achieving a single-point spatial resolution of less than or equal to 3 micrometers is a significant challenge today. Additionally, achieving

precise timing at small radii, with a target on the order of 1 picosecond, presents another layer of complexity.

2. **High Performance for Large Areas:**
   This strategy aims to reduce the cost per unit area while maintaining high performance. For detectors that cover larger areas, lower hit densities and longer TOF at large radii are critical factors. These considerations are essential for ensuring that the detectors can be produced cost-effectively while still meeting performance requirements.

State-of-the-Art by Requirement

1. State-of-the-Art by Requirement : Spatial Resolution

Spatial Resolution in Detector Layers

The spatial resolution in each layer of a semiconductor detector is influenced by several key factors.

Pixel Pitch:
The pixel pitch, which is the distance between the centers of adjacent pixels, significantly affects spatial resolution. Most current prototypes have a pixel pitch ranging from 10 to 35 micrometers. However, there is a conflict between reducing pixel pitch and maintaining in-pixel functionality, as smaller pixels may not accommodate all necessary electronic components.

Charge Deposition and Sensitive Layer Thickness:
The thickness of the sensitive layer where charge is deposited also plays a critical role. For instance, the epitaxial (epi) layer typically has a thickness of about 10 micrometers, while DMAPS (Depleted Monolithic Active Pixel Sensors) have a thickness of around 50 micrometers. These thicknesses determine how well the detector can capture and measure incoming particles.

Charge Sharing:
Charge sharing refers to the distribution of charge across multiple pixels when a particle is detected. The width of the charge cloud compared to the pixel pitch determines the extent of charge sharing. Without noise, the resolution (σ) is expected to be at least half of the pixel pitch ($\sigma \geq p/2$). Effective charge sharing can improve spatial resolution but requires careful calibration and optimization.

Charge Encoding:
The number of Analog-to-Digital Converter (ADC) bits used for charge encoding influences the precision with which the charge is measured. Higher ADC resolution allows for more precise charge measurements, contributing to better spatial resolution.

Graphs and Data:

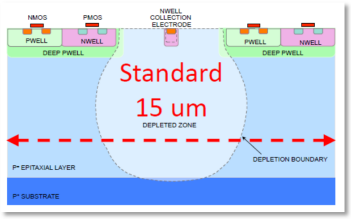

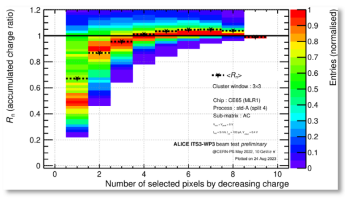

ness

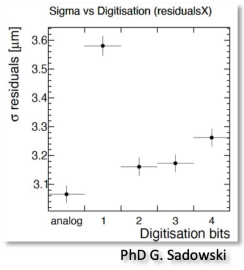

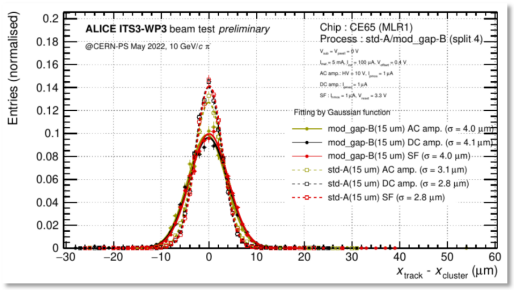

- The graph depicting pixel pitch versus spatial resolution highlights the trade-offs between pixel size and functional integration.
- Charge deposition diagrams show the structure of sensitive layers and their impact on detection efficiency.
- Charge sharing plots compare the charge cloud width to pixel pitch, indicating the importance of balancing these parameters.
- Charge encoding data demonstrates the relationship between ADC bit resolution and spatial precision, underscoring the need for high-resolution encoding.

Overall

➔ σ_{sp} ~ 3 µm seems achievable

---

2. State-of-the-Art by Requirement: Timing Resolution

Applications:

1. **TOF Particle Identification:**
   - Precise time measurements help differentiate particles based on their speed.
2. **Pile-Up Suppression:**
   - High timing resolution can distinguish between overlapping events that occur within a short time window.
3. **Tracking Pattern Recognition and Shower Analysis:**
   - Accurate timing helps in reconstructing the trajectories of particles and analyzing particle showers.
4. **Physics of Long-Lived Particles:**
   - Detecting particles with long lifetimes requires precise timing to measure their decay accurately.

Overall the ATLAS High-Granularity Timing Detector (HGTD) and other similar technologies have demonstrated a total timing resolution

$$\sigma_{total} \sim 35 \text{ ps demonstrated by ATLAS HGTD and others}$$

Research and Development Directions:

1. **Low-Gain Avalanche Diodes (LGADs):**
   - **Resistive Silicon Detectors:** These detectors feature a continuous gain layer and charge collection through a resistive n-layer, enhancing timing resolution.
   - **Variants of LGADs:**
     - **AC-LGAD (AC coupled LGAD):** Features an AC coupling electrode for improved signal readout.
     - **DJ-LGAD (Double Junction LGAD):** Incorporates a double junction to enhance performance.
     - **TI-LGAD (Trench Isolated LGAD):** Uses trench isolation to reduce charge sharing and improve timing.
     - **iLGAD (Inverse LGAD):** Employs an inverse structure for better charge collection efficiency.
2. **Hybrid 3D Silicon Detectors:**
3. **CMOS Detectors with Gain Layer:**

Example of Timing detector: LGAD

Low-Gain Avalanche Diodes (LGADs) are specialized semiconductor devices designed to achieve fast signal detection with moderate signal gain. The key features and operational principles of LGADs are outlined below:

High Electric Field (E-Field) Close to Readout Electrode:

- **Moderate Signal Gain:** The high E-field near the readout electrode ensures that the incoming charge carriers are rapidly accelerated, leading to a moderate gain in the signal without significantly increasing noise.
- **Short Drift Distance:** Charge carriers travel a short distance before reaching the readout electrode, minimizing the time they spend in the detector and thereby improving the timing resolution.
- **Fast Detector Signal:** The combination of moderate gain and short drift distance results in a fast response time, making LGADs suitable for applications requiring precise timing measurements.

Crucial Role of Fast Readout Electronics:

- **Time Walk:** Variations in the signal's arrival time can affect the accuracy of timing measurements. Fast readout electronics help mitigate these variations.
- **Jitter:** Jitter refers to the random variations in the timing of the signal. Reducing jitter is essential for maintaining high timing

resolution.

- **Time-to-Digital Converter (TDC) Resolution:** The resolution of the TDC is critical for accurately digitizing the timing information. Fast readout electronics enhance TDC performance.

Impact of High Gain:

- **Noise:** High gain increases the amplitude of the signal but also amplifies noise, which can degrade the overall signal quality.
- **Jitter:** Higher gain can lead to increased jitter, affecting the precision of the timing measurements.
- **Power Consumption:** Devices with high gain, such as Avalanche Photodiodes (APDs) and Silicon Photomultipliers (SiPMs), consume more power, which can be a limiting factor in some applications.

Diagram

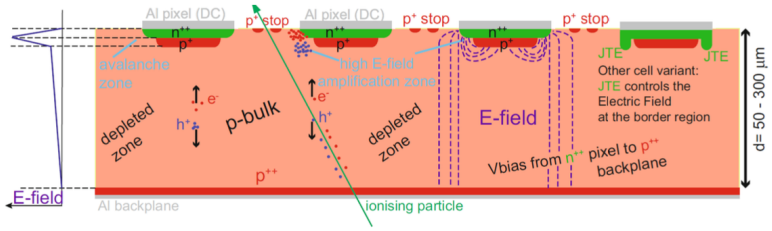

The diagram provided illustrates the structure and operation of an LGAD. Key components and regions include:

- **Avalanche Zone:** This is where the initial charge multiplication occurs due to the high E-field, leading to moderate signal gain.
- **Depleted Zone:** The region where charge carriers are collected and drift towards the readout electrode.
- **Readout Electrode:** Typically an aluminum (Al) pixel with a p-stop to prevent lateral spreading of the charge.
- **Junction Termination Extension (JTE):** A feature used to control the E-field at the edges of the detector cell, ensuring uniform performance across the detector area.

Example of Timing detector: 3D Silicon Sensors

Planar Geometry in Semiconductor Detectors
The planar geometry is considered the most "natural" for semiconductor detectors, primarily because of its straightforward design and fabrication process. However, this configuration faces several challenges, particularly after irradiation.

Below is a detailed explanation of the issues and possible solutions associated with planar geometry detectors.

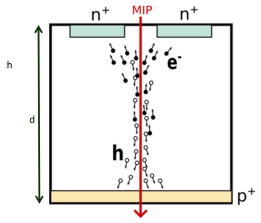

Electrodes on the Sensor Surfaces:
In planar detectors, electrodes are placed on the surfaces of the sensor. This design means that charge carriers generated by incident particles must drift through the entire bulk of the sensor before reaching the collecting electrodes. The typical drift distance ranges from 150 to 250 micrometers.

Challenges Post-Irradiation:
After irradiation, semiconductor materials can develop defects that trap charge carriers. These traps prevent charge carriers from reaching the electrodes, leading to a reduction in signal amplitude and, consequently, a decrease in hit efficiency.

Hit Efficiency:
Hit efficiency ϵ_{hit} is defined as the ratio of detected particles to all incident particles. Trapping of charge carriers adversely affects this ratio, as trapped charges do not contribute to the detected signal.

Trapping Probability:
The probability of trapping is quantified by the mean free path ((\tau)) of the charge carriers.

If the mean free path is less than the drift distance ((d)), there is a significant likelihood that charge carriers will be trapped before they reach the electrodes.

Solutions to Improve Performance:

1. **Increase Mean Free Path ((\tau)):**
    - Fewer Traps,Different Materials,Increased Electric Field.
2. **Reduce Drift Distance (d):**
    - **3D Geometry of Electrodes:** Implementing a 3D structure for electrodes can significantly shorten the drift distance.

Diagram Explanation:

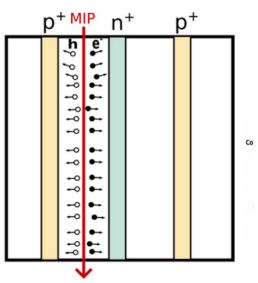

The provided diagram illustrates the concept of planar geometry and the movement of charge carriers:

- **Electrodes (n+ and p+):** Positioned on the sensor surface.
- **Depleted Zone:** The region where charge carriers (electrons (e^-) and holes (h^+)) are generated and drift towards the electrodes.
- **MIP (Minimum Ionizing Particle):** Represents the incident particle that generates electron-hole pairs as it traverses the sensor.

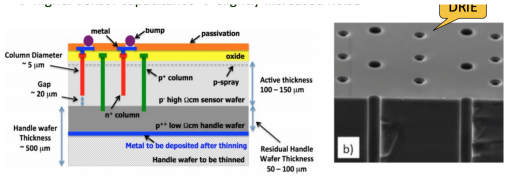

3. State-of-the-Art by Requirement: Large Area Semiconductor Detectors

These detectors prioritize **high yield** and production capacity at the vendor level and during module assembly. The focus is on **affordable cost, efficient connections, and robust services.**

Key Requirements and Strategies:

1. **High Yield and Production Capacity:**
   - Ensuring that the production process can consistently produce large numbers of functional detectors.
   - The goal is to keep costs manageable while maximizing the number of usable detectors produced from each batch.
2. **Cost-Effective and Efficient Connections and Services:**
   - Streamlining the production process to reduce costs.
   - Ensuring that connections (such as interconnects between wafers) and services (like power distribution and signal readout) are reliable and efficient.

Reducing Production Costs for "Classic Size" Sensors:

1. **Hybrid Passive CMOS Sensors (Pixel & Strip):**
   - Combining different types of sensors (pixel and strip) to optimize production and interconnection processes.
   - Techniques like wafer-to-wafer bonding can improve integration and performance.
2. **Monolithic Active CMOS Strip Sensors:**
   - Using monolithic designs where the sensor and readout electronics are integrated into a single silicon piece.
   - This approach can simplify production and reduce overall costs.

Wafer Scale Sensors:

1. **Stitching and Bent Sensors (ALICE ITS-3):**

- Employing stitching techniques to create larger sensors from smaller segments.

2. **Post-Process Redistribution Layer (RDL):**
   - Using post-processing techniques to add an additional layer for connections, as seen in the Belle II iVTX Upgrade.

Diagrams and Images:
The provided diagrams and images illustrate various aspects of large area sensor production:

1. **Wafer Scale Production:**
   - Images of full wafers with multiple sensors fabricated on them.
   - The large wafers demonstrate the scale of production and the ability to produce multiple sensors simultaneously, improving yield and reducing costs.

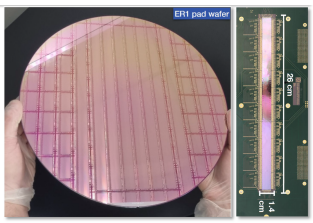

2. **Sensor Modules:**
   - Photos of sensor modules that have been assembled using the described techniques.
   - These modules highlight the practical application of large area sensors in high-energy physics experiments and other fields requiring extensive coverage.

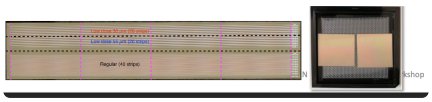

4.State-of-the-Art by Requirement: Power Consumption

Some of the prototypes reach ~100 mW/cm²
• MIMOSIS reports 40 - 70 mW/cm², ATLASPix3.1 ~ 175 mW/cm²
• others estimate 10 - 50 mW/cm²

Max allowable power density not very clear
• Mu3e (He cooling) reports ΔT ≤ 50 K detector temp wrt gas inlet temp for a heat dissipation of 350 mW/cm²

-> limit not clear, but: the lower, the better
-> need engineering support
-> thermal simulation crucial

0:00 / 1:32:17

LT10

Calorimeters

The primary task of a calorimeter is to measure the energy of incident particles. This can be achieved through two main methods:

1. **Tracking Detector:** Measures the momentum of charged particles and derives particle mass from identification processes, using the relation $E^2 = p^2c^2 + m^2c^4$. This method faces challenges as it can only track charged particles, requires a large volume tracker, and experiences increasing relative uncertainty with higher momentum.
2. **Calorimeter:** This method involves the complete absorption of a particle's energy within the detector to measure it accurately.

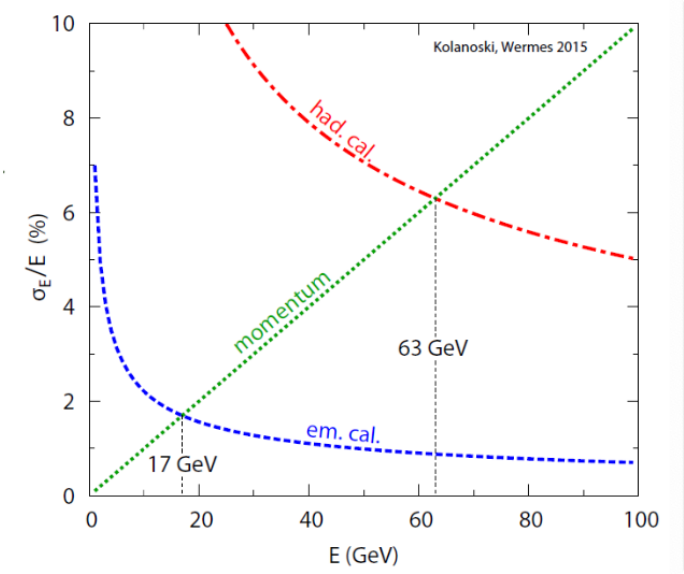

1. Electromagnetic Showers

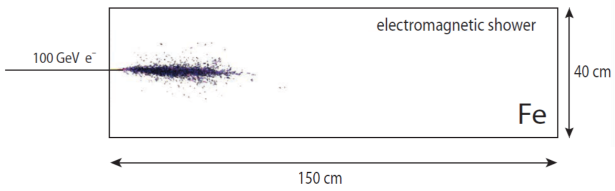

High-energy electrons, positrons, and photons induce electromagnetic showers primarily through bremsstrahlung and pair production processes.

- **Bremsstrahlung and Pair Production:** In high-Z (high atomic number) materials like lead, tungsten, or uranium, these processes dominate.

→ bremsstrahlung & pair production

(a) Bremsstrahlung. (b) Pair production.

Rossi's Shower Evolution Model (1952):

a. Only Bremsstrahlung and Pair Production Taken into Account

- The model considers only two primary processes: bremsstrahlung and pair production.
- These processes dominate in high-Z materials.

b. Energy Loss via Ionization

- The rate of energy loss by ionization is given by $\left.\frac{dE}{dx}\right|_{\text{ion}} \approx \frac{E_k}{X_0}$.
- $\left.\frac{dE}{dx}\right|_{\text{ion}}$ represents the energy loss per unit length due to ionization.
- E_k is the kinetic energy of the particle.
- X_0 is the radiation length, indicating the distance over which a high-energy electron or photon reduces its energy significantly.

c. Neglect Multiple Coulomb Scattering, Only Longitudinal Shower Development

- The model assumes that multiple Coulomb scattering (small-angle deflections) is negligible.
- It focuses on the longitudinal development of the shower, ignoring transverse scattering effects.
- This simplifies the analysis and predictions about the shower's energy deposition along its path.

1. Longitudinal Shower Development

The Rossi Model details that as long as the particle's energy exceeds the critical energy (E > E_crit), energy loss occurs predominantly through ionization. Each interaction occurs per radiation length (X0), with energy distributed among secondary particles, effectively halving the energy per radiation length.

For a calorimeter:

- Most energy is deposited within a thickness of about 25 X0.
- Examples include the ATLAS ECAL with a thickness of approximately 45cm and the CMS ECAL with around 23cm.

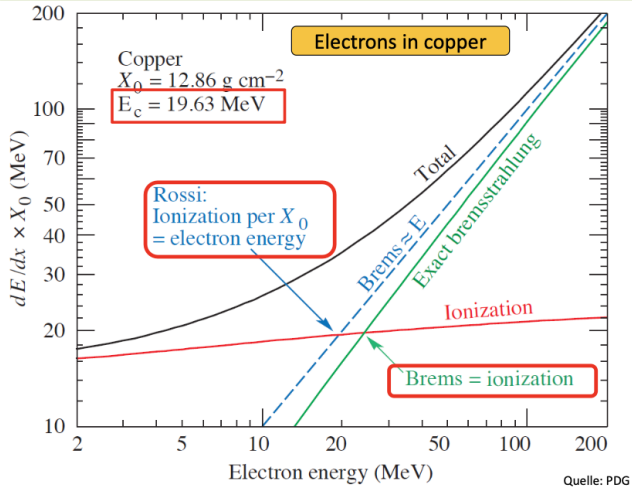

Figure 33.13: Two definitions of the critical energy E_c.

Characteristics of Elm. Showers

Bremsstrahlung and Pair Production:

- The cross-section σ for these processes is proportional to (Z^2), where (Z) is the atomic number of the material.
- High-Z passive materials like lead, tungsten, and uranium are commonly used in detectors due to their effectiveness in inducing bremsstrahlung and pair production.

Emission of Particles in Forward Direction:

- The emission angle $((\theta))$ for bremsstrahlung is inversely proportional to the particle's energy (E), given by $\theta \propto \frac{1}{\gamma} = \frac{m_e}{E}$.

Length Scale for Both Processes: Radiation Length ((X_0)):

- Radiation length is a critical scale for both photons and electrons. It represents the mean distance over which a high-energy electron loses all but $(1/e)$ of its energy or a high-energy photon reduces its energy by a factor of (1/e).
- The radiation length X_0 is inversely proportional to Z^2:

$$X_0 \propto \frac{1}{Z^2}$$

Characteristics of Radiation Length:

- **Photons:** The mean free path with respect to pair production is

$$\lambda \approx \frac{9}{7} X_0$$

- **Electrons:** The energy loss per unit length is described by

$$\frac{dE}{E} = \frac{dx}{X_0}$$

Material Properties Table:

Material	Z	Dichte (g/cm^3)	X_0 (g/cm^2)	X_0 (cm)	E_k (MeV)	E_k^μ (GeV)
Be	4	1.85	65.19	35.3	113.7	1328
C (Graphit)	6	2.21	42.65	19.3	81.7	1060
Al	13	2.70	24.01	8.9	42.7	612
Si	14	2.33	21.82	9.36	40.2	582
Fe	26	7.87	13.84	1.76	21.7	347
Cu	29	8.96	12.86	1.43	19.4	317
Ge	32	5.32	12.25	2.30	18.2	297
W	74	19.30	6.76	0.35	8.0	150
Pb	82	11.35	6.37	0.56	7.4	141
U	92	18.95	6.00	0.32	6.7	128
Szintillatoren:						
NaI	11, 53	3.66	9.49	2.59	13.4	228
CsI	55, 53	4.53	8.39	1.85	11.2	198
BaF_2	56, 9	4.89	9.91	2.03	13.8	233
$PbWO_4$	82, 74, 8	8.30	7.39	0.89	9.64	170
Polystyrol	1, 6	1.06	43.79	41.3	93.1	1183

- The table includes various materials with their atomic number ((Z)), density (g/cm³), and radiation length ((X_0)) both in g/cm² and cm.
- High-Z materials like lead (Pb), tungsten (W), and uranium (U) have shorter radiation lengths, making them effective for inducing showers.
- Scintillators and other materials have their specific radiation lengths listed, indicating their suitability for different types of detectors.

ROSSI MODEL

- The model focuses on bremsstrahlung and pair production processes as long as the particle's energy E is greater than the critical energy E_{crit}
- Energy loss due to ionization is considered once $E \leq E_{\text{crit}}$

Key Points:

1. **One Interaction per Radiation Length X_0:**
   - Particles undergo one significant interaction per radiation length.
2. **Energy Distribution Amongst Secondaries:**
   - The energy of the particle is cut in half after each radiation length, distributing the energy equally among secondary particles.
   - This results in the energy per particle being reduced by half for each X_0

Implications for Secondary Particles:

- **Total Number of Secondary Particles:**
  - $N_{\text{tot}} \approx \frac{E_0}{E_{\text{crit}}}$, where E_0 is the initial energy of the incident particle.
- **Total Track Length Inside Calorimeter:**
  - Total track length inside calorimeter $s_{\text{tot}} \approx \frac{E_0}{E_{\text{crit}}} \cdot X_0$.

Both the total number of secondary particles and the total track length inside the calorimeter are proportional to the initial energy E_0 of the incident particle.

- At Depth $s = t \cdot X_0$ we find a Number of Secondary Particles $N_{\text{sec.}} = 2^t$ and Average Energy of Secondary Particles $\overline{E}_{\text{sec.}} = \frac{E_0}{2^t}$

Illustration:

The diagram shows the energy reduction and multiplication of particles through successive radiation lengths. Starting from an initial energy E_0 , the energy is cut in half (to $\frac{E_0}{2}$, $\frac{E_0}{4}$, $\frac{E_0}{8}$, etc.) with each radiation length X_0

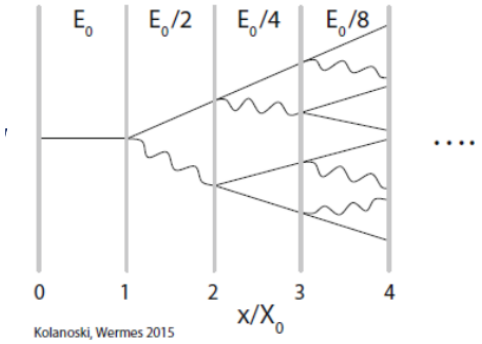

How deep (in units of X0) should the calorimeter be?

Rossi Model: Once $E < E_{crit}$, particles will be stopped after one more X0

At which depth $E \approx E_{crit}$?

$$E_{sec} = E_{crtitic} = \frac{E_0}{2^{t_{MAX}}} \quad \rightarrow \quad t_{MAX} = \frac{ln(E_0/E_{critic})}{ln(2)}$$

- Depth of shower maximum depends on ln E0 -> Calorimeter is a very compact device!
- 98% of energy deposited within typical thickness of a calorimeter ~25 X0

Examples: ATLAS ECAL t ≈ 45cm for X0 = 1,8cm; CMS ECAL t ≈ 23cm for X0 = 0,9cm

---

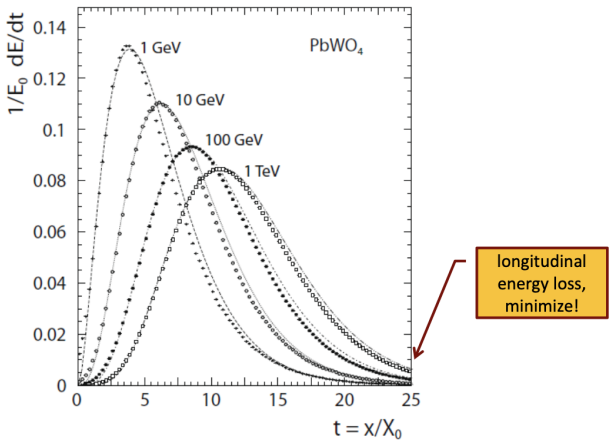

The graph illustrates the longitudinal energy deposition of electromagnetic showers in PbWO4, emphasizing the need for sufficient calorimeter depth and

the importance of minimizing longitudinal energy loss to ensure precise energy measurements.

- **Depth Optimization:** Calorimeters must be designed with sufficient depth (in units of X_0) to capture the full energy deposition of high-energy particles. For example, a depth of around 25 X_0 ensures most of the energy is measured, even for high-energy incident particles like 1 TeV.
- **Material Choice:** PbWO4 is used due to its appropriate radiation length and effective stopping power for high-energy particles.
- **Resolution Enhancement:** By understanding the energy deposition profile, calorimeters can be fine-tuned to improve energy resolution and ensure that the majority of the particle's energy is captured within the optimal range.

---

2. Transversal Shower Development

The lateral development of the shower is dominated by multiple Coulomb scattering, with the characteristic dimension being the Moliere radius (RM). This radius determines the lateral segmentation of the calorimeter, usually on the order of centimeters.

Hadronic Showers

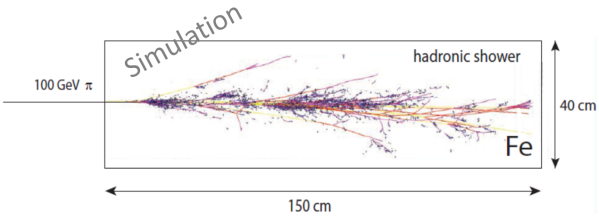

Hadronic showers are more complex, involving high-energy interactions with target nuclei, resulting in secondary particle cascades and subsequent nuclear de-excitation processes such as spallation and evaporation. These showers exhibit larger fluctuations compared to electromagnetic showers and are characterized by the nuclear absorption length.

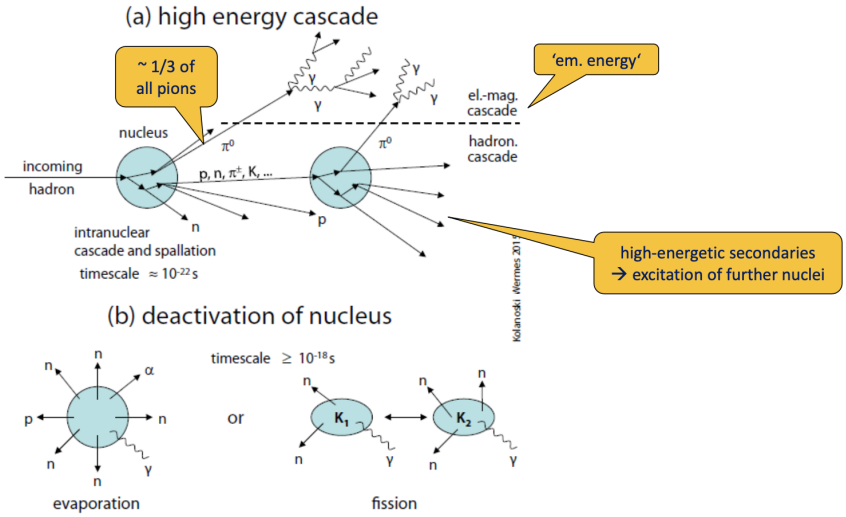

1. High-Energetic Cascade

- **Initial Interaction:** Incident hadrons (protons, neutrons, pions, etc.) undergo inelastic interactions with target nuclei.
- **Secondary Particles:** These interactions produce high-energetic secondary particles, primarily in the forward direction.
- **Cascade Formation:** The secondary particles further interact with other target nuclei, creating a cascade of particles.
- **Diagram Explanation:** The diagram shows an incoming hadron hitting a nucleus, leading to an intranuclear cascade and spallation, and subsequent emission of secondary particles such as pions π^0, π^+, π^-, neutrons n, and protons p

2. Spallation and Intra-Nuclear Cascade

- **Excited Nucleus:** The high-energy interactions create a highly excited nucleus.
- **De-Excitation:** The excited nucleus de-excites by emitting nucleons (protons and neutrons) and light nuclei.
- **Kinetic Energy of Secondaries:** The emitted secondary particles typically have kinetic energies on the order of 100 MeV.
- **Time Scale:** These processes occur over a very short time scale, approximately (10^{-22}) seconds.
- **Neutron-to-Proton Ratio:** The number of neutrons emitted is roughly 1.5 times the number of protons.

3. Evaporation

- **Residual Excitation:** After spallation, the nucleus remains excited, albeit at a lower energy level.
- **Nucleon Evaporation:** The excited nucleus further de-excites by "evaporating" nucleons, which can also lead to fission.
- **Kinetic Energy of Evaporated Particles:** The kinetic energy of these particles is typically around 1 MeV.

- **Time Scale:** The evaporation process occurs over a longer time scale compared to spallation, approximately (10^{-18}) seconds.
- **Neutron-to-Proton Ratio:** The ratio of emitted neutrons to protons depends on the neutron-to-proton ratio (N/Z) of the parent nucleus and the Coulomb barrier.

Energy Resolution

The resolution of a calorimeter's energy measurement depends on several terms:

1. **Stochastic Term:** Related to the Poisson statistics of the secondary particle count.

$$\Rightarrow \frac{\sigma_E^{stat.}}{E} \propto \frac{\sqrt{N_S}}{N_S} = \frac{1}{\sqrt{N_S}} \propto \frac{1}{\sqrt{E}}$$

2. **Noise Term:** Fluctuations in the signal that are independent of the signal's amplitude.

$$\Rightarrow \frac{\sigma_E^{\text{noise}}}{E} \propto \frac{1}{E}$$

3. **Constant Term:** Systematic errors such as miscalibration or inefficient cells. The combination of these factors affects the overall energy resolution, with relative uncertainty decreasing as energy increases.

$$\Rightarrow \frac{\sigma_E^{\text{const}}}{E} = \text{const.}$$

   Considering the combination:

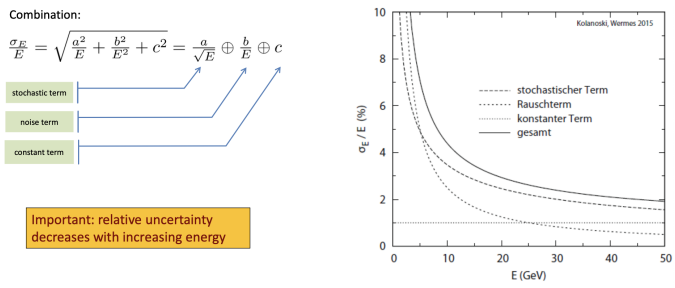

Energy Calibration

Calibrating the calorimeter involves several methods:

- **Beam Tests:** Utilizing well-known energy depositions.

- **Process Reconstruction**: Using known processes like reconstructing π0 masses from gamma pairs or resonant masses from electron-positron pairs during data collection.
- **Radioactive Sources**: Using gamma lines for continuous calibration.

Calorimeter Concepts and Layouts

Calorimeters can be homogeneous or sampling types:

1. **Homogeneous Calorimeters**: Use the same material for both absorption and detection (e.g., crystal scintillators, liquid noble gases). They offer the best energy resolution but are expensive and mainly used for electromagnetic calorimeters (*ECALs*).
2. **Sampling Calorimeters**: Combine high-Z absorbers with active detection mediums like scintillators or ionization media. These are cost-effective, compact, and radiation-hard, making them suitable for hadronic calorimeters (*HCALs*).

Examples of Calorimeters

- **CMS ECAL**: Uses radiation-hard lead tungstate (PbWO4) crystals for precise energy measurements, especially in high radiation environments.

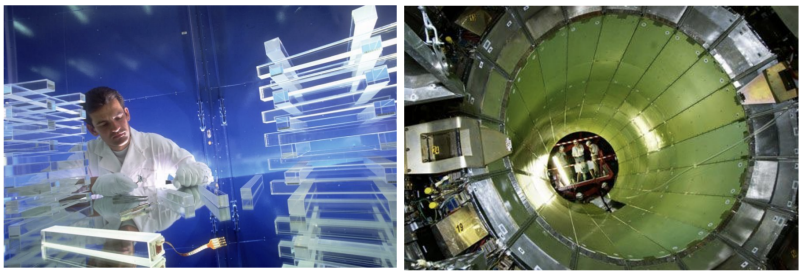

CERN, LHC, 2009 - now
- radiation hard $PbWO_4$, specially developed for CMS
- homogeneous calorimeter uncommon (best energy resolution for H→ γγ)
- equivalent noise energy 120MeV (CsI(Tl) around 250keV), appropriate for this energy range

- **ATLAS ECAL**: Utilizes a sampling calorimeter design with liquid argon and an 'accordion' geometry to avoid insensitive areas.

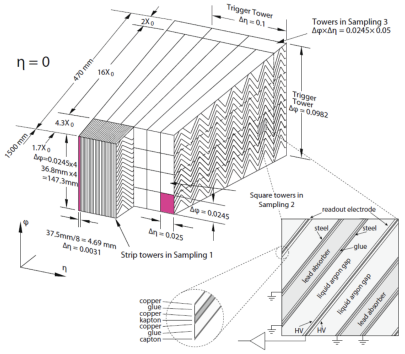

CERN, LHC, 2009 - now
Sampling calo, LArg, ‚accordion' geometry
→ no insensitive areas in Phi
→ longer ionization length

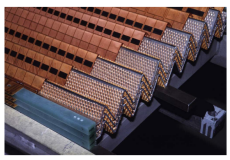

- **ATLAS TileCal**: An example of a hadronic calorimeter within the ATLAS detector at CERN, employing a tile design for effective sampling.

Atmosphere as a Calorimeter

High-energy cosmic rays and gammas interacting with the atmosphere develop electromagnetic or hadronic showers, similar to those observed in laboratory calorimeters. Detectors like the Auger Experiment in Argentina measure these atmospheric showers to study cosmic rays.

Longitudinal and Transversal Segmentation

Longitudinal Segmentation: Ensures accurate energy measurements by compensating for energy lost in materials preceding the calorimeter. Methods include:

- **Tail Catcher:** Corrects energy measurements by catching residual energy.
- **Presampler:** Detects if a shower has already begun before reaching the calorimeter, allowing for corrective measures.

Transversal Segmentation: Maintains accuracy by segmenting the calorimeter laterally, typically in units of the Moliere radius, to manage shower spread and improve resolution.

Compensation Techniques

Due to the mixed electromagnetic and hadronic components in hadronic showers, compensation is necessary:

1. **Hardware Compensation:** Involves designing calorimeters to balance the response to electromagnetic and hadronic components by adjusting the sampling fraction or using materials that enhance specific reactions.
2. **Software Compensation:** Uses algorithms like particle flow to correct for discrepancies during data analysis, improving overall energy measurement accuracy.

LT11

Scintillators and Photodetectors

How to Instrument a Cubic Kilometer of Ice with PMTs

A history of Neutrino Astronomy in Antartica

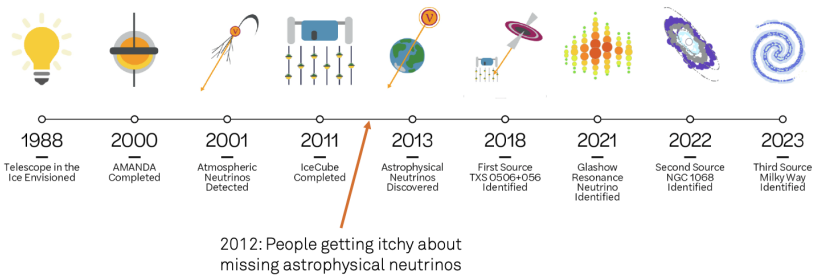

How many neutrinos does the IceCube Detect?

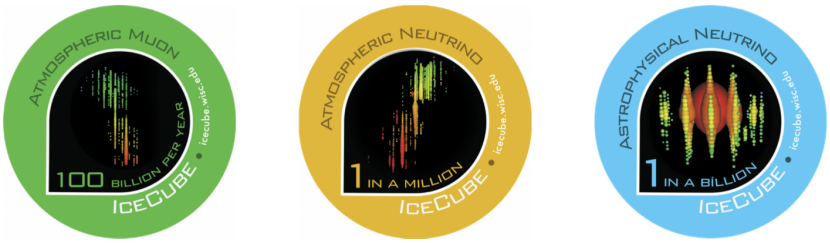

Neutrino Detection with IceCube

Neutrino detection is a global effort, with various telescopes located around the world, each targeting different energy regimes but utilizing similar technology. The detection principle for these neutrinos involves the use of Cherenkov radiation.

The IceCube Neutrino Observatory, situated at the South Pole, plays an important role in this.

IceCube Events

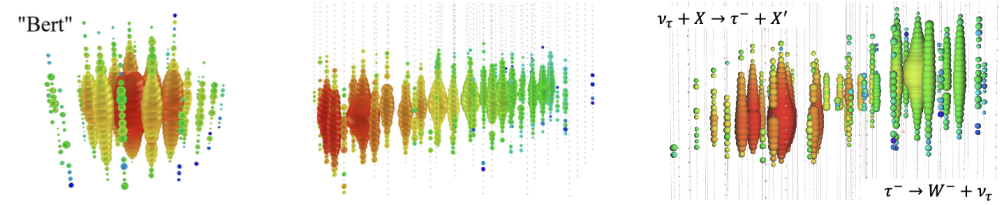

Cascade like events:

- ν_e - CC and all flavour NC interactions
- Interaction inside instrumented volume
- Poor angular resolution ≈ 5°
- Good energy resolution

Track like events:

- ν_μ - CC interactions
- Interaction may happen outside instrumented volume
- Good angular resolution ≈ 1°
- Poor energy resolution

Double Cascades:

- ν_τ interactions
- Very distinct and background free signature
- Very hard to detect!

12

The DOM: IceCube's Fundamental Unit

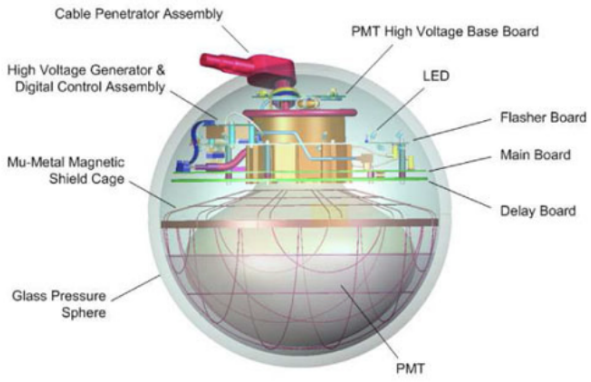

The Digital Optical Module (DOM) is the fundamental unit of IceCube. Each DOM includes a downward-facing 10-inch PMT (Hamamatsu R7081-02) with a 25% peak quantum efficiency. It houses a high voltage supply, electronics, and flasher LEDs. For DeepCore, a specialized section of IceCube, the DOMs use PMTs with a higher quantum efficiency of 34% (Hamamatsu R7081MOD). Despite the complex deployment process, the failure rate of DOMs is very low, with most issues occurring during deployment.

Beyond IceCube: Multi-PMT-DOMs

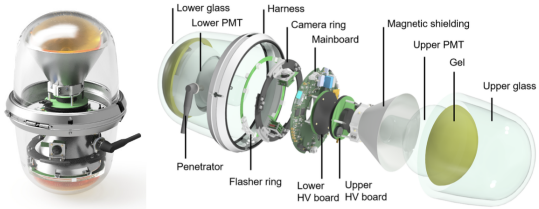

The D-Egg module represents the next step in neutrino detection technology, designed and built for the IceCube upgrade. The D-Egg features UV-transparent glass housing and various internal components, including mainboards, calibration devices, PMTs, and optical coupling silicone. The PMTs in the D-Egg have a higher dark rate due to their higher quantum efficiency. The pressure vessel of the D-Egg has been rigorously tested to withstand up to 72 MPa, ensuring its durability during deployment and operation.

IceCube Reconstruction Algorithms

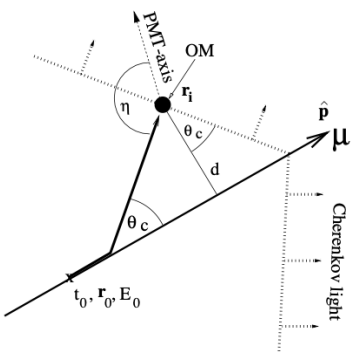

Reconstructing the paths and interactions of detected neutrinos involves algorithms. The reconstruction process can be generalized to estimating unknown parameters based on experimentally measured values, using a maximum likelihood method. For instance, Cherenkov light fronts are simplified to a single muon track forming a cone, described by parameters like position, time, direction, and energy. The reconstruction process involves three levels: analyzing simple features such as total charge, applying simple fits assuming straight lines, and using likelihood-based reconstructions.

-> Details are not super important: Reconstruction is based on the position of the DOMS and the arrival time of Cherenkov photons.

The Role of South Pole Ice

The unique properties of South Pole ice make it an effective medium for neutrino detection, particularly in terms of absorption and scattering of photons. The ice allows for detailed studies using flashers and receiving sensors to measure photon propagation, aiding in the calibration and optimization of the detection system.

- Impurities in the ice make the process challenging but thos impurities are being studied

---

Properties of Photomultiplier Tubes (PMTs)

- basic design of a photomultiplier

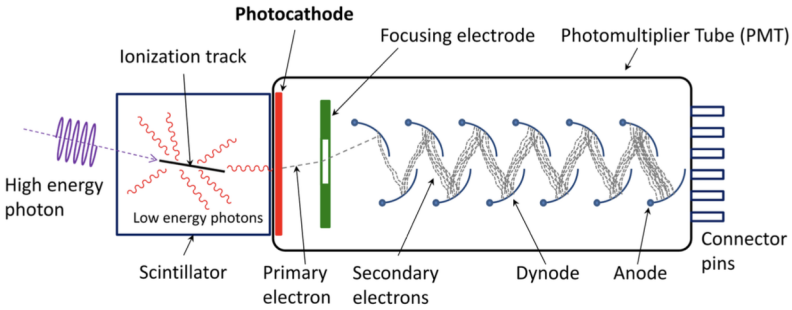

- PMT converts high-energy photons into an electrical signal through a process of photon absorption, electron emission, and electron multiplication.
- The initial high-energy photon creates a burst of low-energy photons in the scintillator. These low-energy photons then release primary electrons from the photocathode.
- These primary electrons are amplified through multiple stages of dynodes before being collected at the anode and transmitted as a strong electrical signal through the connector pins.

PMTs for Super-Kamiokande are 20“ (51 cm) in diameter.

21

PMTs are characterized by high gain, typically greater than (10^6), and low noise, making them capable of detecting *single photons*. They offer good timing resolution, better than 200 picoseconds, and have a typical quantum efficiency of around 25%. These tubes are commercially available for various applications, although they are not particularly portable. For example, the PMTs used in the Super-Kamiokande experiment have a diameter of 20 inches.

The Photoelectric Effect

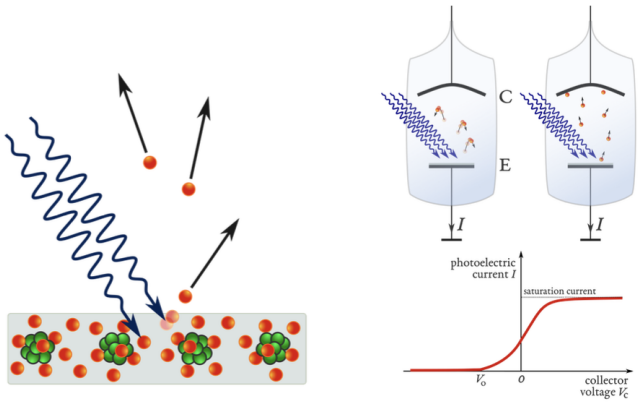

The photoelectric effect is central to the operation of PMTs.

- **Photon Absorption:** When a photon with sufficient energy strikes a material, it can transfer its energy to an electron within that material.
- **Electron Emission:** If the photon's energy is greater than the material's work function (the energy needed to liberate an electron), the electron is emitted from the surface of the material.

Photon Detection: The PMT begins with a photocathode, a material coated on the inner surface of the tube that is sensitive to light. When incident photons strike the photocathode, they cause the emission of photoelectrons via the photoelectric effect.

Photocathodes, often made from bi-alkali or multi-alkali compounds such as SbCs, SbKCs, and SbNaKCs, efficiently absorb photons and emit electrons. This process is critical for the initial detection of photons in PMTs.

Voltage Divider and Quantum Efficiency

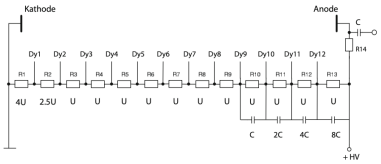

The voltage divider in PMTs generates the necessary potential gradients at the dynodes, typically using a high voltage of 1.8 kV. Quantum efficiency, the measure of signal yield per incoming photon, is wavelength-dependent, with typical values ranging from 25% to 40%.

PMT Window Types

PMTs can have different window types depending on their application. End window PMTs usually have a borosilicate glass envelope with a wavelength threshold of approximately 300 nm. For extended UV range, UV-borosilicate glass (185 nm) or quartz glass (150 nm) can be used. Side window PMTs, on the other hand, are often used in applications requiring close packing, like gamma cameras.

Dynode Geometry and Skipping

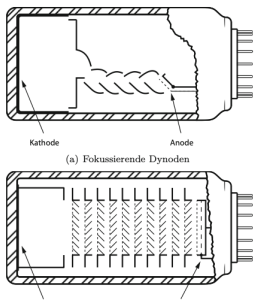

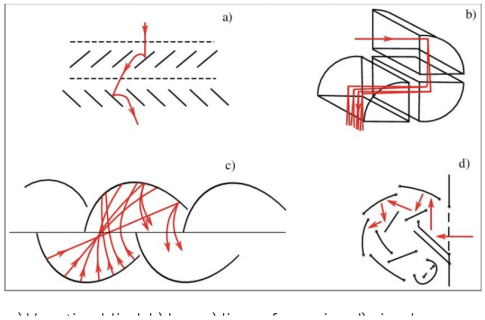

The geometry of dynodes in PMTs can vary, with configurations including venetian blind, box, linear focusing, and circular cage. A phenomenon known as dynode skipping, where electrons traverse without interacting with the dynodes, can affect signal uniformity, particularly in venetian blind structures.

PMT Window and Magnetic Shielding

Most PMT windows are made of borosilicate glass due to its ease of handling and cost-effectiveness. Enhancements can be made using UV-borosilicate or quartz glass to extend the wavelength threshold. Magnetic shielding is essential for PMTs, even against small magnetic fields, to maintain performance and reduce noise. This can be achieved using a mesh of μ-metal.

PMT Transit Time

The transit time in PMTs is defined as the interval between the creation of a photoelectron at the cathode and the detection of the signal at the anode. This time is subject to dispersion, typically described by a Gaussian distribution, which is crucial for understanding the timing performance of PMTs.

Photocathode

Photocathodes are often made from bi-alkali or multi-alkali compounds, such as SbCs, SbKCs, and SbNaKCs. These materials are chosen for their efficiency in absorbing photons and emitting electrons. The efficiency of a photocathode in converting photons to electrons is crucial for the performance of a photomultiplier tube (PMT). The provided image highlights the structure and function of the photocathode in this process.

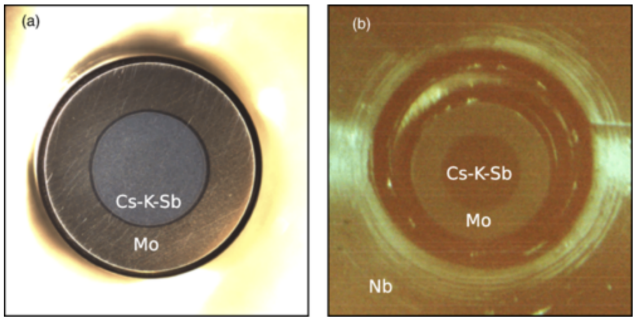

Glass and Gel Transmittance

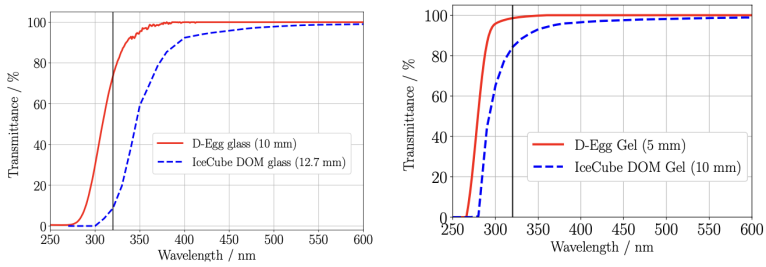

The light transmittance properties of the glass and silicone used in PMTs are critical for their performance. The D-Egg glass has a thickness of 10 mm and shows high transmittance at shorter wavelengths, especially important for detecting Cherenkov radiation.

The IceCube DOM glass, with a thickness of 12.7 mm, also performs well but not as effectively as the D-Egg glass. The graph indicates that the D-Egg glass and silicone (IceCube-Custom and IceCube-Custom-HE) have been optimized for high UV transmittance and low radioactive noise. These improvements significantly enhance the detection efficiency of PMTs at shorter wavelengths, which is vital for the IceCube project.

Photocathode Radiant Sensitivity

Quantum efficiency (QE) represents the signal yield per incoming photon, typically ranging from 25% to 40%. This efficiency is wavelength-dependent, with the maximum sensitivity usually between 300 nm and 600 nm.

The provided graph compares the radiant sensitivity (QS) of a PMT with and without a UV-transmissive entrance window, showing higher sensitivity for UV light when using specialized windows.

$$QS = \frac{N_{pe} \times e}{N_{ph} \times hv}$$

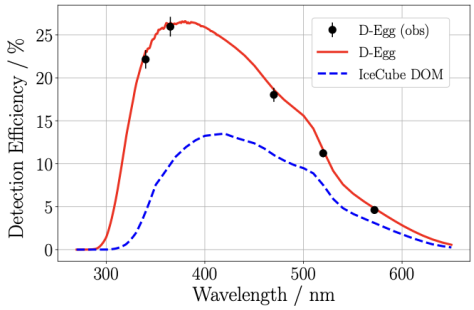

Image Source: Kolanoski, Wermes: Teilchendetektoren, Fig. 10.b

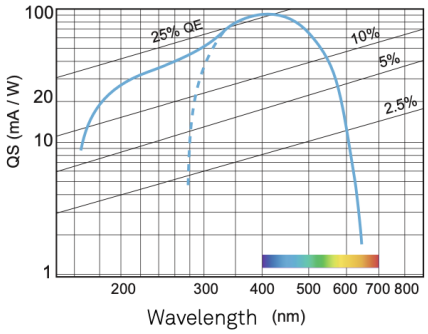

Sensitivity to Magnetic Fields

Photomultiplier tubes are sensitive to magnetic fields, which can distort their performance. Shielding with high-permeability materials like μ-metal is necessary to protect PMTs from external magnetic fields, even small ones like the Earth's magnetic field. Effective shielding involves wrapping the PMT in a conical shape around the neck to reduce sensitivity to magnetic fields and maintain signal integrity.

PMT Transit Time

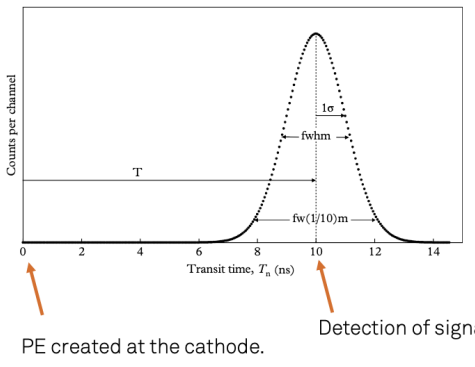

The transit time T is defined as the time between the creation of a photoelectron at the cathode and the detection of the signal at anode.

There is a certain amount of dispersion, generally described by Gaussian.

PE created at the cathode.

Detection of signal at the anode.

Early and Late Pulses

a) Clean event showing a single anode pulse. All but a few percent of measured events are of this type.

b) Event caused by elastic backscatter of of pe from d1 (or the support structure). The photoelectron decelerates in the electric field, stops right in front of the cathode and returns to d1.

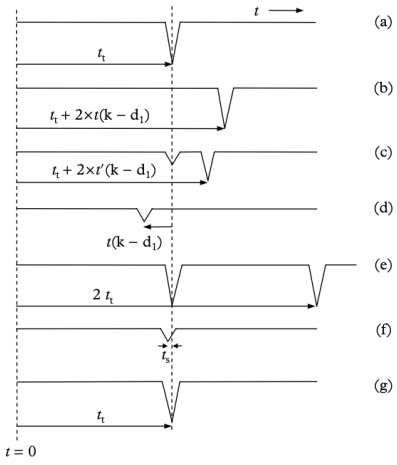

36

Early and Late Pulses

c) A photoelectron is scattered away from d1, carrying away a fraction of the total energy and two pulses of smaller size emerge.

d) A prepulse is generated by a photon hitting the first dynode (by passing the window and not hitting the cathode). Prepulses are smaller and are not registered in case the trigger threshold is set sufficiently high.

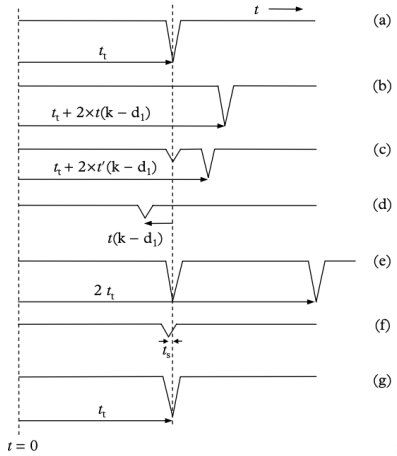

37

Early and Late Pulses

e) Second pulse is generated with twice the transit time. In case the signal is sufficiently high, the anode and the last few dynodes glow. There is a finite probability that one the emitted photons finds its way to the cathode and initiates a second cascade.

f) Early pulse due to scattering of electrons from d1 directly to d2. The resulting signal is undersized.

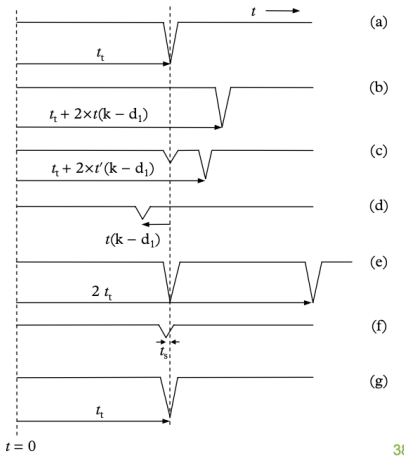

38

Early and Late Pulses

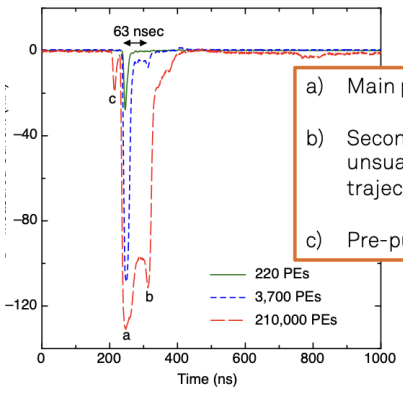

a) Main peak

b) Secondary peak due to unsual electron trajectories

c) Pre-pulse

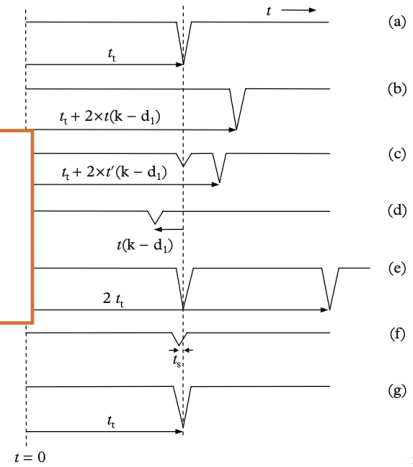

39

-> Afterpulses

- Originate from ions of gaseous impurities and molecules located in the region between the cathode and the first dynode
- Some afterpulses originate from inter-dynode ionization
- Typically between a few hundred ns and a few µs

IceCube Afterpulses

- Primary peak (a) is well visible and saturated
- Afterpulses around 600 ns, 2 µs and 8 µs
- Likely originate from ions of different masses
- Peak intensity grows linearly with flash intensity
- Afterpulses mainly originate from ions in early dynode stages (electron current rises, even when later stages have saturated)

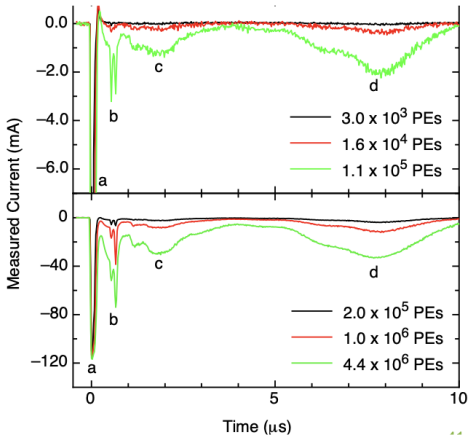

PMT Saturation

Photomultiplier tubes (PMTs) are highly sensitive devices used for detecting low levels of light. However, like all electronic devices, PMTs have operational limits, beyond which their performance can be compromised. This phenomenon is known as PMT saturation. Understanding PMT saturation is crucial for ensuring accurate measurements and extending the lifespan of the tube.

Saturation occurs when a PMT is exposed to an intensity of light that exceeds its ability to linearly convert photons into an electrical signal. In this state, the PMT's output signal no longer increases proportionally with the input light intensity, leading to a plateau or even a decrease in the detected signal.

Causes of PMT Saturation

1. **High Light Intensity:**
   - When the light intensity is too high, the number of photoelectrons generated at the photocathode increases dramatically. The subsequent electron multiplication process within the dynodes can become overwhelmed, leading to saturation.
2. **Excessive Gain Settings.**
3. **Continuous High Light Levels.**

LT12

Detector systems in High Energy Physics

What you should have seen so far

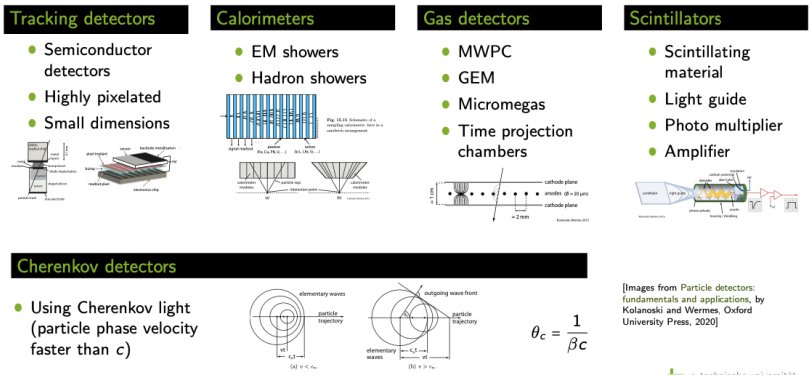

Historical Introduction Evolution of High Energy Physics

Historical Introduction

Initially, Max Planck was advised against studying physics, being told that it was a nearly complete science with little left to discover. Contrary to this, groundbreaking discoveries unfolded.

Roentgen Rays (X-Rays)

Wilhelm Roentgen, in 1895 at the University of Würzburg, discovered X-rays while experimenting with cathode rays. He noticed a fluorescent effect on a phosphor-coated screen, leading to the first X-ray image. Subsequently, in 1897, J.J. Thompson observed electrons, smaller particles than the atom, passing through Crookes tubes, marking the discovery of the electron.

Atomic Structure - Rutherford, Geiger, and Marsden (1909)

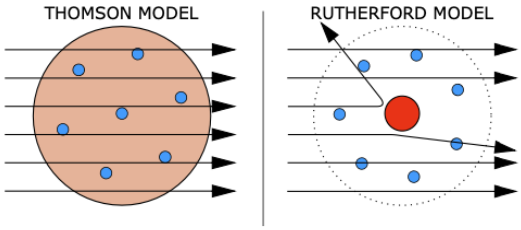

The Geiger-Marsden experiment involved directing alpha particles at a thin gold foil. Some alpha particles bounced back, leading to the realization that atoms have a small, dense nucleus, thus disproving the Thomson model and establishing Rutherford's nuclear model.

Cosmic Rays

Early 20th-century experiments revealed the extraterrestrial origin of cosmic rays. Theodor Wulf in 1909 used an electrometer at the Eiffel Tower to measure radiation, finding inconclusive results. However, Domenico Pacini in 1911 observed a decrease in radiation underwater compared to the surface. Victor Hess's 1912 balloon experiments conclusively showed increased radiation at higher altitudes, attributing it to cosmic rays.

Positron: Cloud Chamber Development

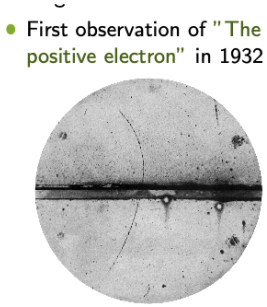

Charles Wilson developed the cloud chamber to visualize particle tracks using supersaturated water vapor. Carl Anderson improved this by using an alcohol solution and a magnet, leading to the discovery of the positron in 1932. The cloud chamber allowed Anderson to observe particles bending in a magnetic field, confirming the existence of the positron. Blackett and Occhialini, guided by Dirac's prediction, further utilized the cloud chamber with Geiger counters to detect positrons and muons.

First Accelerators

The first particle accelerators were developed in the 1930s. John Cockcroft and Ernest Walton, under Rutherford's direction, built an accelerator that split the atom in 1932 using 300,000 eV, as predicted by Gamow's quantum mechanics. Ernest Lawrence at the University of Berkeley developed the cyclotron, accelerating particles using cyclotron resonance.

- First prototype was 11 cm
- Prototype 4.7 m diameter reached 350 MeV

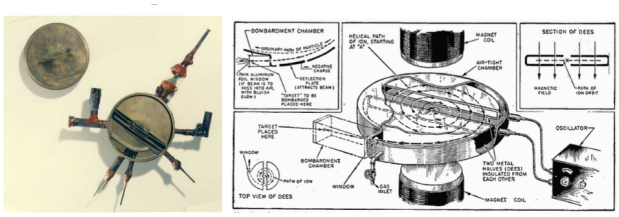

Finding Neutrinos (1956): Cowan-Reines Neutrino Experiment

The Cowan-Reines experiment in 1956 used scintillators and photomultiplier tubes to detect neutrinos through inverse beta decay, using a nuclear reactor as a neutrino source. Their experiments at the Savannah River Plant showed a significant increase in detected events with the reactor on, confirming the existence of neutrinos.

Hydrogen Bubble Chamber

The hydrogen bubble chamber, exemplified by the Gargamelle chamber at CERN in 1970, was a significant advancement in neutrino detection. It used superheated liquid hydrogen to visualize ionization trails, facilitating the study of subatomic interactions.

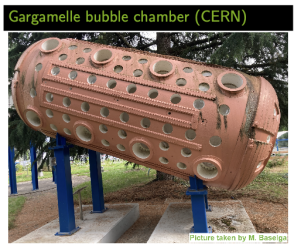

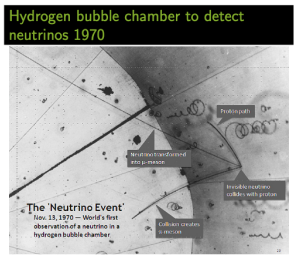

Standard Model Developments

From 1968 onwards, crucial discoveries completed the Standard Model:

- Up, down, and strange quarks were discovered at SLAC in 1968.
- The charm quark was discovered at SLAC and BNL in 1974.
- The tau lepton was discovered at SLAC between 1974-1978.
- The bottom quark was discovered at Fermilab in 1977.
- The W and Z bosons were discovered at CERN in 1983.
- The top quark was discovered at Fermilab in 1995.
- A boson consistent with the Higgs was discovered at CERN in 2012.

Detector Systems

HEP experiments rely on sophisticated detector systems to identify and measure particles. These systems typically include:

1. **Tracking Systems**: Provide detailed momentum and charge information.
2. **Calorimeters**: Measure the energy deposited by particles.

3. **Muon Systems**: Detect muons, which penetrate deeper than other particles.

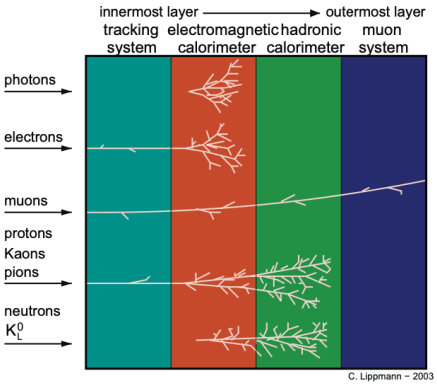

LHC (Large Hadron Collider)

The LHC accelerates particles in a 27 km tunnel, achieving collisions at four interaction points: ATLAS, CMS, ALICE, and LHCb. It uses various systems to detect and measure collision events, including tracking detectors, calorimeters, and muon spectrometers.

ATLAS Detector System

The ATLAS detector at the LHC includes:

1. **Inner Detector**: Features pixel detectors, a semiconductor tracker, and a transition radiation tracker for high-precision tracking.
2. **Calorimeters**: Electromagnetic and hadronic calorimeters to measure energy deposition.
3. **Magnet System**: Solenoid and toroid magnets for momentum measurements.
4. **Muon Spectrometer**: Various detectors to identify muons.

- Details of the ATLAS detector system

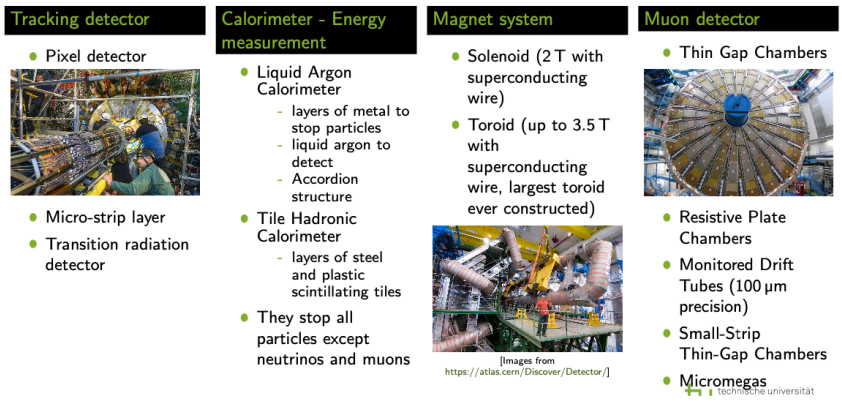

CMS (Compact Muon Solenoid)

The CMS detector includes a 4 Tesla solenoid, tracking system, calorimeters, and multiple muon detection systems such as drift tubes and GEMs. Its physics goals align with those of ATLAS.

LHCb and ALICE

LHCb specializes in b-physics, focusing on CP violation in b-hadron interactions. ALICE studies heavy ion collisions, aiming to understand strongly interacting matter at high energy densities.

Trigger Systems

HEP experiments utilize complex trigger and data acquisition systems to manage the vast amounts of data generated. These systems filter and store relevant data, enabling detailed analysis of particle interactions.

IceCube Neutrino Observatory (Antartica)

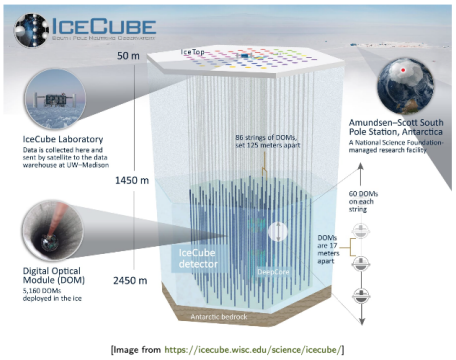

[Image from https://icecube.wisc.edu/science/icecube/]

Detector

- Spherical optical sensors (Digital Optical Modules DOMs)
- Connected to photomultiplier PMT

Physics

- Space neutrinos reach ice and might create charged leptons
- Leptons can emit Cherenkov radiation
- 10^6 muons come from cosmic rays, but can be rejected since they travel downwards
- Search for neutrinos in TeV range
- Neutrino physics, dark matter and glaciology

(Enriched Xenon Observatory) experiment: Neutrinoless double beta decay ($0\nu\beta\beta$)

($0\nu\beta\beta$)

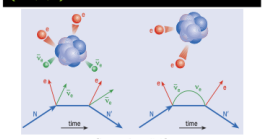

[Image from link]

- Double beta decay occurs when nucleus is energetically or spin forbidden to decay through single beta decay
- $0\nu\beta\beta$ would show that neutrino is a Majorana particle (or its antiparticle)
- could give information about neutrino mass

EXO-200

- EXO-200 is in a mine in New Mexico and cooled with cryostat (650 m under rock for clean background and layers of lead)
- Liquid Xenon (LXe) filling time projection chamber (TPC)

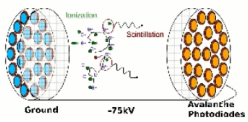

[Image from https://www-project.slac.stanford.edu/exo/about.html]

- Uses 200 kg of LXe enriched 80 % of the 136 isotope
- When particle deposits energy, it ionizes LXe atoms, e^- go to the wire
- Some Xe atoms recombine with e^-, and excite Xe
- When excited state relax, emits UV light, collected with Avalanche Photo Diode
- The neutrinoless decays would appear as narrow spike in the energy spectrum around the xenon Q-value ($Q_{\beta\beta} = 2457.8\,\text{keV}$)

AMS-02: Alpha Magnetic Spectrometer

- Search for dark matter, antimatter, strangelets and space radiation environment in the ISS

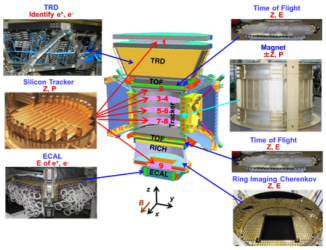

- Detector system:
  - Transition radiation detector measures the velocities of the highest energy particles
  - Time of flight counter, trigger for charge particles, determine the direction and velocity of particles
  - Star tracker determines the orientation of the module in space
  - Silicon tracker (9 disks among 6 locations) measures charge and momentum of particles
  - Permanent magnet bends the path of charged particles so they can be identified
  - Anti-coincidence counter rejects stray particles that enter through the sides
  - Ring imaging Cherenkov detector measures velocity of fast particles with extreme accuracy
  - Electromagnetic calorimeter measures the total energy of the particles

Muon g-2 at Fermilab

- Most precise measurement of anomalous magnetic moment of the muon
- proton beam collides $\rightarrow \pi \rightarrow \mu$
- μ with aligned spin stored in the storage ring
- Storage ring with extremely precise magnetic field
- As muon beam goes around the ring, the muons precess (wobble)
- Muon decays as ν and positron (only positron detected)

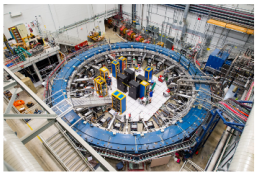

[https://muon-g-2.fnal.gov/index.html]

Detector system

- Magnetic moment measurement realized by 24 electromagnetic calorimeters
  - Calorimeter measure energy and time of arrival of the decay positrons
- Magnetic field curls the positron inwards and hits lead II fluoride calorimeter, read out by silicon photo-multipliers
- Tracking detectors also register the trajectory of the positron but do not provide the magnetic moment (dedicated to the beam profile of μ)

LT13

Detector systems in Medical Physics

The lecture will focus on the use of various detector systems in medical physics, particularly those used in X-ray diagnostics, PET (Positron Emission Tomography), and radiotherapy.

Detector Technologies:
Detector systems in medical physics primarily utilize

- scintillating materials with photo detectors,
- solid state detectors (such as silicon, diamond, and germanium)
- gas-filled detectors.

These technologies are important in both particle physics and medical physics applications.

X-ray

X-Ray Diagnostics

X-rays were discovered by Wilhelm Conrad Röntgen in 1895. The basic principle involves generating an X-ray beam, which undergoes absorption and scattering within the object.

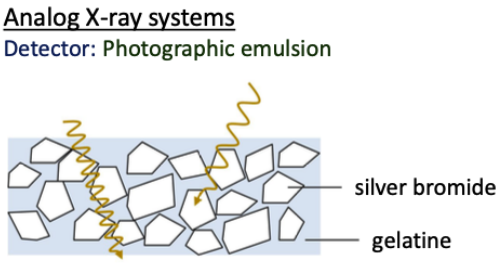

The intensity of the beam is then measured using a detector. Traditional analog X-ray systems used photographic emulsions, such as silver bromide, which provided high spatial resolution.

Photoemulsion

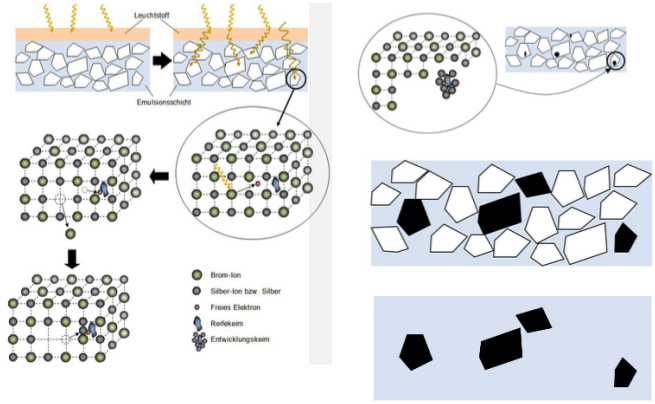

This image illustrates the process of photographic emulsion in X-ray detection, focusing on the behavior of silver (Ag) ions and the formation of Ag crystals.

Initially, when X-rays penetrate the emulsion layer, they cause ionization at certain sites. Bromide ions and silver ions are present in the emulsion. The Ag ions agglomerate at the initial ionization site. During the development process, these ions are reduced to form silver crystals. These crystals are visible as black spots in the developed photographic film.

The size of these silver crystals is a few micrometers (µm), providing very good spatial resolution of about 20 line pairs per millimeter (lp/mm). This high spatial resolution is critical for producing detailed images in analog X-ray systems.

The graphical representation shows the stages of this process, from ionization to the formation of Ag crystals, highlighting the structure and transformation within the emulsion layer.

Digital X-ray Imaging:
Modern X-ray imaging can be direct or indirect.

- In indirect detection, X-ray photons generate visible light in a scintillator, which is then converted into an electrical signal.
- Direct detection converts X-ray photons directly into an electrical signal using high-Z semiconductors like Ge, GaAs, CdTe, and CZT.

Energy-Integrating Readout:
This method integrates the output signal over a long period, with the grey value being proportional to the deposited energy.

Long integration time of the amplifier → output signal $\propto \int_0^{\Delta t} Q(t)\mathrm{d}t \propto \int_0^{\Delta t} I(t)\mathrm{d}t$

Disadvantage: Although it provides information on the energy and total number of photons, it also integrates electronic noise, which can reduce contrast and introduce artifacts like blooming and beam hardening.

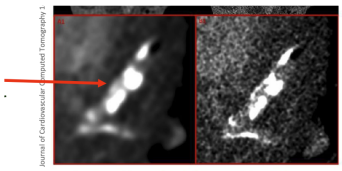

Photon Counting:
Photon counting detectors use multiple energy thresholds and associated counters per pixel to count hits above the respective thresholds.

Advantages

- improved contrast-to-noise ratio (CNR)
- low energy photons generate better contrast images
- offline reweighting possible
- improved spatial resolution due to directed e/h drift inside sensor
- enables multi-spectral imaging (e.g. DECT) with reduced dose
- identification of different contrast agents, tissue identification

Challenges

include handling high photon flux, cross-talk, and radiation hardness.

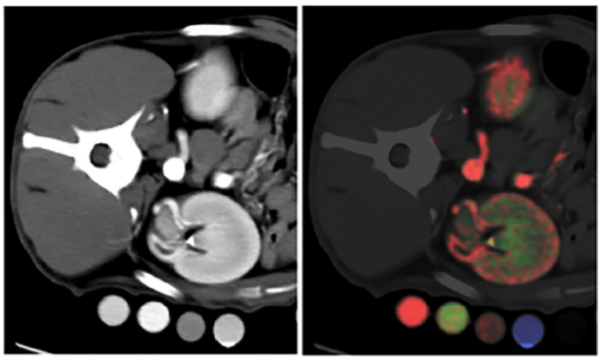

Image of a dog phantom using three different contrast agents (iodine, gadolinium, bismuth)

Examples:
Applications include the reduction of metal artifacts and the detection of kidney stones.

PET

In PET, a β+ source accumulates in the tissue of interest, often using FDG for cancer diagnostics, neurology, and cardiology. Scintillator detectors operating in coincidence mode create a point cloud of intersections of lines-of-response, indicating the location of the contrast agent.

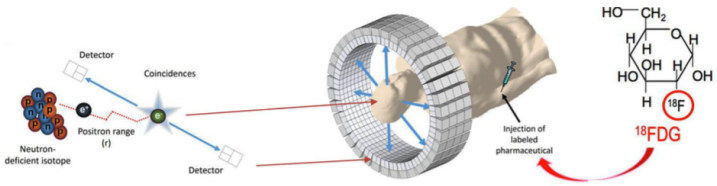

Description of the porcess of Positron Emission Tomography (PET) imaging:

1. **Injection of Labeled Pharmaceutical**: The process begins with the injection of ^18F-FDG into the patient. ^18F-FDG is a glucose analog where a fluorine-18 isotope replaces a hydroxyl group. Fluorine-18 is a positron-emitting radioactive isotope.
2. **Accumulation in Tissue**: After injection, the ^18F-FDG accumulates in tissues, particularly those with high metabolic rates, such as cancer cells, due to their increased glucose uptake.
3. **Positron Emission**: The ^18F undergoes beta-plus decay, emitting a positron (β+). The positron travels a short distance in the tissue before encountering an electron.
4. **Annihilation Event**: When the positron encounters an electron, they annihilate each other, resulting in the emission of two gamma photons. These photons are emitted in nearly opposite directions (approximately 180 degrees apart).
5. **Detection of Coincidences**: The PET scanner detects these pairs of gamma photons using a ring of detectors surrounding the patient. The simultaneous detection (coincidence detection) of these photons by detectors positioned across from each other identifies the location of the annihilation event along a straight line.
6. **Image Reconstruction**: By collecting numerous coincidence events, the PET scanner constructs a detailed image showing the distribution of the radioactive tracer within the body. This image reflects areas of high metabolic activity, which can indicate the presence of tumors or other abnormalities.

PET Detectors:

These detectors use segmented scintillators to achieve high spatial and time resolution. Bismuth germanate (BGO) is commonly used due to its high density and fast signal response in coincidence mode.

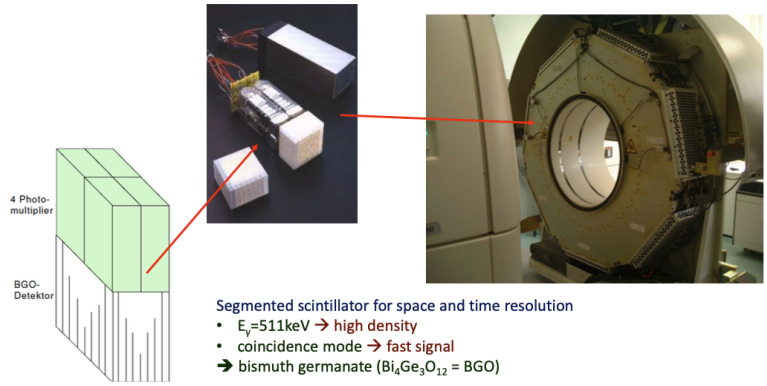

Coincidence Trigger:
For accurate coincidence detection, photons from the same annihilation event must reach detectors simultaneously. The signals must be active concurrently for a logic AND condition to be met, ensuring hits are read out efficiently. High temporal resolution and fast detectors are essential to avoid missed decays and ensure good timing resolution.

- Hit time has to be very well known (high temporal resolution)
- Need fast detectors (scintillators), so no decays go undetected
  - good timing resolution increases efficiency and reduces dose per image!

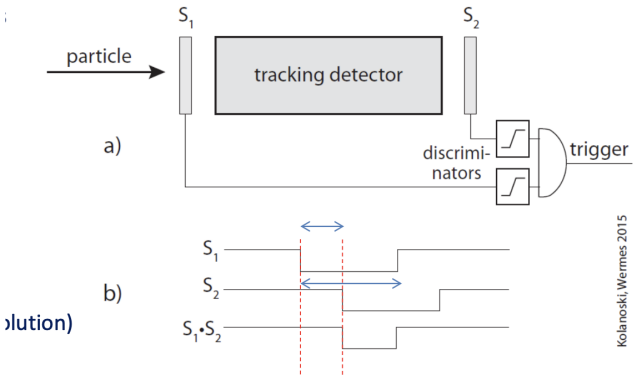

TOF-PET:
Time-of-flight PET (TOF-PET) *measures the delay between hits within the coincidence window*, estimating the decay position along the line-of-response:

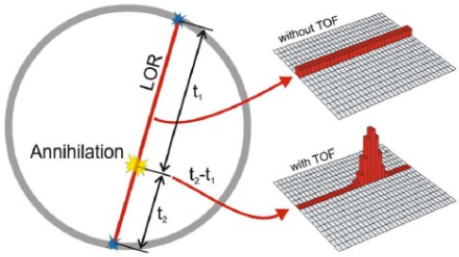

The required timing resolution is around 10 ps, which is still a subject of active research. Readout technologies like PMTs, SiPMs, and SPADs are explored for their potential in enhancing performance, especially in magnetic fields, enabling PET-MRT.

Detector systems in radiotherapy

Ionization Chambers:
Ionization chambers operate in unity gain mode, providing signals proportional to the energy dose.

Various types, such as parallel plate ionization chambers, multi-layer ionization chambers (MLIC), and strip chambers, serve different purposes like MU counting, particle energy/range measurement, 2D dose distribution, and beam position monitoring.

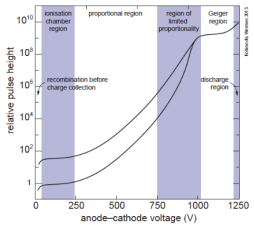

amentals of Detector Physics - Dr. Jens Weingarten 18

Examples of detector R&D in radiotherapy

Examples of detector research in radiotherapy include prompt gamma imaging and proton radiography.

Nuclear interactions during treatment generate excited nuclei

- Emission of gamma rays correlated with energy/dose deposition

Prompt gamma imaging uses nuclear interactions during treatment to emit gamma rays, which are detected to reproduce a 1D image of dose distribution.

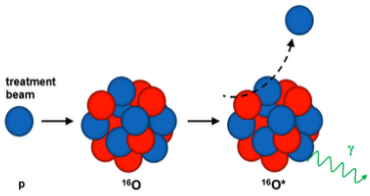

Proton radiography measures the energy of protons downstream of the patient to generate a 2D WET map, useful for adaptive radiotherapy by showing anatomical changes that might necessitate plan re-optimization.

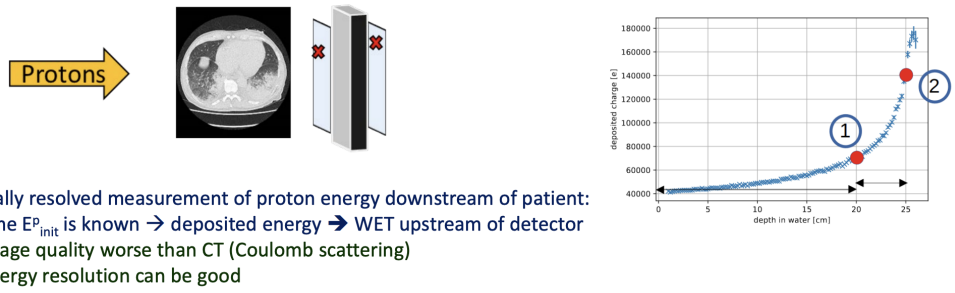

Spatially resolved measurement of proton energy downstream of patient:
assume E^{p}_{init} is known → deposited energy ➔ WET upstream of detector

- image quality worse than CT (Coulomb scattering)
- energy resolution can be good